Journal of Materials Chemistry A

REVIEW

View Article Online
View Journal | View Issue

Cite this: J. Mater. Chem. A, 2022, 10, 19129

Controlled local orientation of 2D nanomaterials in 3D devices: methods and prospects for multifunctional designs and enhanced performance

Hongying He, [a] Lizhi Guan[a] and Hortense Le Ferrand *[ab]

Two-dimensional (2D) nanomaterials are sheet-like crystalline solids exhibiting remarkable electrical, chemical, mechanical and optical properties. The emergence of 2D nanomaterials of diverse chemistries with unique performance at the nanometric scale provides great potential to establish enhanced functionalities at the macroscopic scale. However, transposing these nanoscopic properties into functional macroscopic devices remains a challenge due to the lack of suitable processing technologies. Recent experimental efforts to control the local orientation of 2D materials in thin films and reinforced composites have demonstrated significant advances in improving the bulk material performances and could be the key to unlocking next-generation multifunctional designs. Examples of these for sensors, thermoelectrics and energy harvesting devices are provided in this review. Then, we present the recent advances and methods for achieving controlled alignment of 2D nanomaterials, including in horizontal, vertical, heterogeneous and arbitrarily oriented configurations. Moreover, the advances in 3D printing technology to support aligned microstructures and its capability to build multimaterial compositions, design complex structures and scale up are discussed in detail. Finally, we envision exciting future developments yet also challenges to realize the promise of complex multifunctional energy devices based on 2D nanomaterials with enhanced performance and sustainability, potentially opening up new applications.

Received 10th March 2022
Accepted 25th April 2022

DOI: 10.1039/d2ta01926d

rsc.li/materials-a

1. Introduction

Multifunctional devices are objects able to achieve a combined set of properties, such as electrical, mechanical, optical, or thermal, and that are able to convert energy from one type to

[a]School of Mechanical and Aerospace Engineering, Nanyang Technological University, Singapore 639798. E-mail: hortense@ntu.edu.sg

[b]School of Materials Science and Engineering, Nanyang Technological University, Singapore 639798

Hongying He received her BS degree from Sichuan University, China, in 2016. Afterwards, she received her PhD degree in Mechanical Engineering from the National University of Singapore (NUS) in 2020. She is currently a research fellow in the School of Mechanical and Aerospace Engineering at Nanyang Technological University in Singapore. Her research interests focus on ceramic-based composite structural design for thermal management and study of lead-free ferroelectric ceramics and their functional applications.

Lizhi Guan received his PhD in Applied Chemistry from the Instituto de Ciencia de Materiales de Madrid (ICMM, CSIC) and Autonomous University of Madrid, Spain (2020). After that, he joined the School of Mechanical and Aerospace Engineering at Nanyang Technological University in Singapore as a research fellow. His research interests mainly include bioinspired carbon-based composites with multifunctional properties.

another. Electronic components, sensors, energy harvesting and water splitting devices, and catalyzers are examples of devices receiving great interest from both the scientific community and industries, and they require the fusion of multiple properties into one object. More recently, robotics, automobiles, artificial intelligence (AI), and the Internet of Things (IoT) have increasingly relied on multifunctional devices that are smaller, faster, high performing, and processable into 3D shapes by 3D printing. The rapid technological growth in these domains reflects the unprecedented advances in materials science and engineering and urges further material evolution on both functional and structural aspects. To fulfill these versatile functionalities and realize the promise of Industry 4.0, 2D nanomaterials which exhibit unique intrinsic properties have become an indispensable choice.

2D nanomaterials are a class of crystalline materials in the form of a single-layer or a few-layer lamellar structure. They possess a high lateral diameter to thickness aspect ratio as well as stronger in-plane interatomic interactions than in their stacking, out-of-plane direction. The year of 2004 witnessed the successful exfoliation of monolayer graphene by Geim and Novoselov,[1] which led to the renaissance of the study of 2D nanolayer materials. Since then, remarkable properties such as a large surface area, tunable surface functionality, strong mechanical strength, and excellent thermal and electrical conductivities have been successively found in graphene.[2–11] Notably, these outstanding properties in graphene such as its ultrahigh carrier mobility of 10^4 cm^2 V^{-1} s^{-1}, thermal conductivity of about 4000 W m^{-1} K^{-1} and high Young's modulus of about 1 TPa are demonstrated in the in-plane direction, which are significantly suppressed along the out-of-plane axis.[12–14] The preparation of 2D nanomaterials is commonly achieved by top-down approaches, where bulk layered materials are exfoliated into nanosheets for example using mechanochemical processes or by bottom-up synthesis from molecular precursors. More recently, the prosperous studies on graphene have expanded to the emergence of novel 2D nanomaterials of other chemistries.[15] For example, transition metal dichalcogenides (TMDCs), with the formula of MX_2, where M is a transition metal like Mo, Ti, V, Hf, W, *etc.*, and X represents a chalcogen such as S, Te and Se, have been found to exhibit tunable bandgaps for semiconducting and optoelectronic related applications.[6,16,17] In addition, 2D hexagonal boron nitride (h-BN), an isomorph of graphene, also attracts considerable attention. Indeed, different from the conjugated valence electrons in graphite, the distinct electronegativity of B and N atoms provides electrical insulation to h-BN.[18] Thanks to its outstanding electrical insulation, an in-plane thermal conductivity of about 400 W m^{-1} K^{-1}, thermal stability at temperatures higher than 600 °C, mechanical robustness and chemical inertness, 2D h-BN becomes very useful for microelectronics, as a reinforcing nanofiller and field effect transistor (FET), among others.[19,20] Moreover, the family of MXenes, which represents 2D transition metal carbides, nitrides and carbonitrides, has grown rapidly over the past decade.[21–23] MXenes have a general formula of $M_{n+1}X_nT_x$ ($n = 1$–3), where M is a transition metal such as Ti, Ta, V, Zr, *etc.*, X is carbon or nitrogen, and T_x represents surface functional groups. Since the report of Ti_3C_2 in 2011, there have been more than 30 different MXenes synthesized, which typically exhibit metallic conductive properties because of the existence of conductive carbon and metal layers in the 2D structure and a hydrophilic nature due to the surface terminations like hydroxyl, oxygen or fluorine.[21,24,25] The wide chemical and structural variety of MXenes enables their promising applications for energy storage, electromagnetic interference (EMI) shielding, catalysis, sensors and so on.

The diverse crystal structures and blooming functionalities in 2D nanomaterials provide great opportunities to establish optimized material performances for realistic device applications. Indeed, tailored microstructures with local orientation of 2D nanomaterials could be an efficient pathway to unlock their potential and transpose their outstanding nanoscopic properties to the macroscopic scale. Controlling the assembly of anisotropic particles into hierarchical structures is a way to induce new, unique macroscopic properties that cannot be obtained in random configurations. This effect is well demonstrated in natural materials, which have evolved complex microstructures with local alignment over the years, providing us with an inspirational gallery for structural design and fabrication.[26–30] By mimicking these natural microstructures, many advanced artificial materials exhibiting attractive properties and functions have been realized (Fig. 1). We can imagine that if these delicate local orientations can be precisely controlled and reasonably combined with various 2D nanomaterial combinations, any set of desired functionalities could be realized.

The capability of precisely controlling the alignment of 2D nanomaterials has always been exciting but rather challenging. Fig. 2a displays the statistical number of publications on 2D nanomaterials and 2D nanomaterials with an aligned structure from 2011 to 2021. In the past ten years, there has been a significant increase in 2D nanomaterial-related studies, reflecting the promise of 2D nanomaterials for materials

Hortense Le Ferrand is a Nanyang Assistant Professor in the School of Mechanical and Aerospace Engineering and School of Materials Science and Engineering at Nanyang Technological University in Singapore, where she leads the Laboratory for Dense Multifunctional Composites (LDMC). She received her PhD degree in Materials Science from the Swiss Federal Institute of Technology (ETH Zürich) in Switzerland in 2017. Dr Le Ferrand is the recipient of the prestigious National Research Foundation Fellowship (2020) from Singapore. Her research focuses on novel additive manufacturing technologies for dense composites, microstructural designs and fabrication of bio-inspired composite and ceramic materials for combined structural and functional properties.

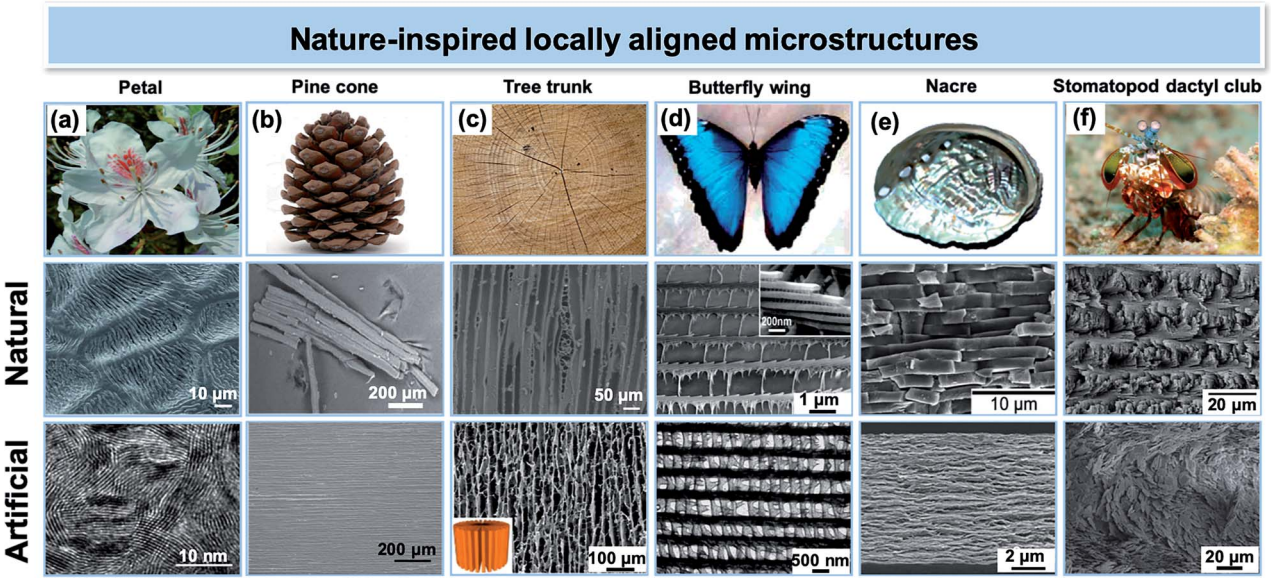

Fig. 1 Representative locally aligned microstructures found in natural species and their mimetic artificial counterparts: (a) locally ordered surface patterning of *Yunnan rhododendron* petals and MoS_2 nanofilms with molecular layers perpendicular to the substrate. Reproduced from ref. 31 with permission from The Royal Society Publishing. Reproduced from ref. 32 with permission from the National Academy of Sciences. (b) Bi-layer active hygroscopic tissue of a *Pinus coulteri* pine cone and aligned carbon nanotubes (CNTs) in paraffin wax. Reproduced from ref. 33 with permission from The Royal Society Publishing. Reprinted with permission from ref. 34. Copyright (2015) American Chemical Society. (c) Radial alignment in a tree trunk and freeze-casted graphene oxide (GO) aerogel with a radial and centrosymmetric structure. Reproduced from ref. 35 with permission from NC State University. Reprinted with permission from ref. 36. Copyright (2018) American Chemical Society. (d) Lamellae microstructure of the scales of a *Morpho peleides* butterfly wing and replica made of alumina. Reprinted with permission from ref. 37. Copyright (2006) American Chemical Society. (e) Brick-and-mortar layered microstructure of the nacre layer in seashells and artificial nacre made of layered poly(vinyl alcohol)–clay–nanofibrillar cellulose. Reproduced from ref. 38 with permission from Elsevier. Reproduced from ref. 39 with permission from John Wiley and Sons. Reprinted with permission from ref. 40. Copyright (2014) American Chemical Society. (f) Helicoidal orientation in the stomatopod dactyl club and similar orientation pattern with alumina microplatelets. Reproduced from ref. 41 with permission from Elsevier. Reproduced from ref. 42 with permission from Springer Nature.

development. The publications related to aligned 2D nanomaterials also exhibit a growing tendency especially in the latest years. However, these studies only comprise 7.67% of the total research on 2D nanomaterials (Fig. 2b), indicating an available, vacant area for further research. Classifying the alignment of 2D nanomaterials as vertical, horizontal, arbitrary and heterogeneous microstructures, it appears that vertical and horizontal alignment account for the most research interest (Fig. 2c).

From these recent studies, one major observation is that the lateral size of 2D nanomaterials and their orientations greatly impact the properties at the microscopic and macroscopic scales. These results have already been reviewed and summarized by others. For example, Luo *et al.* compared the strategies of improving photocatalytic performances by assembling functional architectures with 2D nanomaterials and analyzed its role in enhancing the energy conversion efficiency.[43] Zhang *et al.* reviewed the growth mechanism of vertically aligned graphene nanosheet arrays (VAGNAs) and discussed their properties for electrochemical energy applications.[44] Yaraghi *et al.* focused on fabrication methods and structures of biomimetic structural materials with brick-and-mortar and helicoidal architectures.[45] Cao *et al.* provided a survey on low-dimensional materials for electromagnetic (EM) applications and discussed the strategy of constructing well-aligned 2D nanosheets.[46] Tan *et al.* stressed the advances of vertically aligned nanosheets (VANSs) for batteries.[47] Furthermore, Huang *et al.* pointed out that aligned carbon-based electrodes (ACBEs) can greatly enhance the battery power density due to the combined advantages of an aligned structure and carbon-based materials.[48] Shao *et al.* emphasized the role of the freeze casting technique in the formation of well-controlled biomimetic porous materials from low-dimensional building blocks.[49] Moreover, Lei *et al.* reviewed the specific role of vertically aligned structures in polymer composite materials for multiple applications.[50] Zhang *et al.* provided synthesis and modification methods of polymer composites with aligned 2D nanomaterials and their potential applications.[51] In most of the reviews, the controlled orientation mainly focused on a single orientation type such as vertical or horizontal, throughout the bulk material, or limited fabrication methods for a specific target application. A systematic review on diverse orientation design of 2D nanomaterials and their augmented properties is thus still lacking.

In view of controlling the microstructural local alignment of 2D nanomaterials for improving performances, it is therefore timely to review the up-to-date development on this topic and to propose a vision on how to leverage the diversity in the chemistry and properties of 2D nanomaterials to yield multifunctional high-performance devices. Herein, we review the most recent research on controlled local orientation of 2D nanomaterials for functional designs and envision future prospects.

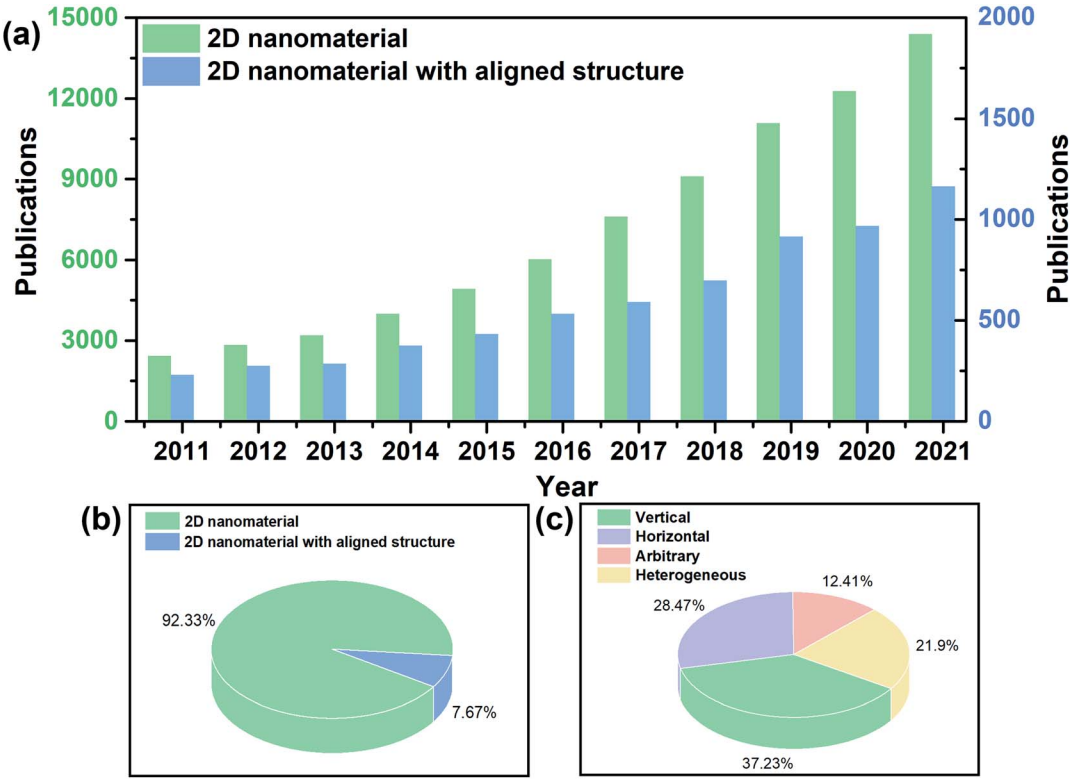

Fig. 2 (a and b) Publications on 2D nanomaterials and 2D nanomaterials with an aligned structure from 2011 to 2021. The publication numbers were collected from the *Web of Science* using the key words "2D nanomaterial" and "2D nanomaterial aligned structure" or "2D nanomaterial oriented structure" or "2D nanomaterial ordered structure". (c) Publications on aligned 2D nanomaterials with different orientation types.

The outline of this review is presented in Fig. 3. First, in this introduction, the background for studying 2D nanomaterials and the inspiration to develop locally aligned microstructures are provided. In the next section, we provide examples that demonstrate how oriented 2D nanomaterials can enhance the performances for selected applications, namely sensing, thermoelectrics and electrochemical energy harvesting, followed by reviewing the fabrication methods for horizontal, vertical, heterogeneous, and arbitrarily aligned microstructures. To bridge the gap between microstructural and 3D macroscopic devices, the fourth section of this review discusses how 3D printing can contribute to achieving locally aligned structures and what is its capability to build macroscopic architectures combining multiple chemistries. Finally, we anticipate the potential of controlled alignment of 2D nanomaterials for functional designs and applications and discuss remaining challenges, for the fabrication of next-generation smart multifunctional devices.

2. Oriented 2D nanomaterials for functional applications

This section provides examples from the literature, which demonstrate why orienting 2D nanomaterials purposely is key for achieving high performance in macroscopic components. We specifically selected a few functional applications that we see as the most promising for future energy and sustainability enhancement and that are under intense research in the materials community. These are sensing, thermoelectrics and electrochemical energy harvesting applications. The reader is then invited to draw analogies for other applications of their interest, where aligned and specifically oriented 2D nanomaterials could enhance the properties and functionalities of materials and devices.

2.1 Sensing

A sensor is a signal generator that captures a physical input from its working environment and converts it into a readable output. An ideal sensor should possess high sensitivity, selectivity and stability.[15,61,62] The sensitivity is typically determined by the ability of materials to respond to environmental stimuli such as optical, thermal, electrical, mechanical or chemical variations.[63,64] 2D nanomaterials, with their exceptional surface properties, are promising candidates for sensing applications. Controlling the alignment of 2D nanomaterials has proved to be beneficial in sensing mainly because it can improve (i) the density of exposed active sites, (ii) the surface-to-volume ratio, and (iii) the charge transfer within the oriented material.[65] Gas sensing and photodetection are among the most extensively studied sensing applications using 2D nanomaterials. In gas sensing applications, the mechanism consists of transforming chemical potential into electrical current density through gas molecule adsorption, where the resistance change is closely related to chemical reactions occurring at the surface of the

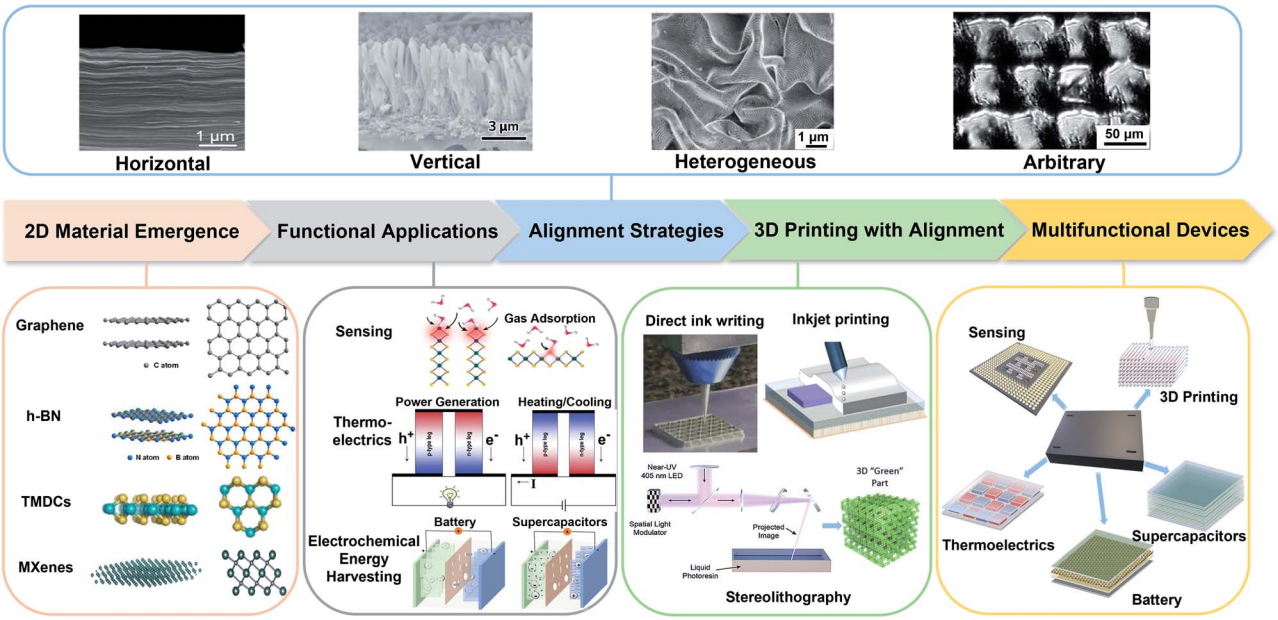

Fig. 3 Graphical outline of this review: from the background for emerging 2D nanomaterial study, established functional applications using oriented 2D nanomaterials, to fabrication methods of various orientations including 3D printing, following by the potential of developing multifunctional devices. Reprinted with permission from ref. 15. Copyright (2017) American Chemical Society. Reproduced from ref. 52 with permission from the Royal Society of Chemistry. Reproduced from ref. 53 with permission from Elsevier. Reproduced from ref. 54 with permission from John Wiley and Sons. Reprinted with permission from ref. 55. Copyright (2015) American Chemical Society. Reproduced from ref. 56 with permission from the Royal Society of Chemistry. Reproduced from ref. 57 with permission from Springer Nature. Reproduced from ref. 58 with permission from the Royal Society of Chemistry. Reproduced from ref. 59 with permission from John Wiley and Sons. Reproduced from ref. 60 with permission from Springer Nature. Reproduced from ref. 274 with permission from Springer Nature. Reproduced from ref. 323 with permission from the Royal Society of Chemistry.

nanomaterials. For photodetection, the mechanism is to convert an incident optical signal into an electrical signal based on the optical responsivity of the material.[66–70] Taking gas sensing as an example, the sensitivity (S) is defined as:

$$S\ (\%) = \frac{\Delta I}{I_0} \times 100, \quad (1)$$

where ΔI is the gas-induced current change and I_0 is the current of the sensor without gas.[71–73] Various 2D nanomaterials such as MXenes,[74,75] TMDCs,[76–78] graphene[79,80] and phosphorene[81,82] have been used to absorb gases like NO_2,[77,83] CO,[84] CO_2,[79,85] NH_3,[76,86] and H_2S.[87] Fig. 4 illustrates the NO_2 gas sensing properties of MoS_2 films with horizontal, vertical and mixed alignment structures.[55] During gas sensing, the gas adsorption capability is closely related to the binding energy between the active sites and the gas molecules. The exposed edge sites with high surface energy in vertically aligned MoS_2 provided high adsorption, while the adsorption in the basal plane of horizontal alignment was much lower (Fig. 4a). Meanwhile, the resistance of the vertically aligned film was significantly increased, which was attributed to the dominated carrier transport within the van der Waals gaps in the cross-plane direction (Fig. 4d). As a result, the vertically aligned MoS_2 film allowed a 5-times higher resistance variation (Fig. 4e) and could even detect 0.1 ppm of NO_2 gas when the maximum amplitude of electrical responses $(\Delta R/R_b)_{max}$ was 0.2%, which was impossible in the horizontally aligned film (Fig. 4f). In another example, Jiang *et al.* reported the H_2S gas sensing response of Fe_2O_3/graphene nanosheets with horizontal and vertical alignments (Fig. 4g and h).[87] The alignment was induced by controlled magnetic field assembly under a directed flow and will be described in Section 3 of this review. The vertically aligned Fe_2O_3/graphene nanosheets exhibited higher sensitivity (~450 absorption units to 15 ppm H_2S) than the horizontally aligned ones (~350 absorption units to 23 ppm H_2S) at a working temperature of 190 °C (Fig. 4j). This improved sensing capability in response to H_2S gas could be contributed by a larger contact area as well as less resistance to the target gas flow. Islam *et al.* also observed high sensitivity to NO_2 gas in vertically aligned MoS_2 layers.[72] The sensitivity was about 160–380% within a gas concentration range of 5–30 ppm, demonstrating a much higher response compared with the horizontally aligned layers. The higher sensitivity in the vertical alignment could be attributed to the exposed edge sites with sufficient dangling bonds, leading to high chemical reactivity and adsorption capability. These few, selected examples illustrate how the orientation of 2D nanomaterials can be utilized to boost the performance of sensing devices.

2.2 Thermoelectrics

To tackle the increasing global energy demand, the ability of harvesting electrical energy from waste heat from the thermoelectric effect has attracted considerable attention.[88–91] The

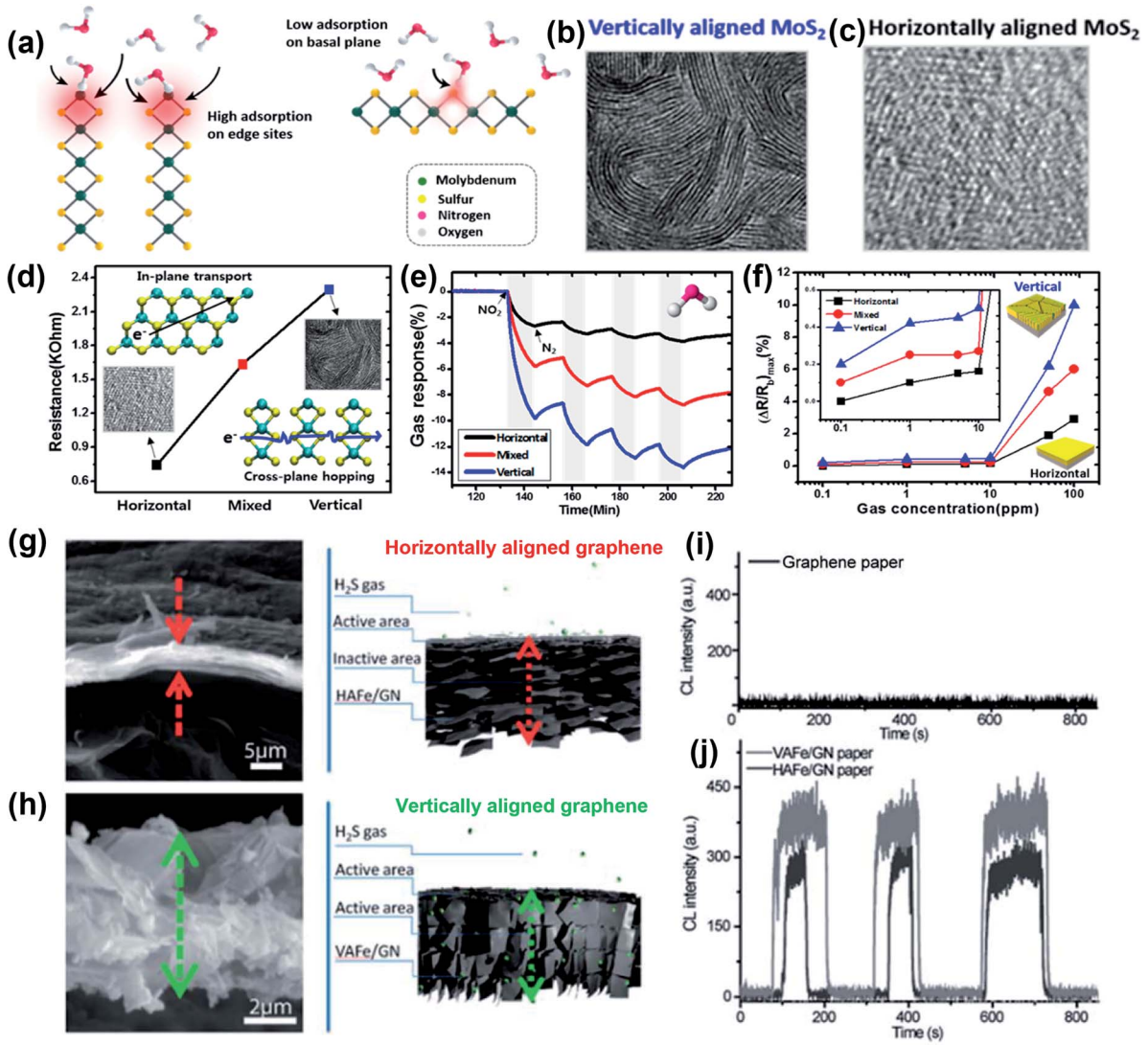

Fig. 4 Gas adsorption properties of MoS_2 films with horizontal, vertical and mixed alignments for gas sensing. (a) Schematic illustration showing the mechanism of gas adsorption on the edge sites and basal plane of MoS_2 films. SEM images of (b) vertically aligned and (c) horizontally aligned MoS_2 films. (d) Resistance in relation to different alignments with higher resistance in the vertically aligned MoS_2 film because of cross-plane hopping of carriers. (e) Resistance changes of 100 ppm NO_2 gas adsorption demonstrating the superior gas sensing properties of edge sites than the basal plane. (f) Maximum electrical responses of the synthesized MoS_2 films within 0.1–100 ppm of NO_2 exposure. Reprinted with permission from ref. 55. Copyright (2015) American Chemical Society. Morphologies of (g) horizontally aligned Fe_2O_3/graphene paper and (h) vertically aligned Fe_2O_3/graphene paper. Response curves of H_2S on the chemiluminescence (CL) intensity of (i) graphene paper fabricated by traditional filtration and (j) vertically arranged Fe_2O_3/graphene nanosheets (VAFe/GN) and horizontally arranged Fe_2O_3/graphene nanosheets (HAFe/GN) with a controlled orientation. Reproduced from ref. 87 with permission from the Royal Society of Chemistry.

thermoelectric effect refers to the phenomenon by which a temperature difference is directly converted into an electric voltage and *vice versa*. The process of voltage generation from a temperature difference is known as the Seebeck effect (Fig. 5a), while the conversion process of creating a temperature difference upon an applied voltage is the Peltier effect (Fig. 5b).[92] The working mechanism of the thermoelectric effect is related to the perturbation of charge carriers in equilibrium distribution. When there is a temperature gradient, the charge carriers migrate from high temperature to low temperature, leading to the generation of voltage. The performance of thermoelectric materials is characterized by the dimensionless thermoelectric figure of merit, ZT:

$$ZT = \frac{\sigma S^2 T}{k}, \quad (2)$$

where σ is the electrical conductivity, S is the Seebeck coefficient, T is the temperature, and k is the thermal conductivity.[93] Based on eqn (2), an ideal thermoelectric material should possess a high electrical conductivity, a high Seebeck coefficient and a low thermal conductivity. The optimum carrier concentration for a high thermoelectric performance and thermoelectric power factor (σS^2) is illustrated in Fig. 5c.

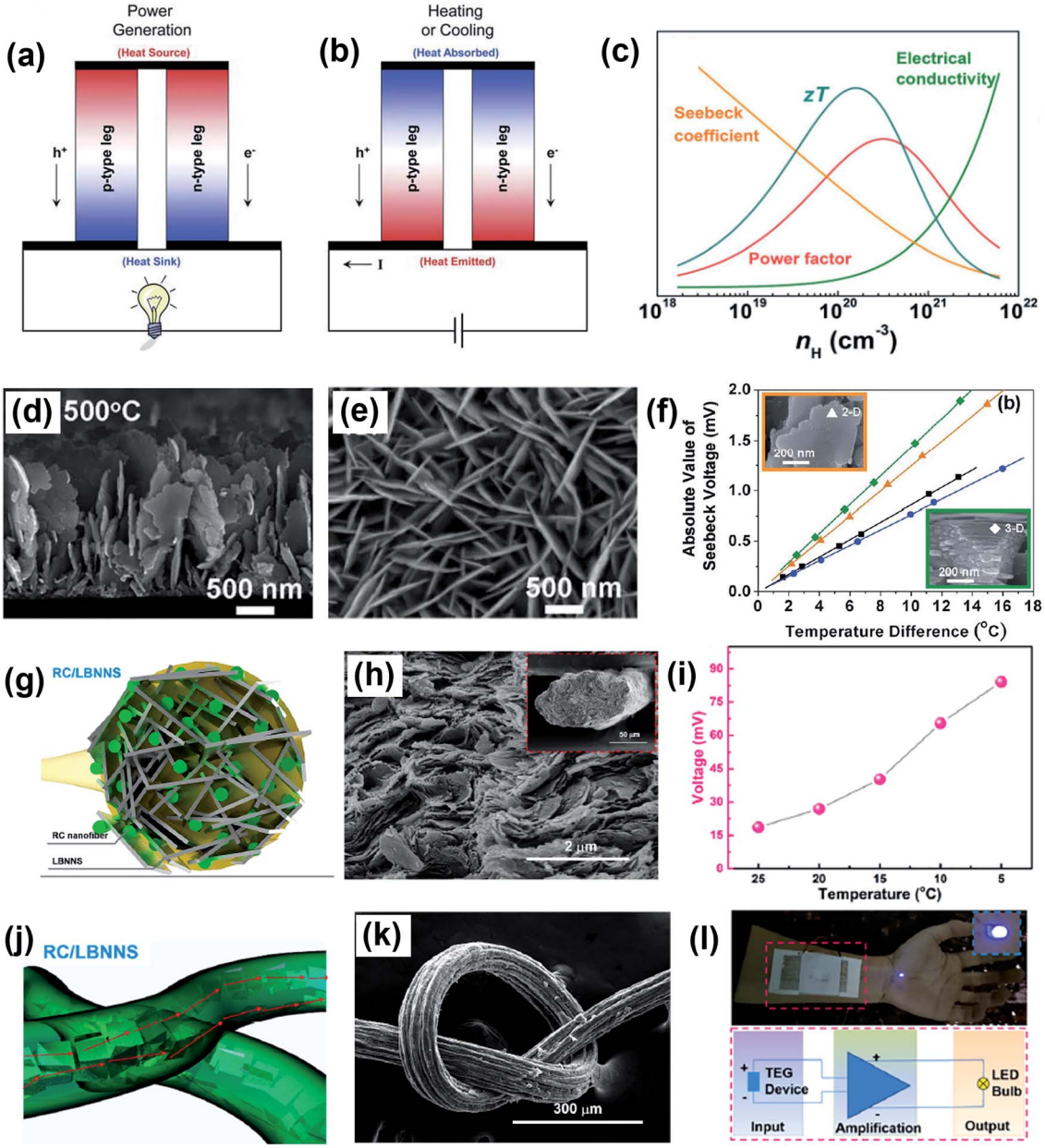

Fig. 5 Controlled alignment of 2D materials for thermoelectric applications. Schematic illustration of thermoelectric devices for (a) voltage generation and (b) heating or cooling applications. Reproduced from ref. 56 with permission from the Royal Society of Chemistry. (c) Optimum carrier concentration (n_H) for the thermoelectric figure of merit (ZT) and power factor. Reproduced from ref. 104 with permission from John Wiley and Sons. Well-aligned 2D Bi_2Te_3 nanoflakes as thermoelectric materials. SEM images of (d) cross sectional and (e) top view morphologies. (f) Seebeck voltage as a function of the temperature difference in aligned 2D and 3D Bi_2Te_3 nanoblocks. Reproduced from ref. 101 with permission from the Royal Society of Chemistry. Aligned regenerated cellulose (RC)/BNNS composite filaments for wearable thermoelectric devices. (g and j) Schematic representation of RC/BNNS composite filaments. (h and k) Morphology of RC/LBNNS composite filaments. (i) Generated voltage at different ambient temperatures. The red arrow refers to the heat conduction direction. (l) Diagram of a wearable thermoelectric device and its ability to light a LED bulb. Reproduced from ref. 103 with permission from Elsevier.

Besides the well-known thermoelectric materials like Bi_2Te_3, Sb_2Te_3, PbTe, *etc.*, emerging 2D nanomaterials with a high electrical conductivity or high Seebeck coefficient, such as graphene,[94–96] TMDCs,[97,98] and MXenes,[99,100] are also promising for thermoelectric applications. Interestingly, controlling the alignment of 2D nanomaterials is a great way to enhance the thermoelectric performances. The pivotal concepts of this enhancement are to (i) increase ion mobility in aligned carrier pathways for improved electrical conduction, and (ii) induce more phonon scattering to suppress thermal conduction or tune the thermal conductivity along the selected directions. For example, Chang *et al.* investigated the role of alignment in 2D Bi_2Te_3 nanosheets for thermoelectric applications.[101] 2D Bi_2Te_3 nanosheets with a vertical alignment to the SiO_2/Si substrate

were grown by pulsed laser deposition at 500 °C (Fig. 5d and e). The good alignment contributed to improved electrical conductivity and Seebeck voltage generation compared to randomly aligned nanosheets (Fig. 5f). Consequently, an in-plane thermoelectric power factor of 1.35 μW cm^{-1} K^{-2} was obtained in vertically aligned nanostructures, which was effectively improved compared to that under random conditions (<1 μW cm^{-1} K^{-2}). In another example, Oh *et al.* achieved significantly improved thermoelectric properties in an aligned MoS_2/graphene nanoribbon heterojunction.[102] A vertical heterojunction was designed to maximize the carrier transport: carriers can pass back and forth between the graphene and MoS_2 nanosheets easily to induce the thermoelectric effect. The as-synthesized nanostructure exhibited an enhanced electrical conductivity of 700 S m^{-1} and a high power factor of 222 μW m^{-1} K^{-2}. In addition, Wu *et al.* developed regenerated cellulose (RC)/BNNS composite filaments with an oriented microstructure using a wet-spinning procedure, which will be described later in the review.[103] With the alignment, the large-sized BNNSs were confined among adjacent RC nanofibers at a high filler loading, providing high anisotropy to the filaments (Fig. 5g, h and j, k). The aligned RC/BNNS composites displayed extraordinary thermal conduction and could be used in wearable thermoelectric generator (TEG) devices that can promptly transport body heat from skin to the surface of the composites. A maximum Seebeck voltage of 84 mV was achieved at an ambient temperature of 5 °C (Fig. 5i). Therefore, the aligned composites can be utilized as a wearable heat spreader to improve energy harvesting efficiency, which demonstrates potential in high-performance wearable electronics (Fig. 5l). These exciting examples demonstrate how the orientation of 2D nanomaterials can be leveraged to increase the functionalities of thermoelectric devices for robotics, energy harvesting, and electronics, among others.

2.3 Electrochemical energy harvesting

An ideal electrochemical energy storage (EES) device should have low cost, long life span, high energy and power density, good recycling stability, and safety. Two main types of EES devices are batteries and supercapacitors that are composed of two porous electrodes separated by a porous layer, the electrolyte. During charging and discharging, ions, such as lithium, travel back and forth between the cathode and the anode through the electrolyte (Fig. 6a). In supercapacitors, the energy storage is attributed to a double layer capacitance and a surface redox reaction creating pseudocapacitance, as described in Fig. 6b. Since the discovery of graphene, 2D nanomaterials have become predominant electrode materials in pursuit of high power and energy density for batteries and supercapacitors.[105–107] For example, MXenes have a conductive inner transition metal carbide layer that allows fast electron supply to active sites. Meanwhile, a transition metal oxide-like surface is redox active, and the 2D morphology and nano-confined fluid molecules enable fast ion transport.[108–110] The MXene electrode structure in supercapacitors is able to deliver up to 210 F g^{-1} at a scan rate of 10 V s^{-1} and a volumetric capacitance of ~1500 F cm^{-3}.[111] However, 2D nanomaterials used as electrodes tend to aggregate and restack into microparticles, which result in low electrolyte ionic conductivity and high electrode tortuosity and further limit ion transport between the electrode and the electrolyte. The ion transport in electrolytes includes ion migration and ion diffusion. It is related to the intrinsic conductivity of ions and the tortuosity of the porous electrode. The effective diffusivity in the electrolyte is commonly defined as:

$$D_{\text{eff}} = D \times \frac{\varepsilon}{\tau}, \tag{3}$$

where D is the diffusion coefficient, ε is the porosity, and τ is the tortuosity. An empirical correlation between ε and τ is provided by a Bruggeman-type relationship:

$$\tau = \gamma \varepsilon^{1-\alpha} \tag{4}$$

where α is the Bruggeman exponent correlated with the porosity, and γ is a scaling factor.[112] When the conductive pathways are composed of straight channels that are parallel to the transport direction, τ is 1.[113] A lower value of tortuosity leads to higher effective ionic diffusivity and ionic conductivity. Therefore, to facilitate ion transport in 2D nanomaterial-based electrodes, designing vertically aligned microstructures is a promising strategy to enhance power and energy density (Fig. 6c).[113] Numerous examples in the literature illustrate the benefits of this strategy in batteries and supercapacitors.[114,115] The most recent progress in this domain is reviewed in the following paragraph.

Vertically aligned structures composed of 2D nanomaterials including graphite, graphene, lithium metal phosphate, MXenes, and transition metal oxides have exhibited outstanding performances and promising commercialization prospects for batteries and supercapacitors. Indeed, vertical alignment of 2D nanosheets enables directional ion transport that can lead to thickness-independent electrochemical performances in thick films.[116–119] A recent study demonstrated successful alignment of graphite with superparamagnetic nanoparticles of Fe_3O_4 driven by a magnetic field, which allows cycling at a fast rate of up to 2C with a specific charge three times higher than that of the anode with a disordered structure.[120] The out-of-plane tortuosity of graphite aligned perpendicularly to the current collector is reduced by nearly four times. In addition to graphite, graphene has attracted much more attention because of its excellent electrical conductivity and ultrahigh surface area. Described by Hao *et al.*, three structures of graphene including vertically (VGA), horizontally (HGA), and randomly (RGA) aligned electrodes were fabricated, which showed a tortuosity of 1.25, 4.46, and 1.76, respectively.[121] High electrode tortuosity induced locally higher current density on the top surface of horizontal alignment and random graphene, which resulted in dendritic Li overgrowth on the surface (Fig. 6d and e). In contrast, lower electrode tortuosity in the vertically aligned graphene enabled homogeneous Li transport and uniform Li deposition across vertically aligned graphene (Fig. 6f).[121] Upon

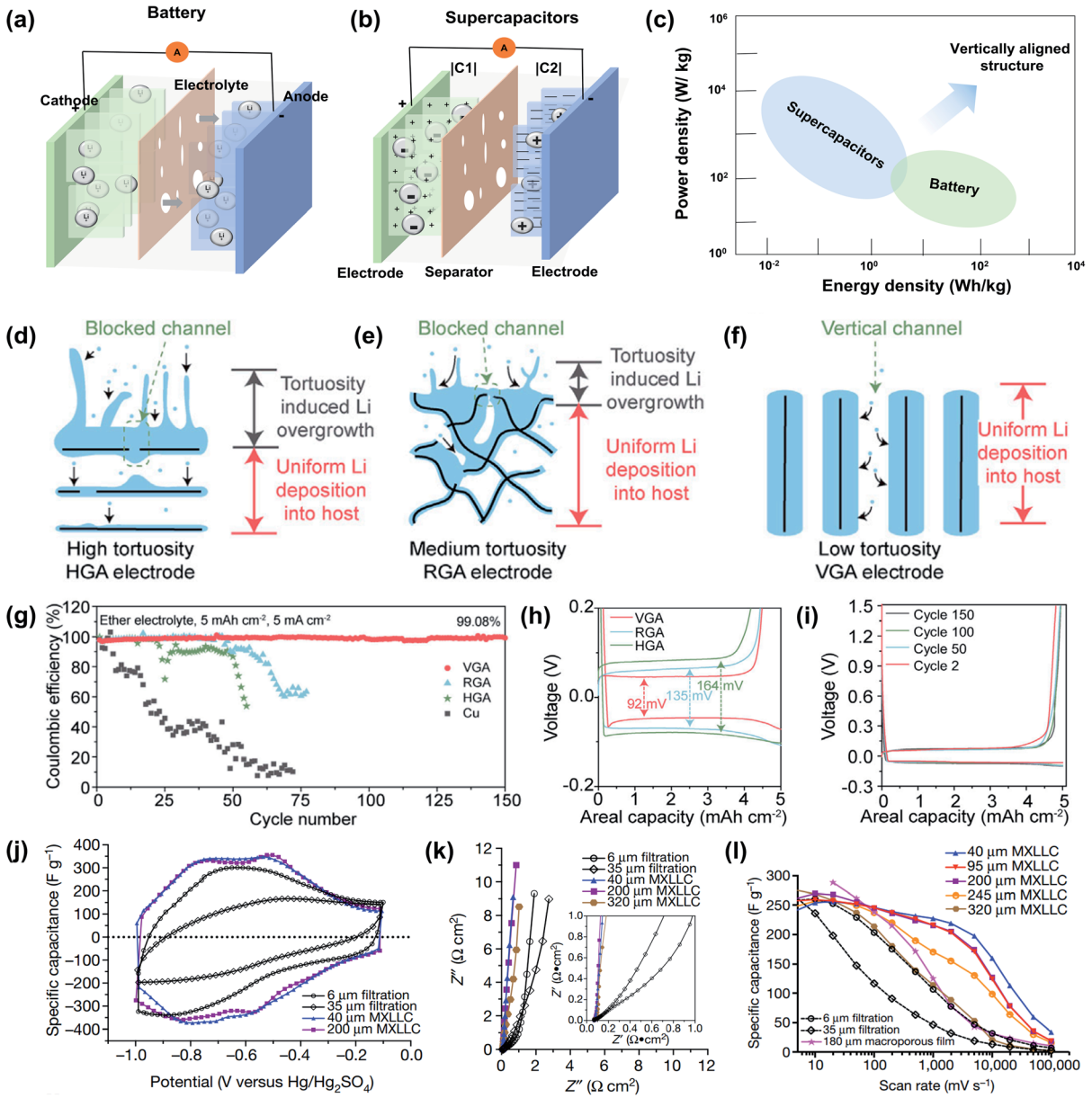

Fig. 6 Schematic illustration of (a) batteries and (b) supercapacitors. C_1 and C_2 refer to the capacity of the cathode and anode. (c) The Ragone plot of batteries and supercapacitors, in which the vertically aligned structure promotes the enhancement of power and energy density. Li-deposition behavior in the structure of the (d) horizontally aligned electrode (HGA), (e) randomly arranged electrode (RGA), and (f) vertically aligned electrode (VGA). Electrochemical performance of the reduced graphene oxide anodes with (g) Li cycling coulombic efficiency (CE) on different anodes with an ether electrolyte at a current density of 5 mA cm^{-2} and a capacity of 5 mA h cm^{-2}. (h) Corresponding voltage-*versus*-capacity plot of different electrodes in the first cycle. (i) Voltage-*versus*-capacity plot of the VGA electrode during different cycles. Reproduced from ref. 123 with permission from Elsevier. Electrochemical performance of vacuum-filtered MXene papers and MXLLC films with (j) cyclic voltammograms at a scan rate of 100 mV s^{-1}. (k) Nyquist plots for different MXene films with real impedance Z' and imaginary impedance Z''. (l) Rate performance of vacuum-filtered MXene papers and MXLLC films at scan rates ranging from 10 to 100 000 mV s^{-1}. Reproduced from ref. 116 with permission from Springer Nature.

cycling Li on the different anodes as shown in Fig. 6g, the HGA electrode showed a decay of the coulombic efficiency (CE) to 90% after 24 cycles, whereas the CE of the RGA electrode decreased to 90% after 48 cycles. In turn, the VGA electrode held a stable CE of ~99.08% after 150 cycles. In the voltage–capacity test, VGA presented a lower overpotential (46 mV) than RGA (67.5 mV) and HGA (82 mV) (Fig. 6h), and held a stable overpotential of ~46 mV even after 150 cycles (Fig. 6i).[121] In another example, an electrode with vertically aligned Fe_3O_4/GO exhibited an energy density of 724 mA h g^{-1} at 2 A g^{-1}, which was much higher than that with the horizontal alignment.[122] Beyond graphene, MXenes also have a large potential for enhanced supercapacitors. Vertically aligned MXenes allow ion transport directly inside the

electrode, which results in thickness-independent electrochemical performances. An example of vertically aligned titanium carbide ($Ti_3C_2T_x$, MXLLC) was achieved by mechanical shearing.[116] The vertically aligned MXLLC exhibited much higher cyclic voltammogram performances than the horizontally aligned film. Furthermore, the Nyquist plots of MXLLC electrodes were nearly vertical at all frequencies, indicating that fast ion diffusion was critical for the independence from the thickness (Fig. 6k). In addition, the rate performance of the MXLLC films declined negligibly when the film thickness was increased from 40 μm to 200 μm (Fig. 6l). Some studies on vertically aligned structures in electrodes for EES are collected in Table 1, which demonstrate the better performance of vertical over horizontally oriented electrodes. These selected examples illustrate how controlling the orientation of 2D nanomaterials enhances the performance of batteries and supercapacitors.

We have seen that controlling the orientation of 2D nanomaterials can enhance the properties and functionalities of sensing and thermoelectric devices, as well as batteries and supercapacitors. These few devices are playing a major role in the development of greener energies, to detect polluting elements or generate energy. The key fundamental reason for the enhancement of the functionalities arises from the conjunction of the outstanding intrinsic properties of 2D nanomaterials with their orientation in a specific direction at the microscopic scale. Even though these various examples are exciting, a number of challenges remain for transposing these properties and enhanced functionalities into real, macroscopic devices, such as scale-up, locally controlled orientation and shaping, which are discussed here. To address these challenges in manufacturing, a number of versatile methods have been systematically investigated, which are reviewed in the following section.

3. Processing techniques for controlled alignment

The desired local orientation direction and global microstructure of a material are determined by what the application demands. Over the recent years, diverse techniques have been established to achieve specific orientations of 2D nanomaterials. We classify these orientation types into horizontal, vertical, heterogeneous, and arbitrary structures. Overall, some methods lead to one of these orientation types, whereas others can produce several, which is the case for example of magnetically assisted orientation and chemical vapor deposition (CVD). The methods that can achieve versatile orientations by tailoring the fabrication parameters will be discussed as arbitrary structural alignment processes. In this section, we give an overview of the most representative processing methods to achieve the four alignment types mentioned earlier using 2D nanomaterials. The advances of different alignment techniques, pivotal control parameters and typical aligned structures are discussed.

3.1 Horizontal microstructures

A material with good horizontal orientation of 2D nanomaterials shows typically exfoliated, dispersed nanosheets that are stacked in a highly ordered aligned structure. In turn, this alignment allows a higher concentration of nanosheets and highly compact assembly. Thanks to this horizontal orientation, the anisotropic nanoscopic properties of the 2D nanomaterial can be transferred to the larger structure. For example, the anisotropic orientation can strengthen the macroscopic material along the aligned direction, while the properties in the perpendicular direction are not affected.[129] The techniques to

Table 1 The electrochemical performance of batteries and supercapacitors produced with vertically aligned 2D nanomaterials as the electrode. The electrode material, the orientation method and the electrode thickness are also featured in the table. The orientation methods are explained in Section 3 of this review

Electrode	Orientation method	Electrode thickness	Cycling stability	Energy power & density	Ref.
3D aligned Fe_3O_4/GO	Freeze-casting	~600 μm	—	724 mA h g^{-1} @ 2 A g^{-1}	122
	Traditional slurry-casting method		—	162 mA h g^{-1} @ 2 A g^{-1}	
$LiFe_{0.7}Mn_{0.3}PO_4$ nanoplates/graphene	Freeze-casting	—	85.6% (450 cycles)	122.3 mA h g^{-1} @ 2C	124
	Traditional slurry-casting method	—	67% (450 cycles)	68.7 mA h g^{-1} @ 2C	
Graphite/sodium carboxymethyl cellulose	Freeze-casting	575–800 μm	—	~18, ~14, and ~7 mA h cm^{-2} @ 0.1C, 0.2C, and 1C	125
$VOPO_4$ nanosheet	Freeze-casting	800 μm	83% (500 cycles)	144 mA h g^{-1} @ 0.2C	126
	Drop-casting		—	122 mA h g^{-1} @ 0.2C	
Graphite	Magnetically aligned casting	—	—	83 mA h g^{-1} @ 2C	120
	No alignment	—	—	23 mA h g^{-1} @ 2C	
$Ti_3C_2T_x$/graphite	Magnetically aligned casting	—	90% (5000 cycles)	60 mA h g^{-1} @ 2 A g^{-1}	127
	No alignment	—	77% (5000 cycles)	16.7 mA h g^{-1} @ 2 A g^{-1}	
$Ti_3C_2T_x$	Freeze-casting	700 μm	97.7% (14 000 cycles)	150 kW kg^{-1} @ 1000 A g^{-1}	128
MXLLC	Shear induced alignment	40–200 μm	100% (20 000 cycles)	220–207 F g^{-1} @ 2000 mV s^{-1}	116
	Vacuum-filtered film	6–35 μm	—	33–77 F g^{-1} @ 2000 mV s^{-1}	

obtain horizontally aligned structures typically are vacuum-assisted filtration, tape casting, wet spinning, centrifugal casting, direct bottom-up synthesis, hot pressing and self-assembly, and are summarized in Table 2. The mechanisms, characteristics and advantages of these techniques are systematically introduced in this section.

3.1.1 Vacuum-assisted filtration. Vacuum-assisted filtration (VAF) or vacuum-assisted self-assembly (VASA) is a flexible technique to synthesise well-ordered and free-standing films or papers.[129] It is one of the simplest and most commonly used methods to achieve horizontal alignment for a wide variety of 2D nanomaterials. Fig. 7a1 illustrates the fabrication process using VAF of a film with horizontally ordered layers, starting from a liquid solution containing dispersed nanosheets. This method utilizes a vacuum-generated flow to filter the nanosheets from an aqueous or organic dispersion over a filtration membrane. In addition, to obtain a homogeneous dispersion in the final layered nanosheets and increase their mechanical properties, a hydrophilic or hydrophobic polymer can be added into the dispersion.[129–131] The mechanism of horizontal alignment *via* VAF is explained by the densification process during solvent removal. In a typical vacuum filtration process, when the solvent is gradually removed, the well-dispersed nanosheets are brought into close contact, leading to the formation of semi-ordered loose aggregates. As the top loose aggregates are exposed to the air–solvent interface, the compression force brings the nanosheets to the perpendicular direction of the flow. The gaps between nanosheets close, resulting in the formation of a compact film.[130] In the end, assisted by VAF, the disordered nanosheets in solution are sequentially aligned parallel to the air–solvent interface (Fig. 7a2–a4). For example, Lin *et al.* synthesized highly aligned graphene oxide (GO) papers by using VAF.[132] Thanks to the ultralarge GO nanosheets (average area of 272.2 μm^2) with compact stacking and well-aligned microstructures, the GO paper achieved more than 3-fold improvement in electrical conductivity and enhanced mechanical properties including Young's modulus by 320% and tensile strength by 280%. Similarly, Ling *et al.* reported flexible and free-standing $Ti_3C_2T_x$ MXene films fabricated by VAF.[133] By tailoring the MXene content in solution, the obtained film thickness can be easily controlled. The as-fabricated $Ti_3C_2T_x$ films could be used as electrodes in supercapacitors because of

Table 2 Processing techniques for horizontal alignment of 2D nanomaterials

Method	Alignment principle	Achieved structure	Advantages	Limitations	Ref.
Vacuum-assisted filtration	Vacuum filtration of colloidal solution to compress the 2D nanosheets horizontally	Film, highly ordered, free-standing layered structure	Wide material selection, inexpensive, simple setup	Time-consuming process, requires low viscosity in colloidal solution	129–134, 146, 172 and 173
Tape casting	Application of horizontal shear force on a viscous solution using a doctor blade	Film, highly ordered, layered structure	Scalable, industrially adaptable	Slow processing	137, 138, 174 and 175
Wet spinning	Extrusion and spinning of a self-assembled colloidal dispersion through a spinneret in a solution bath	Fiber, layered structure	Industrially adaptable, no thermal degradation	Slow processing, requires volatile organic solvents	139, 140, 142 and 176
Centrifugal casting	Casting of a 2D nanosheet dispersion on the inner surface of a rotating hollow tube to align them using centrifugal force	Film, highly aligned, compact layered structure	Wide material diversity, high efficiency, scalable synthesis	Requires specific equipment, with an appropriate inside diameter for efficient centrifugation	57, 144 and 145
Hydrothermal	Heating of an aqueous or organic medium above the boiling point to induce pressure rise and chemical reaction	Nanosheets/film, well-defined aligned layers	High quality nanocrystals, high yield, low cost	Requires specific autoclaves, safety issue during the reaction	153–155
Gelation	Nanosheet hydrogel growth at a solid–liquid interface by an electrochemical reaction	Film, porous layered structure	Simple setup, scalable, controllability of gel structures	Porous morphology, time-consuming process	151 and 156–158
Hot-pressing	Densification process using uniaxial pressure and temperature to simultaneously align and sinter	Film/bulk, closely packed structure	Compact microstructure, improved mechanical properties	Requires specific equipment and operation, limited efficiency	159, 163, 164 and 177
Langmuir–Blodgett (LB) assembly	Spreading of 2D nanosheets at a liquid–air interface which align due to capillary forces	Thin monolayer films	Simple operation, accurate thickness control	Limited resistivity to high temperature, slow deposition	168, 169, 171, 178 and 179

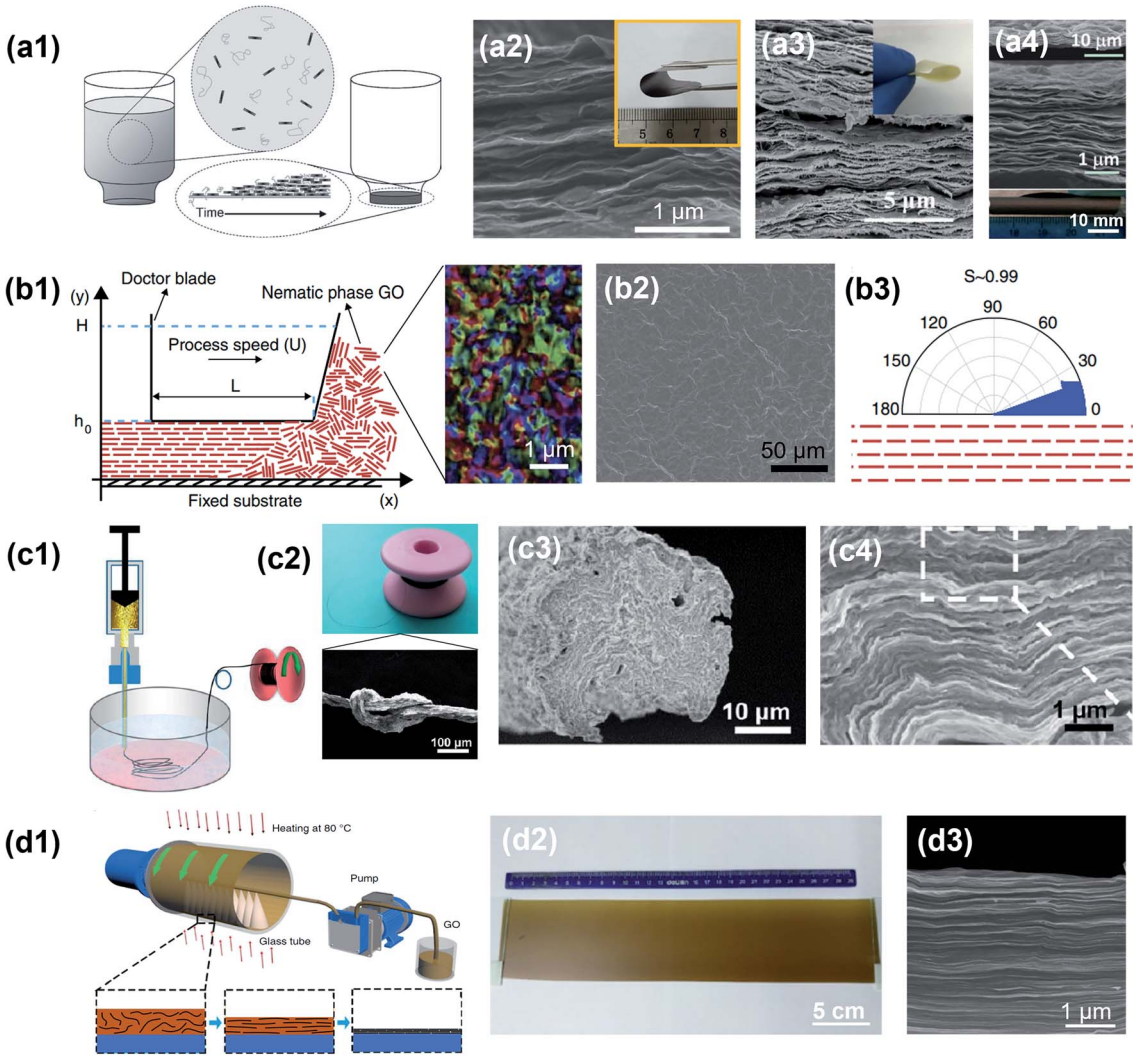

Fig. 7 Horizontal alignment of 2D materials assisted by mechanical force. (a1) Schematic representation of the vacuum-assisted filtration of nano-composite films. Reproduced from ref. 129 with permission from John Wiley and Sons. (a2) SEM image showing the cross section of the horizontally aligned MXene membrane. Reproduced from ref. 134 with permission from Springer Nature. (a3) SEM image of an aramid nanofiber (ANF)/BNNS film with a tightly packed microstructure. Reproduced from ref. 146 with permission from John Wiley and Sons. (a4) Cross-sectional SEM images of flexible free-standing $Ti_3C_2T_x$/PDDA films. Reproduced from ref. 133 with permission from the National Academy of Sciences. (b1) Schematic of tape casting processing of nematic graphene oxide (GO). (b2) SEM image showing the top surface of the shear-aligned GO membrane. (b3) Organization of graphene sheets in membranes. Reproduced from ref. 137 with permission from Springer Nature. (c1) Schematic representation of wet spinning for polyacrylonitrile-grafted GO (GO-g-PAN) fibers and (c2) fabricated GO-g-PAN fibers. (c3 and c4) Cross-sectional SEM images of GO-g-PAN3 fibers with horizontally aligned layers. Reprinted with permission from ref. 139. Copyright (2013) American Chemical Society. (d1) Schematic of the continuous centrifugal casting process. (d2) A GO film with a dimension of ~30 × 10 cm^2 and a thickness of ~100 μm. (d3) SEM image of a GO film showing a highly aligned and compact layered structure. Reproduced from ref. 57 with permission from Springer Nature.

the rapid cation intercalation between the well-aligned layers. Moreover, Ding *et al.* manufactured membranes with a horizontally oriented MXene using VAF.[134] Owing to the regular sub-nanometer spacing between aligned MXene layers, the membrane provided fast and precise molecular sieving channels for gas separation with H_2 permeability higher than 2200 Barrer and H_2/CO_2 selectivity higher than 160. Although the VAF method has multiple advantages such as unlimited material selection, a simple setup and facile control of film thickness, it also has limitations from the time-consuming procedure and prerequisite of low viscosity for efficient filtration, especially when a polymer is involved.

3.1.2 Tape casting. Tape casting, doctor blading or knife coating, is a well-established method to induce shear-induced alignment and to fabricate thin membranes from a viscous slurry.[135,136] The membrane thickness can vary from 0.01 to several millimeters and can be controlled by setting the distance between the doctor blade and the substrate. More importantly, the membrane's lateral dimension is only limited by the shear apparatus, allowing its utilization in commercial production. In a typical slurry preparation, 2D nanosheets or

ceramic precursors are mixed with a solvent, dispersant, binder and plasticizer at a ratio optimized for homogeneity and shear-thinning properties. The procedure is to use a doctor blade to spread out the slurry over a flat substrate (Fig. 7b1).[137,138] Due to the shear generated by the motion of the doctor blade, the initial random orientation of the 2D nanosheets in slurry is overcome and well-aligned layers are formed.[138] For example, Akbari *et al.* introduced tape casting as a scale-up method to fabricate highly ordered graphene-based membranes.[137] The top surface morphologies of the film showed good uniformity and continuity (Fig. 7b2). They further investigated the extent of local orientation as the in-plane stacking order in the membranes using polarized light imaging, where a scalar parameter, S, was used to quantify the alignment extent (Fig. 7b3). This scalar parameter is defined as:

$$S = \frac{1}{2}\langle 3\cos^2\theta - 1\rangle \quad (5)$$

where θ is the angle between the mean azimuth and each pixel. When $S = 1$, the alignment is perfectly oriented in parallel, while $S = 0$ represents a completely random alignment. As a result, the shear-aligned membrane exhibited S values of about 0.99. Their results indicate the potential of tape casting to obtain aligned 2D nanomaterials.

3.1.3 Wet spinning. Wet spinning is a mature technology that is industrially viable. It is a solution spinning process, where a thermoplastic polymer is dissolved in a solvent and extruded through a spinneret to form fibers that consolidate as the solvent evaporates. When it comes to 2D nanomaterials, this technique has been utilized to fabricate fibers which contain layer-stacked nanosheets. In a typical synthesis procedure, the nanosheets are well-dispersed in an organic solvent. Then, the macroscopic assembly of fibers is conducted by continuously spinning into the coagulation bath *via* a spinneret (Fig. 7c1 and c2).[139] When the dispersion passes through the spinneret, a unidirectional flow is generated that assembles the nanosheets horizontally along the fiber direction. The as-fabricated fibers exhibit a dense and layered microstructure containing nanosheets and polymers, which recalls the brick-and-mortar fashion found in natural nacre (Fig. 7c3 and c4). Moreover, it should be noted that the successful alignment of nanosheets is closely related to their liquid crystal self-assembly in the initial colloidal dispersion. The formation of nematic and lamellar liquid crystals with nanosheet colloids is critical in achieving desired alignment, where the material concentration, size and dispersion should be properly controlled.[140–142]

3.1.4 Centrifugal casting. Compared with the previous mechanical force-assisted methods, centrifugal casting is a time efficient method to assemble 2D nanomaterials into highly aligned and compact films.[57,143] For example, it can complete the synthesis of 10 μm-thick graphene oxide films within 1 minute, which provides the possibility of fast processing for industries.[57] Moreover, centrifugal casting is scalable and can produce continuous films up to the meter scale. Fig. 7d1 presents the schematic of the continuous centrifugal casting process of GO nanosheets. In a typical process, the nanosheets are dispersed in solution, which continuously deposits on the inner surface of a hollow tube rotating at speeds up to 2500 rpm. A temperature of about 80 °C can be applied simultaneously to accelerate the solvent evaporation. After reaching the desired thickness and complete water removal, a homogeneous GO film is obtained (Fig. 7d2). Due to the high-speed rotation of the hollow tube, a strong centrifugal force is induced along the radial direction. Meanwhile, the velocity difference between the cast solution and rotating tube generates shear forces along the tangential directions. These forces bring the nanosheets into a compact and highly ordered configuration (Fig. 7d3).[57,144,145]

3.1.5 Bottom-up approaches. Bottom-up approaches are direct ways to synthesize horizontally aligned 2D nanomaterials. They allow the fabrication of films of controlled sizes, thicknesses and orientation, which make them convenient and scalable routes.[15] Besides chemical vapor deposition (CVD), other representative chemical methods that can grow oriented 2D nanomaterials from small molecules are hydrothermal synthesis and gelation growth.[15,147–152] For example, hydrothermal or solvothermal synthesis methods are classical wet-chemical routes for nanomaterials, especially the inorganic ones.[153,154] They are conducted in a sealed vessel, where the reaction medium is water for hydrothermal and an organic solvent for solvothermal reactions. The principle of the synthesis is to heat the reaction medium above the boiling temperature of the solvent to generate high pressure, which leads to the reaction and growth of nanocrystals. By using a hydrothermal method, Xu *et al.* synthesized horizontally aligned 2D hybrid sheets of V_2O_5 and reduced graphene oxide (rGO/V_2O_5) (Fig. 8a1), which can be utilized as cathodes for lithium-ion batteries.[155] As shown in Fig. 8a2, the 2D hybrid sheets exhibited a wrinkled surface, which increased the accessible surface area for ion interaction. In addition, the cross-sectional SEM image revealed well-defined horizontally oriented layers made of 30 nm-thick nanosheets (Fig. 8a3).

Another typical wet-chemical strategy for directional 2D nanomaterial assembly is gelation growth.[151,152] It is a simple and straightforward way to assemble macroscopic structures from nanosheets. For example, Yang *et al.* reported the ordered gelation of graphene hydrogel films from chemically converted graphene in water without the need for additional gelators.[156,157] Later, Maiti *et al.* demonstrated the successful fabrication of reduced graphene oxide films in μm-thick hydrogels with porous and planarly aligned microstructures.[158] To obtain this structure, Zn foils were immersed in a mildly acidic GO dispersion to induce the spontaneous growth of graphene hydrogels on the Zn surface (Fig. 8b1). The mechanism of this spontaneous interfacial gelation can be explained by the reduction process as shown in Fig. 8b2. Because of the lower reduction potential of Zn, there is continuous electron transfer from the Zn metal surface to the GO. As a result, ionized Zn^{2+} tightly attaches to the negatively charged GO nanosheets, leading to layer-by-layer interfacial stacking at the basal planes (Fig. 8b3 and b4). Generally, the gelation growth thickness is controlled by the immersion time: a 78 μm-thick gel film can be typically obtained within one hour. At the same time, the lateral

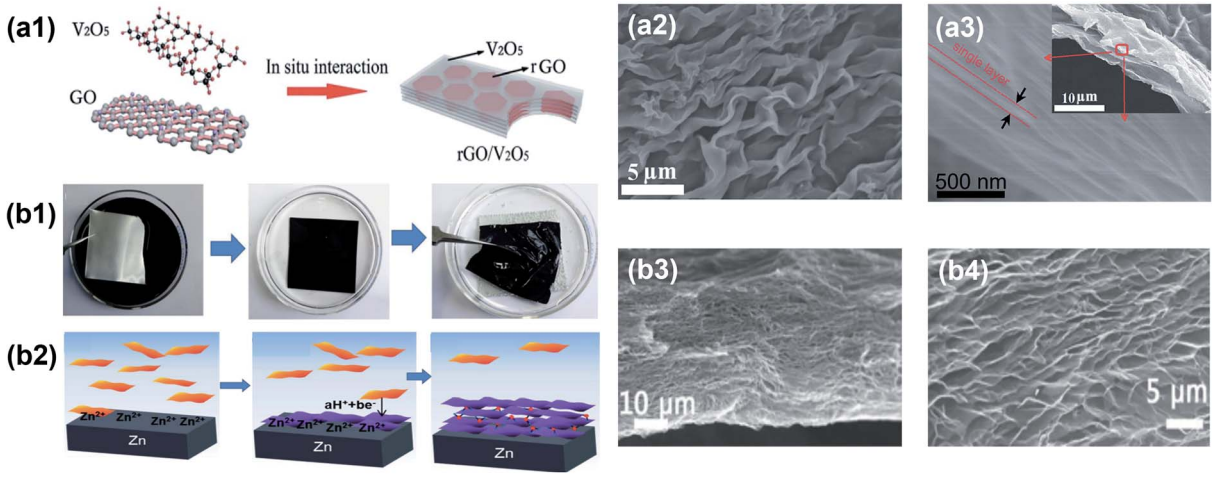

Fig. 8 Horizontal alignment of 2D materials by a bottom-up approach. (a1) Schematics of the hydrothermal fabrication process of rGO/V_2O_5 hybrid sheets. (a2) Top view SEM image of rGO/V_2O_5 hybrid sheets showing a wrinkled surface. (a3) The cross-sectional SEM image showing individual layers. Reproduced from ref. 155 with permission from the Royal Society of Chemistry. (b1) Schematic representation of the interfacial gelation mechanism where a Zn foil (in grey) is immersed in a GO dispersion (black). (b2) Graphene gelation mechanisms at the surface of the metallic foil. (b3 and b4) Morphologies of the graphene aerogels. Reproduced from ref. 158 with permission from John Wiley and Sons.

dimension of the graphene film is determined by the substrate, making the procedure scalable.

3.1.6 Hot-pressing. Hot-pressing, which consists in simultaneously applying heat and pressure, is a popular fabrication method to assemble nanomaterials when high relative density is required. Under uniaxial pressure, a planarly oriented microstructure can be formed from pre-stacked nanosheets. Or in other cases, a self-aligned texture can be formed during sintering due to the uneven stress distribution around nanosheets.[159–162] Using this method, Liu *et al.* fabricated aligned graphene/polycarbonate composites with multiple parallel layers.[163] For planar stacking, each layer thickness was exponentially scaled with successive stacking and folding in a quadrant, and hot-pressing could further improve the interlayer integration (Fig. 9a1). After repeating the process, multilayered graphene composites were obtained, presenting closely spaced and horizontally aligned layers (Fig. 9a2). As a result, the elastic modulus and strength were significantly enhanced at exceptionally low volume fractions of only 0.082%. Other than pre-stacking and compressing, 2D nanomaterials can be alternatively assembled into a complex precursor such as granular particles, where nanosheets are aligned around a sphere, before being hot-pressed. Zhang *et al.* reported a thermally conductive but electrically insulating segregated double network in graphene/h-BN-based composites *via* hot-pressing.[164] Further hot compressing treatment into thinner sheets can improve the intrinsic filler orientation. Additionally, the hot-pressing synthesis procedure is scalable, allowing the fabrication of a dense product with controllable thickness.

3.1.7 Langmuir–Blodgett (LB) assembly. The LB method is a classical interfacial assembly strategy that is performed at the liquid–air interface.[165–168] Typically, molecules or nanosheets are initially dispersed in a water-immiscible volatile organic solvent. Then, the dispersion is spread dropwise onto the water surface. After the solvent has evaporated, a water-supported thin layer is formed, which can be later transferred to a substrate and compressed. When it comes to controlled horizontal alignment of 2D nanosheets, the LB method has been further developed by tuning the dewetting instability of the wet monolayer upon transferring, which involves the wet transition from complete to partial wetting. Consequently, the alignment and patterning design of 2D nanomaterials can be accessible without an additional template.[169–171] Kim *et al.* investigated the edge-to-edge interactions between neighbouring graphene oxide sheets *via* LB assembly.[168] In this case, the water surface was utilized as an ideal platform to assemble the 2D nanosheets. To improve the spread capability of nanosheets by LB methods, Nie *et al.* developed a general method by combining it with electrospray (Fig. 9b1).[169] Benefiting from the reduced volume of the aerosolized droplets, the diminished droplets are depleted rapidly in the initial spreading and leave all the nanoparticles on the water surface, leading to efficient LB assembly as shown in Fig. 9b2.

3.2 Vertical microstructures

The anisotropic properties of 2D nanomaterials are some of the most critical features to achieve unique functionalities. When they are aligned vertically, the 2D nanosheets can provide more reaction sites from the exposed edges as compared to when they are horizontally aligned. Also, the increased surface area resulting from vertical alignment in a forest-like configuration can for example lead to more efficient conduction pathways. In this section, we review several representative strategies to achieve the vertical alignment of 2D nanomaterials. The typical processing, achieved structures, advantages and limitations of the techniques are tabulated in Table 3. Some universal techniques are capable of conducting diverse aligned patterns including horizontal and vertical structures and will be tackled in the arbitrarily aligned section.

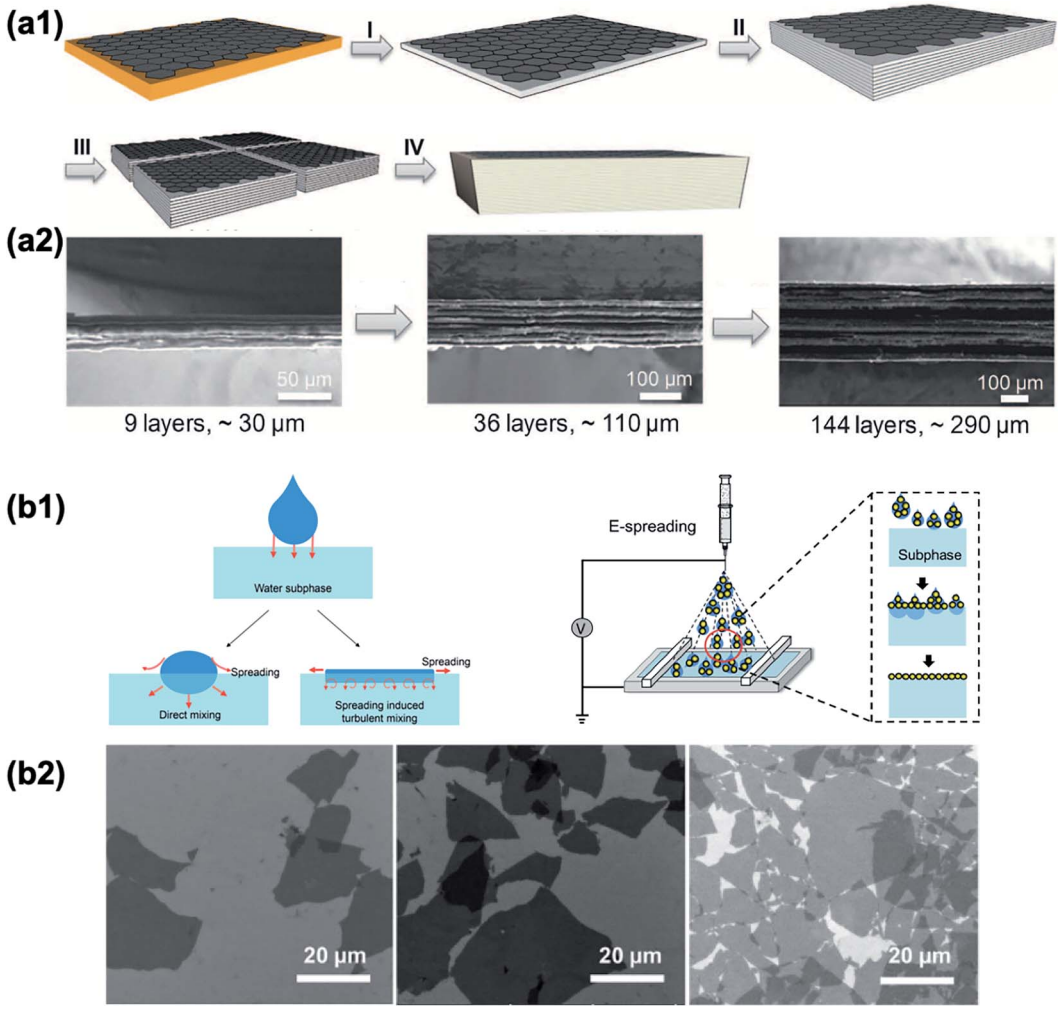

Fig. 9 Horizontal alignment of 2D nanomaterials by (a) hot-pressing and (b) Langmuir–Blodgett assembly. (a1) Stacking and hot-pressing method for planar composites. (a2) SEM images of the planar composites with different layer thickness. Reproduced from ref. 163 with permission from the American Association for the Advancement of Science. (b1) Schematic representation of a conventional Langmuir–Blodgett process and electrospray. (b2) Water-dispersed graphene sheets on a Si wafer by electrospray at increasing surface pressures. Reprinted with permission from ref. 169. Copyright (2015) American Chemical Society.

3.2.1 Shear force. Achieving vertical alignment of 2D nanomaterials is considered more difficult than horizontal alignment since gravitational forces need to be overcome. Shear resulting from flow-induced fluctuations in smectic or lamellar self-assembled colloidal phases is one effective route. This shear-induced orientation depends on the torque that is generated perpendicularly to the shear direction.[116,180] Tape casting is a typical technique to shear. Assisted by tape casting, highly ordered horizontal structures have been obtained as mentioned above (Fig. 7b). Nevertheless, tape casting can also lead to vertical alignment of 2D nanosheets under controlled conditions (Fig. 10a1). When 2D nanosheets are well-dispersed in aqueous solution, long-range oriented mesophases spontaneously form as discotic liquid crystal phases, where the nanosheets are aligned parallel to each other.[140,181] Under external mechanical shear, a vertical torque arising from the flow-induced fluctuation is generated, which orients the aligned nanosheets in the mesophases, vertically (Fig. 10a2 and a3).[116,180,182] The applied shear rate for vertical orientation should be adjusted according to the particle size, with larger particles requiring a lower shear rate.[116] Furthermore, extrusion is another method to induce shear. As one of the most commonly used processing techniques in the plastics industry, it is also suitable for orienting 2D nanomaterials having high anisotropy.[183] A typical extrusion process is illustrated in Fig. 10b1. The critical control parameters to achieve good distribution and orientation of 2D nanosheets include a relatively low processing temperature, suitable draw ratios (the ratio between extrudate pulling velocity and average velocity in the extrusion die), sufficiently high local shear rates and shear stresses inside the die for orientation. After extrusion, cutting along the transverse section is required to reveal the vertically aligned nanoflakes (Fig. 10b2). By providing a biaxial stress field by combining rotation and extrusion, the 2D nanoflakes could be further assembled into perpendicular alignment to the radial direction (Fig. 10c1–c3).[184]

Table 3 Processing techniques for vertical alignment of 2D nanomaterials

Method	Alignment technique	Achieved structure	Advantages	Limitations	Ref.
Tape casting	Induction of vertically oriented torque by horizontally shearing with a blade on solution containing liquid-crystalline nanosheets	Film, vertically packed nanosheets	Scalable, nearly thickness-independent	Slow processing	116, 180, 182 and 185
Extrusion	Alignment of 2D nanoparticles along the extrusion direction through a die and cutting perpendicularly to this die	Tube, vertically oriented nanosheets	Flexible alignment direction	Requires specific equipment and post-processing (cutting)	119 and 183
Laser irradiation	Irradiation of a high energy laser on the surface of a nanosheet film to induce local compression forces	L-shaped nanostructures in thin films	One-step process, local control enabling patterning possibility, reduces nanosheet defects	Requires equipment for laser generation	186
Hydrothermal/ solvothermal synthesis	Bottom-up nanostructure growth on a substrate in solution	Film, direct vertical alignment, densely packed nanostructure	Versatile and cheap, direct growth of nanostructures, low reaction temperature	Requires autoclave equipment and proper safe operation	192, 200 and 202
Templated growth	Template induced nanostructure crystallization and growth on pre-fabricated supports	Film, densely packed nanostructure	Tunable particle size, highly interconnected nanostructures	Requires pre-fabricated templates and precise control of template growth	58 and 201

3.2.2 Laser irradiation. Laser irradiation is a newly developed technique to process and orient 2D nanomaterials.[186–188] Thanks to the recent development of a diverse range of lasers, laser irradiation as a method to process nanomaterials is blooming.[189–191] Different from most conventional material processing techniques, laser irradiation imparts rapid heat and localized high energy to materials, allowing precise control over the material microstructures.[188] Park *et al.* reported the fabrication method of L-shaped graphene nanostructures with a vertical alignment and reduced defect level through laser irradiation.[186] Fig. 11 presents the fabrication process of laser-induced L-shaped graphene nanostructures. Initially, a horizontally aligned GO film was prepared by filtration. Then, as the laser irradiated the surface of the horizontally stacked GO film, compression stresses generated because of thermal expansion of individual GO nanosheets. As a result, the GO nanosheets were locally re-aligned in the vertical direction. Also, the high energy density from CO_2 lasers could even heal the defects within the graphene nanosheets by removing the oxygen-containing functional groups. The as-fabricated L-shaped graphene nanoarchitectures exhibited high hydrophobicity, excellent electron transport and thermal conduction due to the localized vertical orientation and lower defect level.

3.2.3 Hydrothermal and solvothermal synthesis. The hydrothermal and solvothermal synthesis strategies introduced in Section 3.1.5 to produce horizontal layers (Fig. 8a) can also create vertically aligned nanosheets. Through a hydrothermal reaction, vertically aligned nanosheets have been grown on various substrates under well-controlled growth parameters and are applicable to diverse material types and geometries such as nanowires, nanospheres, nanosheets, and nanoribbons.[192–196] Generally, the morphology of the grown nanostructures can be tuned by controlling the template seed growth, reaction temperature, pH and by adding surfactants.[197–199] Fig. 12a1 displays a typical solvothermal synthesis procedure for vertically oriented VO_2(B) nanobelts.[200] Before solvothermal growth, a thin layer of vertically oriented graphene was grown on a flat substrate by plasma enhanced CVD, which improved the vertical growth of the nanobelts into a forest structure with enhanced densification. Later, the precursor slurry was loaded on the graphene coated substrate in an autoclave, in which the densely packed nanostructure self-assembled with a vertical orientation as shown in Fig. 12a2 and a3. Similarly, vertical alignment of α-MoO_3 nano-blades was achieved by the hydrothermal method (Fig. 12b1). The obtained nano-blades were arranged in rows and bundles, showing a flower-like structure. The individual nano-blades were 10 to 50 nm-width without stacking onto each other (Fig. 12b2 and b3).

3.2.4 Templated growth. The synthesis of vertically aligned 2D nanosheets can also be implemented by the self-assembly of sacrificial particles called templates. Typically, the nanostructures fabricated by template induced self-assembly exhibit highly interconnected nanostructures, strong interface adhesion, good structural robustness, *etc.* For example, Zhu *et al.* investigated a general salt-templating method that led to vertically oriented graphitic carbon nanosheets.[201] Fig. 12c1 presents the schematic illustration of the salt-templating process. In short, the precursor was mixed with a $ZnCl_2$ and KCl salt

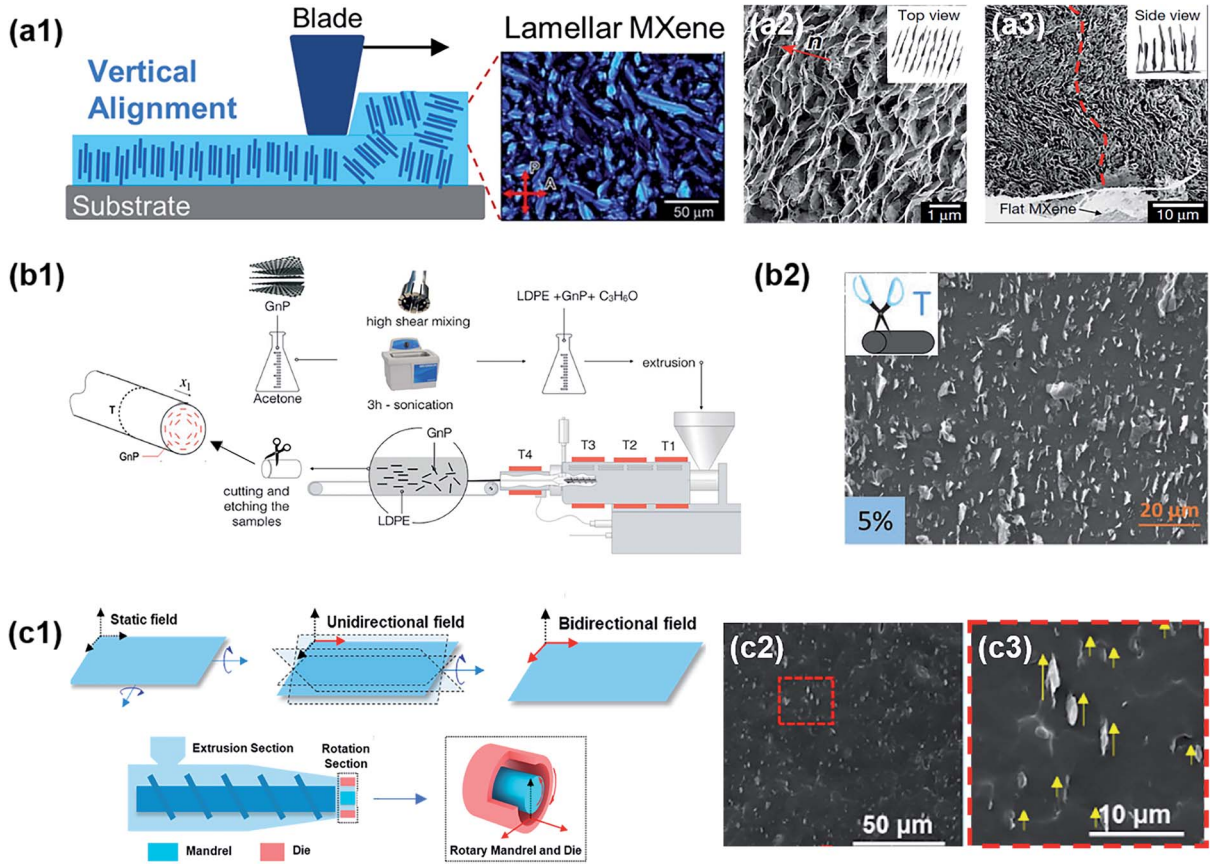

Fig. 10 Vertical alignment of 2D nanomaterials assisted by shear force. (a1) Schematic representation of tape casting of liquid-crystalline $Ti_3C_2T_x$. Reproduced from ref. 185 with permission from Elsevier. (a2) Top view SEM image of the MXene lamellar liquid crystal (MXLLC). (a3) Side view of vertical MXene nanosheets. Reproduced from ref. 116 with permission from Springer Nature. (b1) Schematic representation of the extrusion process of graphite nanoplatelet (GNP) and polyethylene (LDPE) nanocomposites. (b2) Surface morphology of the extruded GNP–LDPE composite with the transverse section. Reproduced from ref. 183 with permission from John Wiley and Sons. (c1) Schematic illumination of the rotation extrusion equipment. (c2) Cross-sectional SEM images of the extruded composites. (c3) Magnified area of (c2) in which yellow arrows refer to the nanofiller alignment direction. Reproduced from ref. 184 with permission from Elsevier.

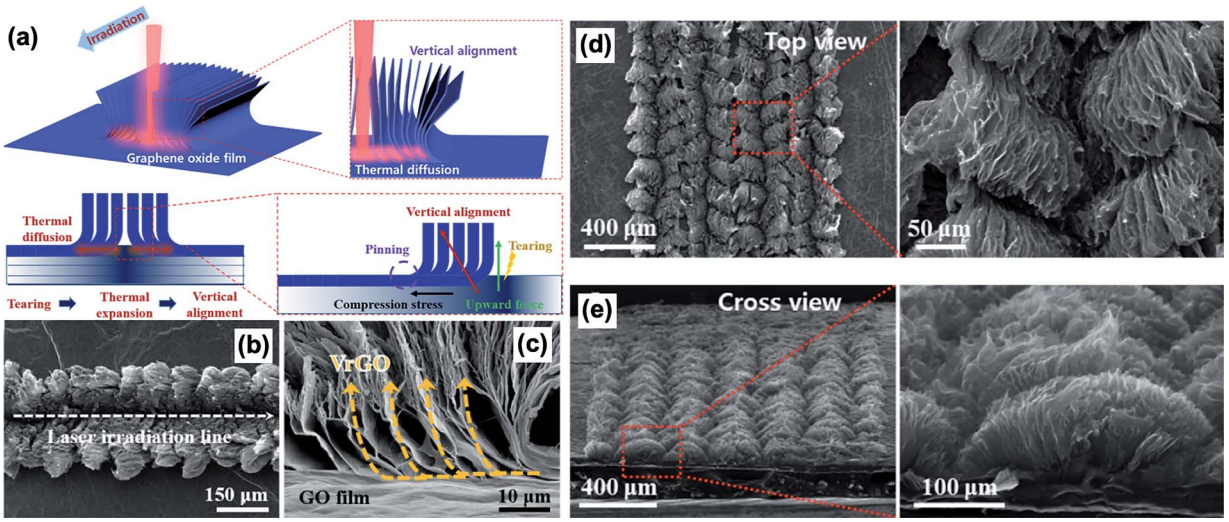

Fig. 11 Vertical alignment of reduced graphene oxide nanosheets by laser irradiation. (a) Schematic of the CO_2 laser irradiation fabrication process of the vertically aligned nanostructure. (b and d) Top view of the vertically aligned nanosheets. (c and e) Cross-sectional view of the as-fabricated nanostructure. Reproduced from ref. 186 with permission from Elsevier.

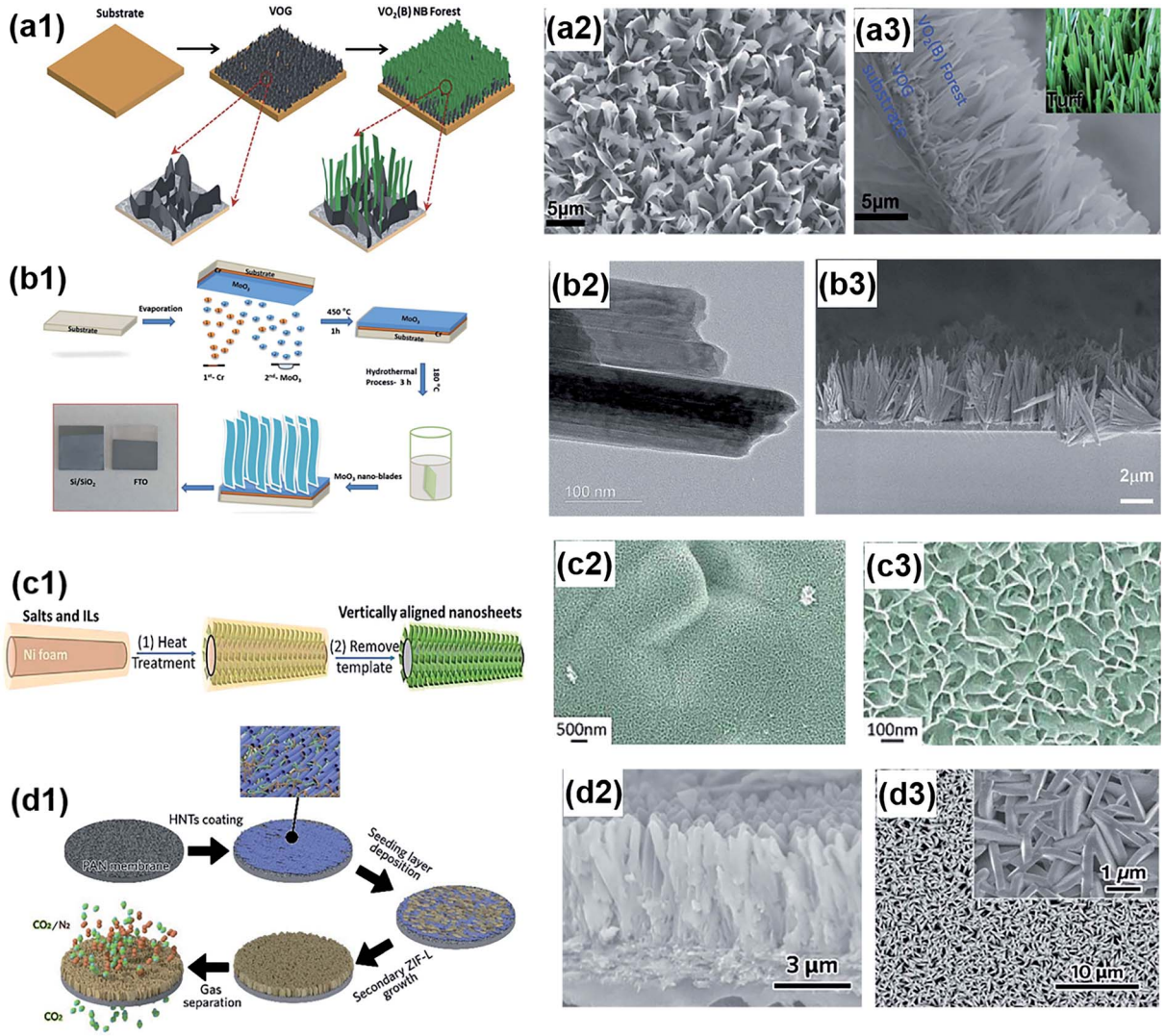

Fig. 12 (a1) Schematic showing the solvothermal synthesis of VO_2(B) nanobelts (NB) on a vertically oriented graphene (VOG)-coated substrate. (a2) Top morphology of aligned VO_2(B) nanobelts. (a3) Cross-sectional SEM image of grown VO_2(B) nanobelts. Reproduced from ref. 200 with permission from the Royal Society of Chemistry. (b1) Schematic representation of the hydrothermal synthesis process of vertically aligned α-MoO_3 nano-blades. (b2) HRTEM image of α-MoO_3 nano-blades. (b3) SEM image showing vertical alignment of α-MoO_3 nano-blades. Reproduced from ref. 192 with permission from the Royal Society of Chemistry. (c1) Schematic illustration of the salt-templating process for vertically aligned 2D nanosheets. (c2 and c3) Typical morphologies of the grown graphitic carbon nanosheets. Reprinted with permission from ref. 201. Copyright (2015) American Chemical Society. (d1) Schematic illustration of the halloysite nanotube (HNT) modification on a polyacrylonitrile (PAN) membrane and templated growth of vertically aligned zeolitic imidazolate framework-L (ZIF-L) 2D MOF nanosheets. (d2) Cross section and (d3) top surface of the vertically aligned MOF membrane. Reproduced from ref. 58 with permission from the Royal Society of Chemistry.

mixture before being coated onto a nickel foam substrate. After heat treatment and template removal, vertically aligned and highly interconnected nanosheets were obtained (Fig. 12c2 and c3). In this case, the formation of vertical orientation of the 2D nanosheets could be attributed to two reasons. One is the nickel induced dissolution and crystallization of carbon on the surface of the substrate, leading to the directional growth of graphitic carbon distal to the surface. The other reason is that the salt mixture acts as a porogen and helps in forming separated flat structures. In another example, Li *et al.* reported templated growth of vertically aligned 2D metal–organic framework (MOF) nanosheets (Fig. 12d1–d3).[58] To achieve the nanocrystal orientation, a layer of horizontally aligned 1D halloysite nanotubes was deposited as the nucleation sites for 2D MOF nanosheets. This pre-fabricated layer also plays a role in guiding the vertical growth of nanosheets.

3.3 Heterogeneous microstructures

Beyond purely horizontal or vertical alignment, the creation of more complex microstructures with ordered 2D nanomaterials can also generate novel functionalities. The heterogeneous architectures are typically beneficial for enhancing interfacial interactions of ion diffusion by increasing the density of reaction sites, which may facilitate applications such as catalysis,

Table 4 Processing techniques for heterogeneous microstructures with 2D nanomaterials

Method	Alignment technique	Achieved structure	Advantages	Limitations	Ref.
Crumpling	Induction of compressive stresses in a film of horizontally aligned nanosheets	Crumpled film	Facile method, controllable crumpled patterns	Limited scale (*e.g.*, micrometer-scale), time consuming	59 and 207–209
Scrolling	Scrolling of layered nanosheets into fibers	Fiber, spiral structure	Simple procedure, high packing density, unlimited material type	Requires precise operation	118, 163 and 212
Layer-by-layer assembly	Sequential deposition of individual layers into a multilayer structure	Film, multiple layers	Simple procedure, low cost, precise film thickness control	Requires strong interaction between individual layers, slow fabrication speed	129, 213, 216 and 219
Freeze-drying assisted self-assembly	Self-assembly of liquid crystals under appropriate conditions	Film/bulk	Simple procedure, inherently interconnected microstructure	Requires precise control of liquid crystal alignment conditions	205, 218 and 220

energy storage and so on. In this section, we review several emerging approaches used to fabricate heterogeneous microstructures as summarized in Table 4. By using different synthesis technologies, diverse periodic textures and microstructures can be effectively tuned.

3.3.1 Crumpling. 2D nanomaterials have a large surface area and tunable surface functionalities. They are much easier to bend or fold than stretch in the planar direction, leading to morphological surface instability.[203,204] This mechanical instability has been further utilized to create 3D crumpled architectures with the assistance of external stimuli. Crumpled graphene films, as an example, are extensively studied for energy storage, electronics, biomedicine, *etc.*, where the crumpling degree is pivotal in determining their performances.[205,206] To crumple a graphene film, this film is first adhered on a pre-stretched elastomeric polymer substrate or any other substrate able to shrink. When the substrate relaxes, it shrinks, inducing compression in the graphene layer that crumples due to its high stiffness (Fig. 13a1).[59,207–209] Furthermore, the substrate shrinkage can be controlled to be isotropic or anisotropic. For isotropic shrinkage, the sample is simply annealed without mechanical stress, showing a flower-like crumpled morphology

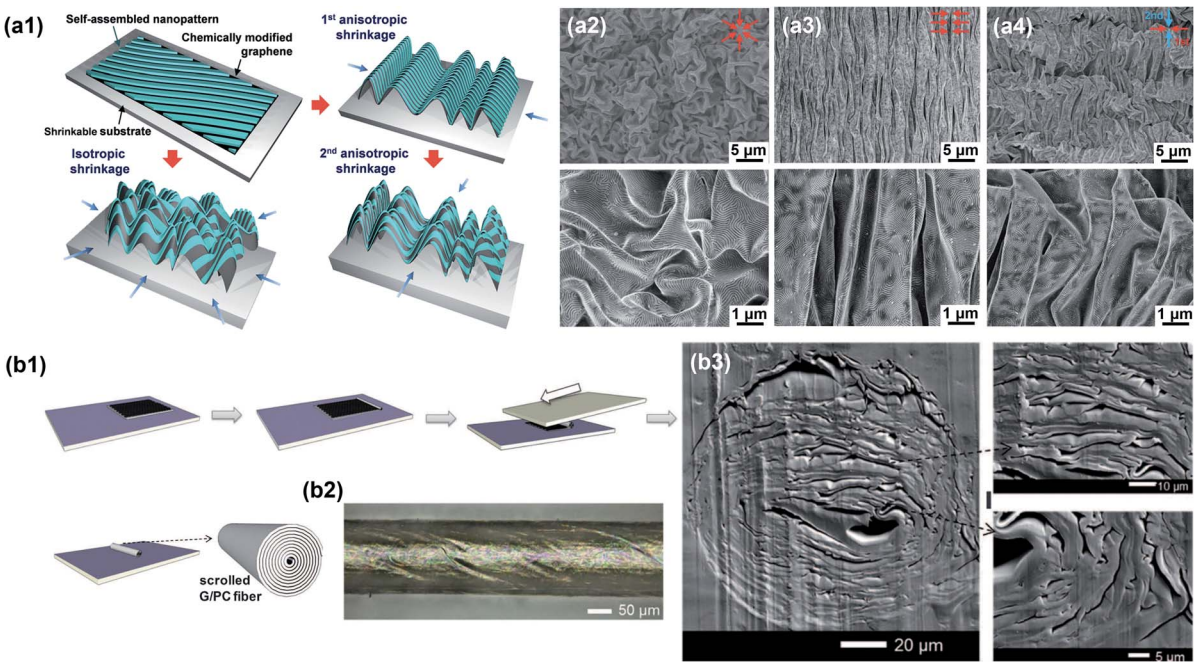

Fig. 13 Heterogeneous graphene nanostructures created by (a) crumpling and (b) scrolling. (a1) Schematic illustration of crumpling for a self-assembled nanopattern. SEM images of (a2) isotropically, (a3) uniaxially, and (a4) hierarchically crumpled graphene with different shrinkage directions specified in red arrows. Reproduced from ref. 59 with permission from John Wiley and Sons. (b1) Schematic illustration of scrolling the graphene/polycarbonate (G/PC) nanocomposite. (b2) Optical microscope image of the scrolled fiber. (b3) Cross-sectional SEM images of the scrolled fiber. Reproduced from ref. 163 with permission from the American Association for the Advancement of Science.

(Fig. 13a2). As for anisotropic, uniaxial and hierarchical crumpling, the relaxation of the substrate is conducted by anchoring one of its side during the shrinkage (Fig. 13a3 and a4).[59] The crumpled patterns are typically on a sub-micro scale, which are applicable for various applications such as electrochemical catalysis, strain sensors and stretchable conductors.[210,211] The crumpling method could be more suitable for synthesizing small sample sizes rather than scalable products to precisely control the shrinkage of substrates.

3.3.2 Scrolling. Scrolling is a simple way to assemble 2D nanomaterials into fibers with a heterogeneous structure, which typically shows a spiral cross section. It provides broad material selection without specific requirements of the composition, chemical bonding or nanomaterial dimension. During scrolling, a planar film containing ordered nanosheets is rolled into a cylinder. The dimensions and intrinsic microstructure of the cylinder can be easily controlled by varying the initial film parameters, such as thickness and orientation.[118,163] Fig. 13b1 provides an example of the transverse shear scrolling method. Liu *et al.* demonstrated the feasibility of this method for fabricating closely packed spiral microstructures in graphene-based nanocomposites (Fig. 13b2 and 13b3).[163] The scrolled graphene nanocomposites with a heterogeneous structure exhibited anisotropic electrical conduction along the graphene planar axis with electrical conductivity about 4 S cm^{-1} at a low volume fraction of about 0.185%, and the transparency was maintained at the same time. Similarly, Chen *et al.* reported the fabrication of tightly packed and interconnected BN nanosheet composites using scrolling.[212] These nanocomposites exhibited an enhanced through-plane thermal conductivity of 1.94 W m^{-1} K^{-1} with 15.6 vol% BN nanosheets, which are beneficial for thermal management applications. The heterogeneous structures of 2D nanomaterials synthesized by scrolling are typically fibers on a micro- or milli-meter scale, which are still challenging for industrial fabrication.

3.3.3 Layer-by-layer (LBL) assembly. Layer-by-layer (LBL) assembly is one of the most extensively used methods for synthesizing nanocomposites with heterogeneous compositions and structures at high filler loadings. It consists in assembling individual layers of nanoparticles in a sequential manner, thereby allowing for the fabrication of building heterogeneous structures composed of different components. LBL assembly is thus a versatile approach to combine individual layers of various morphologies or different material types, where the film thickness can be precisely controlled.[213–215] In practice, the LBL assembly is realized using dipping, spinning or spraying as shown in Fig. 14a1–a3. In a typical LBL dipping assembly procedure, a substrate is sequentially immersed into colloidal solutions containing nanosheets. A heterogeneous film with a multilayer structure can be formed by repeating the dipping process.[320] The formation of a layered structure with high ordering is closely related to the strong interactions

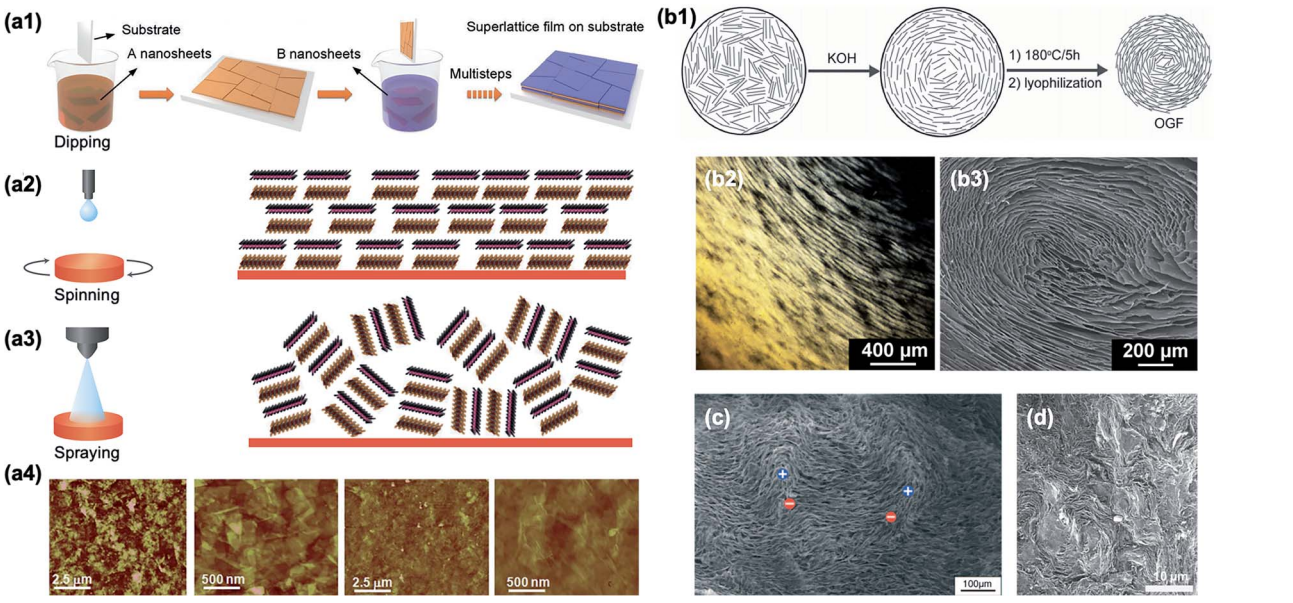

Fig. 14 Fabrication approaches of heterogeneous structures. (a1) LBL assembly of oppositely charged nanosheets by dipping. Reproduced from ref. 219 with permission from John Wiley and Sons. Schematic illustration of various LBL methods *via* (a2) spinning and (a3) spraying. Reproduced from ref. 213 with permission from Springer Nature. (a4) AFM images showing the surface morphologies of rGO multilayers fabricated by spin coating. Reproduced from ref. 216 with permission from the Royal Society of Chemistry. (b1) Schematic illustration of the self-assembly of ordered graphene foams (OGFs) by tuning the pH value. (b2) Polarized-light optical microscope (POM) image of GO suspension near the inner surface of the glass tube. (b3) SEM image showing the heterogeneous structure of OGFs. Reproduced from ref. 218 with permission from John Wiley and Sons. (c) SEM image of a graphene oxide liquid crystal treated by freeze-drying. Blue and red symbols represent +1/2 and −1/2 disclinations, respectively. Reproduced from ref. 220 with permission from John Wiley and Sons. (d) SEM image of a self-assembled MXene liquid crystal. Reproduced from ref. 116 with permission from Springer Nature.

between individual components, such as electrostatic force, covalent bonding, hydrophobic interaction and so on.[129,213] To guarantee high LBL packing, the deposited material components should be selected to bound together. This can be improved by introducing surface modifications such as functional groups or surfactants. For example, Lee *et al.* utilized the spin coating LBL method to assemble positively charged rGO and negatively charged rGO as one bilayer. A multilayer structure with 10 bilayers was obtained by repeating the procedures (Fig. 14a4).[216] The size and thickness of the fabricated structures are set by the substrate dimensions and repeat times, respectively, which provide the possibility for scale-up applications.

3.3.4 Freeze-drying assisted self-assembly. 2D nanomaterials with high aspect ratios can be self-assembled into aligned domains when they are in the liquid crystal form. Liquid crystals (LCs) are particles in the intermediate state between an amorphous liquid and crystalline solid. LCs therefore exhibit mobility and self-assembled ordering under competing driving forces from packing and orientation entropies. The LC size, concentration, repulsion and solvent viscosity greatly influence their self-assembling behavior.[217] Furthermore, with the assistance of freeze-drying, which provides rapid growth of ice crystals, the self-assembly of 2D nanosheets from dilute LC suspension can be induced by concentrating the LCs between the crystals. As an example, Yao *et al.* organized GO nanosheets into LCs with high heterogeneous orientations by increasing the pH value of their dispersion with potassium hydroxide (KOH) (Fig. 14b1).[218] The self-assembled nanosheets exhibited an inherently interconnected microstructure. In strong alkaline bases such as KOH, the enhanced electrostatic repulsion between GO sheets could be increased, leading to higher fluidity and a highly ordered texture. After hydrothermal reduction of GO LCs and subsequent freeze-drying, a spiral microstructure with better aligned nanosheets was obtained mainly due to the alignment of GO nanosheets in LCs along the inner surface of the container (Fig. 14b2 and b3). More examples of self-assembled macroscopic orientation of liquid crystals can be found in Fig. 14c and d. Overall, the freeze-drying assisted self-assembly method involves simple procedures but may be limited in scalability and material diversity because it requires more strict control of nanomaterial selection and operation with a suitable size, aspect ratio, materials chemistry and fabrication parameters to achieve desirable assembled microstructures.

3.4 Arbitrary microstructures

The orientation and distribution of 2D nanomaterials are key factors that determine the macroscopic performances of films and bulk materials made from them due to their anisotropic properties. These performances include mechanical, electrical, thermal, optical properties and so on. Therefore, methods capable of controlling the microstructure in predesigned orientation patterns are highly desirable. The methods that can create arbitrary microstructures are therefore reviewed in this section, and their representative features are summarized in Table 5. Through these technologies, a variety of aligned patterns can be achieved within a single method, allowing materials with a highly tunable local orientation and versatile properties.

3.4.1 Magnetic field assisted orientation. A magnetic field is a powerful tool in precisely and remotely controlling the local orientation of anisotropic particles, including 2D nanomaterials.[60,220,221] This approach utilizes external magnetic fields to align particles with anisotropic magnetic susceptibility suspended in a liquid matrix.[222,223] As 2D nanomaterials are often diamagnetic, extremely high magnetic fields are usually required for alignment.[222,224] To solve this problem, superparamagnetic nanoparticles such as iron oxide nanoparticles can be coated on the surface of the nanosheets to make them more responsive to magnetic fields.[225,226] During magnetic alignment in suspension, the dynamics of particles is synergically controlled by torques generated from the magnetic, gravitational, and viscous forces. Several key factors can influence

Table 5 Processing techniques for arbitrary orientation

Method	Alignment technique	Achieved structure	Advantages	Limitations	Ref
Magnetic field	Application of external magnetic fields to align 2D nanosheets having anisotropic magnetic susceptibility	Bulk/film, highly tunable localized orientation	Low cost, applicable to a wide material type, any orientation angle	Limited scaffold density, the sample dimension is limited by the magnet size	42, 60, 222 and 225
Electric field	Application of an external electric field to align 2D nanosheets having anisotropic electric susceptibility	Bulk/film, tunable control of local particle alignment	Low cost, scalable, facile to tune electric field distribution	Requires dielectric polarization and requires a multi-step process for complex patterns	231–233
Freeze casting	Control nucleation and directional growth of ice crystals under temperature gradients to push the 2D nanosheets into patterns	Bulk/film, porous scaffolds, well-orientated patterns	Applicable to a wide range of materials, scalable, tunable microstructures of freeze-cast scaffolds	Limited scaffold density, requires precise control of solidification front growth	49, 240–242 and 255
CVD	Gaseous chemical reaction and solid deposition on a substrate surface	Film, tunable aligned structure through growth conditions	Scalable, high material quality	Limited layer thickness, cannot change orientation angle freely	55, 247–249, 251 and 252

the particle orientation, including the particle geometry, magnetic field strength and gradient, particle concentration and fluid viscosity. After positioning the particles, the fluid is consolidated to fix the orientation, which can be achieved by solvent evaporation, light or temperature-controlled curing, depending on the solvent type.[42,223,226–228] To create complex local assemblies, virtual magnetic molds can be used.[319] These molds consist in placing a ferromagnetic material above a magnet. The ferromagnetic material then becomes magnetized and attract the particles locally. Combined with a dynamic magnetic field instead of a static field, 2D particle orientation in set directions with a local particle concentration can be achieved. Fig. 15a shows the alignment process of gelatin-based composites containing magnetically responsive reduced graphene oxide (m-rGO) flakes.[60] By controlling the magnet placement and by using a virtual magnetic mold made of a Co or Ni template, both the orientation and spatial distribution of m-rGO flakes can be effectively tailored within the composites. By choosing predefined meshes as the template, the m-rGO flakes could be assembled into hierarchical double-percolating networks (Fig. 15b), enabling both optical transparency and electrical conductivity at a reduced percolation threshold of 0.65 to 0.85 vol% of rGO. In addition, Lin *et al.* demonstrated the magnetic response and alignment of graphene flakes, where the displayed patterns of graphene suspension were induced by different shapes and configurations of magnets (Fig. 15c–f).[222] Later, when the static magnetic field was switched to a rotating magnetic field in the *x*–*y* direction (Fig. 15g), the graphene nanosheets were aligned in the planar direction, exhibiting much higher birefringence and anisotropic absorption/transmission capabilities than those without a magnetic field or with a static magnetic field (Fig. 15h–j). Overall, the magnetic orientation of 2D nanomaterials is applicable to a wide range of material chemistry and the orientation angle can be easily programmed by

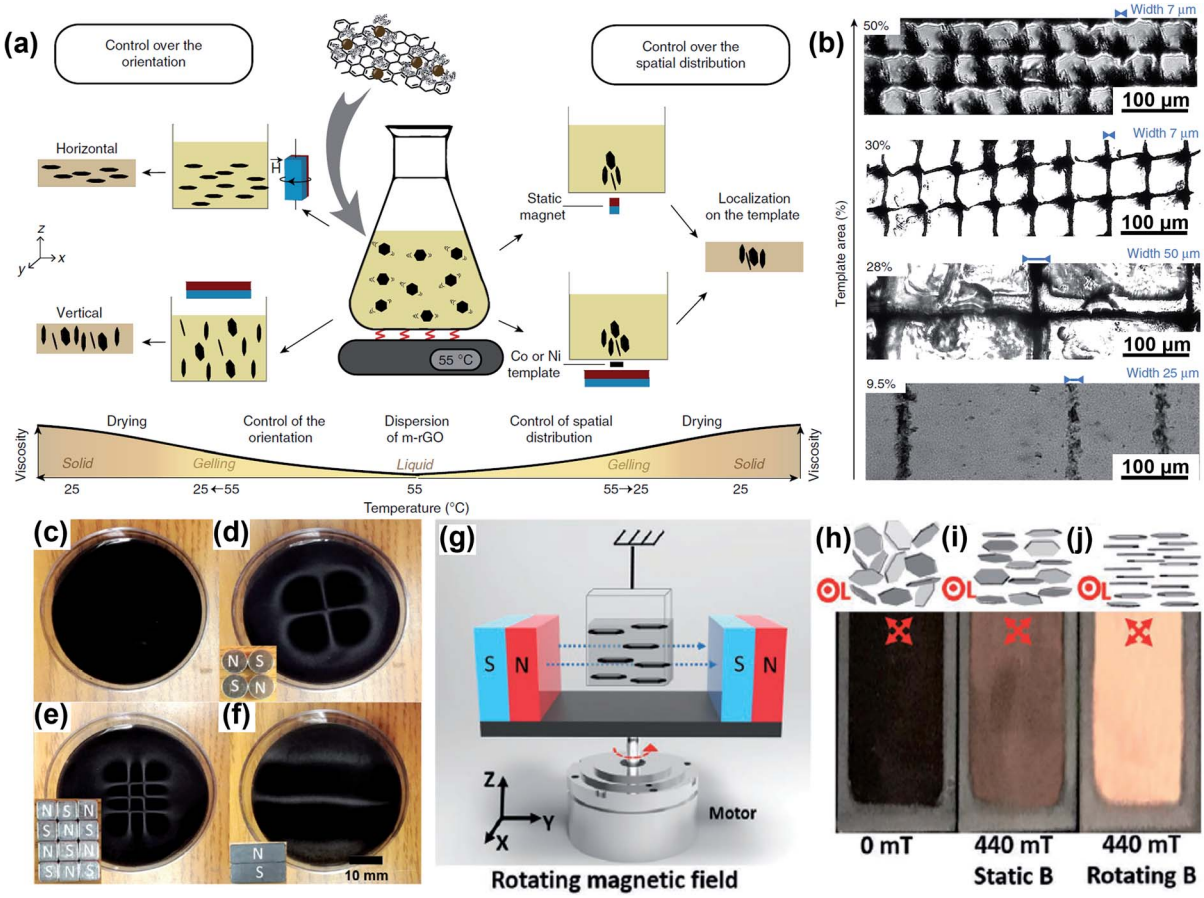

Fig. 15 Controlled orientation of 2D nanomaterials assisted by a magnetic field. (a) Schematic illustration of magnetic control over the orientation or spatial distribution of magnetized reduced graphene oxide (m-rGO) flakes. (b) Optical micrographs of patterned poly(2-acrylamido-2-methyl-1-propanesulfonic acid) (PAMPS) composites with 0.065 vol% magnetically responsive rGO flakes of decreasing template area and various line widths. Reproduced from ref. 60 with permission from Springer Nature. Photographs of 0.1 wt% graphene suspension with (c) no magnet field and (d–f) magnets of different shapes and configurations placed underneath for magnetic field sensing and display. Reproduced from ref. 222 with permission from John Wiley and Sons. (g) Schematic of the experimental setup to generate a rotating magnetic field for planar alignment of graphene sheets. (h–j) Schematic representation and snapshots of white light birefringence/transmission images of graphene suspension under different magnetic field conditions: (h) without a magnetic field, (i) under a static magnetic field in the *x*–*y* direction, and (j) under a rotating magnetic field in the *x*–*y* plane. The symbol L represents the incident white light in the *x* direction. Reproduced from ref. 221 with permission from John Wiley and Sons.

changing the direction of the magnetic field, while the sample dimension is usually limited by the magnet size.

3.4.2 Electric field assisted orientation. Similar to magnetic fields, electric fields can serve as an external driving force to align anisotropic particles in programmable directions. Electric field induced alignment is compatible with dielectric materials or electrically conductive fillers, such as graphene nanoplatelets, graphite, BNNSs or fluorohectorite nanosheets, which are typically mixed in a low viscosity, organic medium.[229,230] These 2D nanomaterials can respond to the electric field and form oriented patterns because they can be polarized by the external field and acquire a dipole moment. During the electrical alignment, a high-frequency alternating current (AC) electric field is commonly used to orient 2D nanomaterials and also avoid the electrophoresis of nanosheets and the electrolysis of the medium.[231,232] Under this alternating AC electric field, any solid inclusion suspended in a dielectric liquid will be polarized and acquire a dipole moment because of the mismatch in dielectric properties and electrical conductivity between the particles and their surrounding matrix. For 2D nanomaterials with considerable anisotropy, the polarization moment generally develops along their basal plane. When the polarization moment is not aligned along the electric field, a torque is created that rotates the particles and align their basal plane along the electric field direction to reach an equilibrium state. Once aligned, the polarized nanosheets can attract each other due to opposite surface charges, leading to an end-to-end chain configuration (Fig. 16a–d).[233] Theoretically, similar to magnetic alignment, the electric field induced alignment method can achieve arbitrary orientation directions, simply by tuning the electric field. For example, complex and intricate ordered patterns can be fabricated by sequential electric field induced orientation and photolithographic consolidation (Fig. 16e–j).[232] Moreover, the electric field induced alignment of 2D nanomaterials should be differentiated from the electrophoretic deposition (EPD) for materials like rGO or MXenes, in which the charged particles cannot be polarized but will move towards the electrode of opposite polarity and deposit on the surface.[234–236]

3.4.3 Freeze casting. Freeze casting, also known as ice templating, is a well-established technique that is utilized to fabricate arbitrarily oriented patterns, such as horizontal, vertical, gradient, layered, honeycomb, and radial structures.[49,237–239] It is a versatile technique applicable to diverse

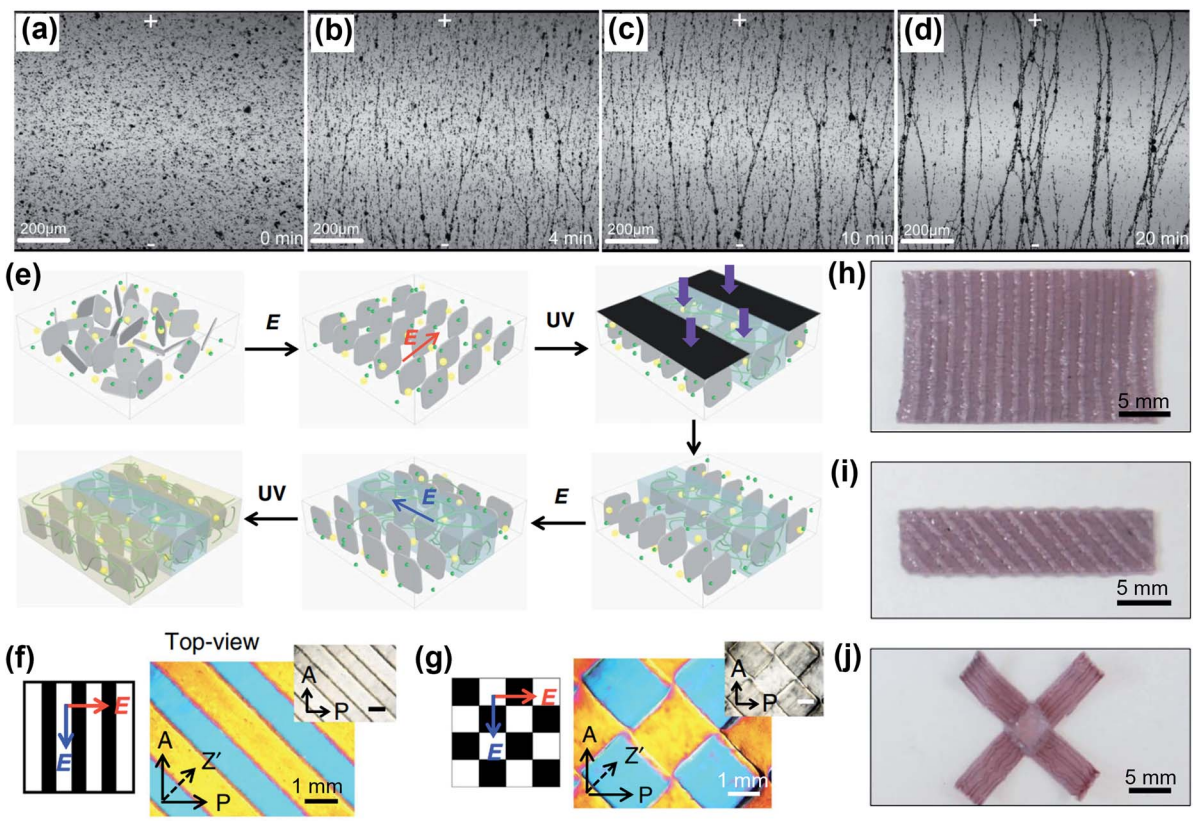

Fig. 16 Controlled orientation induced by an electric field. (a–d) Optical micrograph images of graphene nanoplatelet alignment in liquid epoxy resin by an AC electric field (*E*) as a function of time (0 to 20 min). (a) Random orientation of graphene nanoplatelets before applying an electric field, and after applying an electric field for (b) 4 min, (c) 10 min and (d) 20 min. Reproduced from ref. 233 with permission from Elsevier. (e) Schematic representation of a patterned anisotropic hydrogel by multi-step electrical orientation and photolithographic polymerization with different electric field (*E*) directions and use of ultraviolet (UV) light. (f and g) Polarizing optical microscope (POM) images showing hydrogel patterns with different nanosheet alignments. A: analyzer, P: polarizer, and Z′: axis of the tint plate. (h–j) Photos of the patterned anisotropic hydrogels. Reproduced from ref. 232 with permission from Springer Nature.

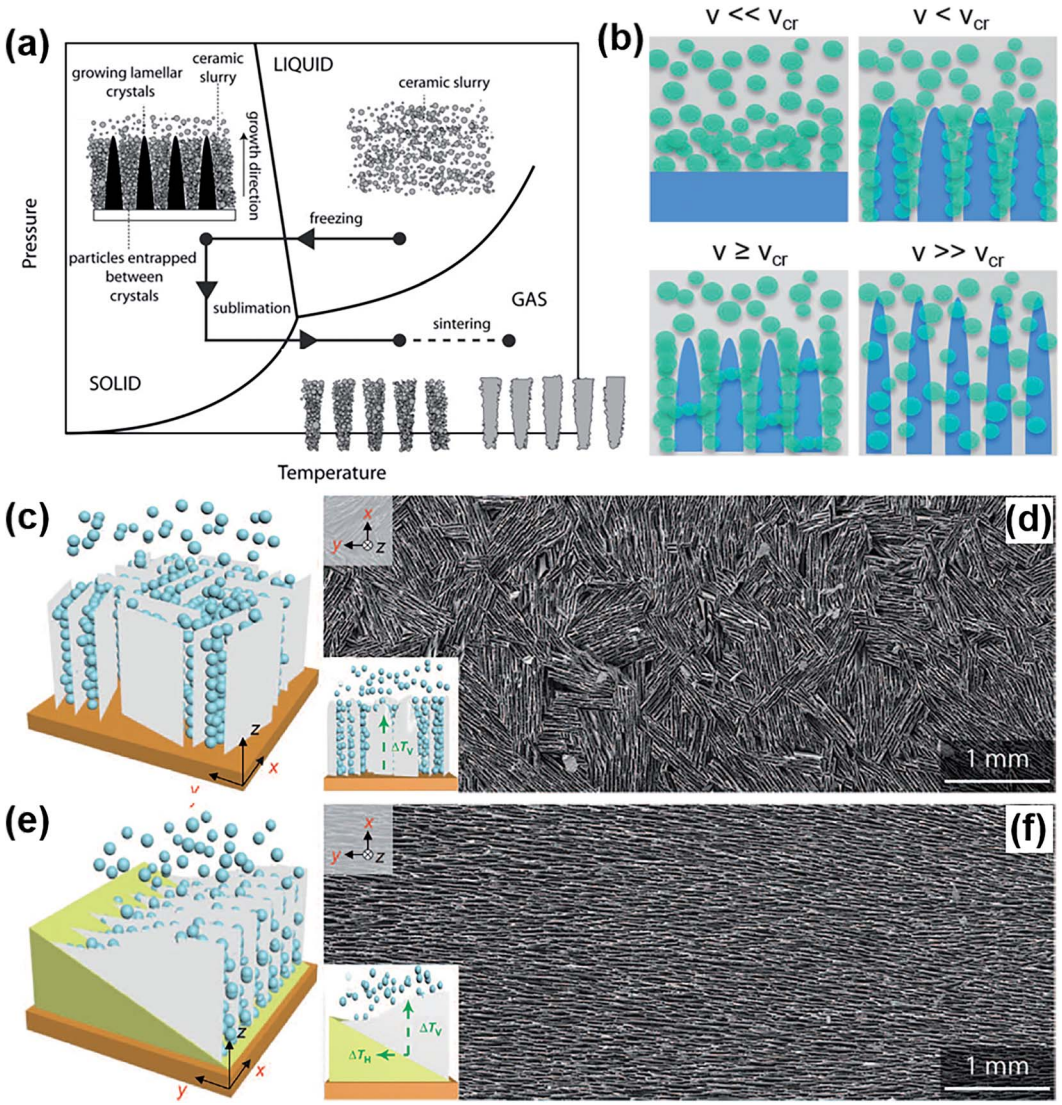

Fig. 17 Controlled oriented microstructures by freeze casting. (a) Schematic illustration of the four processing steps of the freeze casting technique including slurry preparation, solidification, sublimation and post-treatment. Reproduced from ref. 240 with permission from John Wiley and Sons. (b) Schematic representation of the freezing front progression at different velocities. Reproduced from ref. 49 with permission from John Wiley and Sons. The freezing front progression is decided by the particle freezing front velocity (v) and the ice critical freezing front velocity (v_{cr}). (c and d) Scheme and obtained hydroxyapatite (HA) scaffold of unidirectional freezing casting with a single vertical temperature gradient (ΔT_V). (e and f) Scheme of bidirectional freeze casting and the resulting HA scaffold with both the horizontal temperature gradient (ΔT_H) and vertical gradient (ΔT_V). Reproduced from ref. 242 with permission from the American Association for the Advancement of Science.

material types not limited to 2D nanosheets. The four processing steps of a typical freeze casting procedure are liquid suspension preparation, solidification, sublimation and post-treatment as shown in Fig. 17a.[240] A dispersant, plasticizer and binder are commonly added in the initial liquid suspension to ensure uniform dispersion of the 2D nanoparticles in the liquid medium. The microstructure is determined by the formation of ice dendrites during the solidification stage. After sublimation of the ice, the subsequent post-treatment, such as sintering densification, thermal reduction or pyrolysis, will transform the material into a porous scaffold. The desirable oriented patterns are thus set during the solidification, when the suspended particles are rejected by the moving solidification front, concentrated and entrapped between the ice crystals. Fig. 17b illustrates the freezing front progression at different velocities, where v is the particle freezing front velocity, and v_{cr} is the ice critical freezing front velocity. At a very low solidification velocity ($v \ll v_{cr}$), the particles are not rejected by the ice front, so that no pattern forms. At $v < v_{cr}$, the particles are generally rejected and assemble in a lamellar microstructure. And at $v \geq v_{cr}$, some particles could be further entrapped, leading to bridges between the lamellar structure. If the freezing rate is too high ($v \gg v_{cr}$), the particles are instead encapsulated within the ice front.[49] Moreover, different thermal gradients can be introduced to control the growth direction of the ice dendrites.[241] For example, Bai *et al.* compared the scaffolds prepared by unidirectional freeze casting and bidirectional freeze casting techniques using hydroxyapatite (HA).[242] For

unidirectional freeze casting, a single vertical temperature gradient was applied, leading to simultaneous crystal nucleation over the substrate (Fig. 17c). The obtained scaffold showed multiple domains with various orientations in the planar direction (Fig. 17d). For bidirectional freeze casting, a PDMS wedge was placed between the slurry and the cold substrate, leading the combination of both horizontal and vertical temperature gradients (Fig. 17e). The as-fabricated scaffold showed a well-aligned monodomain lamellar structure along the dual temperature gradients (Fig. 17f). Moreover, Shao *et al.* demonstrated the fabrication of 3D hierarchical porous graphene films by using freeze casting.[243] GO as a precursor was partially reduced to micro-gels and filtered before freeze casting. Ideally, continuous ice crystals are formed and the GO nanosheets are rejected from the solidification front to get a highly porous microstructure. The obtained 3D porous GO films exhibited a high electrical conductivity of 1905 S m^{-1} and good mechanical stability with only 9% decay of discharge capacitance after 500 bending cycles. Bian *et al.* reported a direct freeze casting route for the fabrication of ultralight Ti_3C_2–MXene aerogels with density lower than 10 mg cm^{-3}.[244] The MXene aerogels showed a specific shielding effectiveness of 9904 dB cm^3 g^{-1} with a reflection lower than 1 dB, which can be useful for EMI shielding applications. Additionally, more freeze casting control strategies such as radial freeze casting or external field assisted freeze casting have been implemented, providing controllable assembly methods for 2D material applications.[36,245,246]

3.4.4 Chemical vapor deposition (CVD). Chemical Vapor Deposition (CVD) is a widely used technique that involves a gaseous material reaction and subsequent solid deposition on a substrate. As a versatile bottom-up growth method to synthesize oriented 2D nanomaterials, the obtained material morphology and alignment can be tuned by controlling the growth parameters such as selective source materials, temperature, pressure, gas flow rate and so on.[247] The CVD fabrication method is classified as an arbitrary alignment technique here because 2D nanomaterials can be formed into several types of alignment, typically including horizontal, vertical and heterogeneous alignment structures.[55,248–253] The alignment of the grown 2D nanomaterials such as TMDCs can be tuned using different CVD growth conditions. Dumcenco *et al.* reported the morphological changes of MoS_2 by tuning the sample temperature.[254] When the gas injection temperature gradually decreased from 700 °C to 600 °C, the MoS_2 domains went through the vertically aligned multilayers to a reduced longitudinal length, and finally changed into horizontally aligned monolayers. Cho and co-workers fabricated MoS_2 films with different alignment directions by rapid sulfurization of CVD (Fig. 18a–d).[55] The growth direction of the TMDC films could be

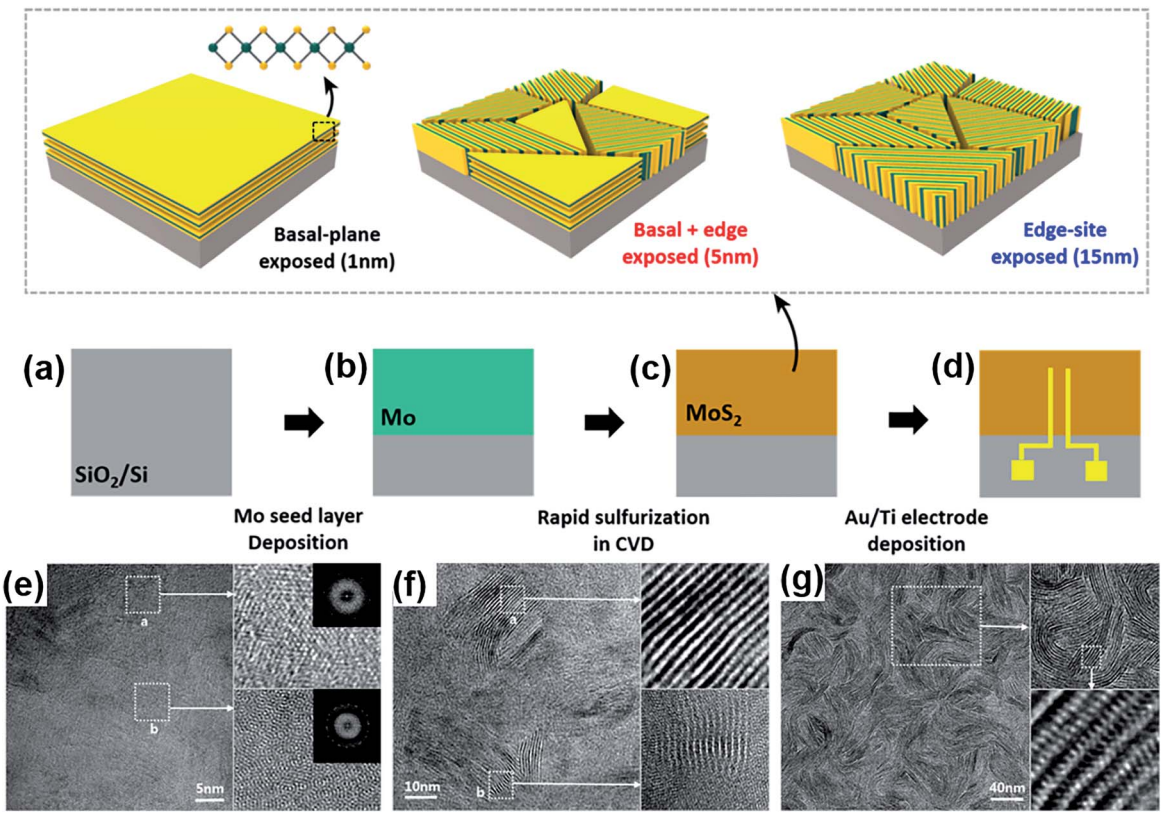

Fig. 18 Controlled orientation of 2D MoS_2 films by CVD growth. (a and b) Mo seed layers are predeposited on a substrate. (c) Growth of MoS_2 films from horizontal to vertical alignment upon increasing the Mo seed layer thickness. (d) Deposition of an Au/Ti electrode for application. (e) Horizontal layer alignment from 1 nm seed thickness. (f) Horizontal and vertical heterogeneous alignment from 5 nm seed thickness. (g) Vertical film alignment grown from 15 nm seed layer thickness. Reprinted with permission from ref. 55. Copyright (2015) American Chemical Society.

controlled by the thickness of the pre-deposited metal seed layer.[55,248,251] Horizontal (Fig. 18e), a mixture of horizontal and vertical (Fig. 18f), and vertical alignment (Fig. 18g) were achieved with increasing seed layer thickness. Later, Kumar *et al.* investigated the horizontal to vertical growth of MoS_2 films by tailoring the supersaturation ratio of the S:MoO_3 precursors.[249] These various aligned structures obtained from direct growth by CVD indicate the possibility to better control the 2D nanomaterials. At the same time, CVD is a scalable method to fabricate diverse nanomaterials with high quality, which requires precise control over the grow parameters.

In summary, the alignment of 2D nanomaterials can be well controlled through various processing methods involving self-driven or directed assembly. Based on the desired material and target orientation patterns required for specific properties and applications, people can select appropriate fabrication techniques. Furthermore, the selection of the most adequate fabrication process to achieve a target microstructure should also consider (i) the available material quantity and form. For example, all processes except CVD and hydrothermal and gelation require a well-disperse, stable dispersion of 2D nanosheets in a medium; (ii) the intended final relative density. For example, porous structures can easily be formed using freeze-casting, salt templating, or gel casting, whereas hot pressing or vacuum filtration, among others, lead to dense films; (iii) the intended properties and chemistry of 2D nanomaterials. Indeed, the processes requiring chemical reactions or intrinsic properties like anisotropic electric responses are chemically dependent, whereas others are mostly based on the physical properties of the nanosheets such as their dimensions, like magnetic fields, freeze-casting, filtration, *etc.* Furthermore, the methods reviewed here are representative of the most commonly used methods and have numerous variations in the literature. Although some can produce bulk samples, couple several materials or have heterogeneous alignment patterns, one common limitation of these methods is their inability so far, to decouple the final material shape with the local microstructure. This limits the potential for design and the fabrication of complex structures with tailored, local orientations. Also, in view of creating a multifunctional device containing particles of various chemistries, it is necessary to use a fabrication method that would be efficient independently of the material type. The freedom of shape, orientation, and composition is one of the many advantages that could be brought about by 3D printing. One recent and extremely exciting process with industrial potential is 3D printing. In the following section, how 3D printing can support the microstructure control using 2D nanomaterials is reviewed. The ability to create 3D shapes with locally controlled orientation of 2D nanomaterials in dense or porous packings would allow more design flexibility, giving a bright future for energy devices and others with boosted performances.

4. 2D nanomaterial alignment supported by 3D printing

Substantial efforts have been made to develop various processing techniques to achieve controlled orientations of 2D materials. To implement these achievements into a functional device with enhanced performance, a realistic 3D object or prototype is highly demanded. However, it is challenging to translate the exceptional properties of 2D materials into end structures for specific applications, because it involves assembling and upscaling the oriented microstructure for target properties. For example, it may be necessary to add a layer of glue between components processed separately, preventing intimate bonding between the functional parts and decrease in properties. In this area, 3D printing is a potential solution under the spotlight and a few reviews discuss about the 3D printing of 2D nanomaterials.[256,257] However, these reviews miss the importance of 2D nanomaterial alignment and how the combination of 3D printing with alignment could further induce new and enhanced functionalities. In the following section, we therefore review 2D nanomaterial alignment supported by 3D printing and discuss how 3D printing can be expected to fabricate realistic devices with high performance and/or new functionalities.

4.1 Advances in 3D printing

3D printing, or interchangeably called additive manufacturing (AM), refers to the fabrication process of building a 3D structure in a layer-by-layer manner. This fabrication strategy allows customizable computer-aided design (CAD) and precise control of complex patterns from printable inks, for example, containing 2D nanosheets distributed in a matrix. One remarkable advantage of 3D printing over most conventional fabrication processes is the large design freedom. Indeed, the starting materials, 3D printing equipment, final structures, complexity, dimensions, and postprocessing methods can be tailored as desired. As a result, development in the field grows rapidly and has attracted increasing attention from both scientific and industrial communities in the latest decade. 3D printing also allows the fabrication of complex, hierarchical structures with as much diversity as found in biological materials such as those shown in Fig. 1. 2D nanomaterials can therefore be integrated into nano-, micro-, and macroscopic structures, as illustrated in Fig. 19. If some of the common processes have numerous advantages for specific applications, for example for producing homogeneous coatings, fast production of thin films, nearly defect-free 2D nanomaterials, *etc.*, 3D printing technologies open the avenue for the design and fabrication of materials, using one single method, but for potentially any application. More specifically, when it comes to 2D nanomaterial assembly, 3D printing technology reveals unique advantages over the standard processes in the following aspects: (i) local microstructures: the embedded particles can be locally reoriented during the printing process or post-processing, with or without the assistance of external forces such as magnetic, electrical, or acoustic fields. (ii) Multimaterial structures: heterogeneous material compositions can be combined and fabricated synchronously during printing. (iii) Complex shapes: benefiting from the layer-by-layer printing manner, complexity and diversity of the shapes can be broadened, especially for those with hollow structures and intricate interconnections. (iv) Scale up:

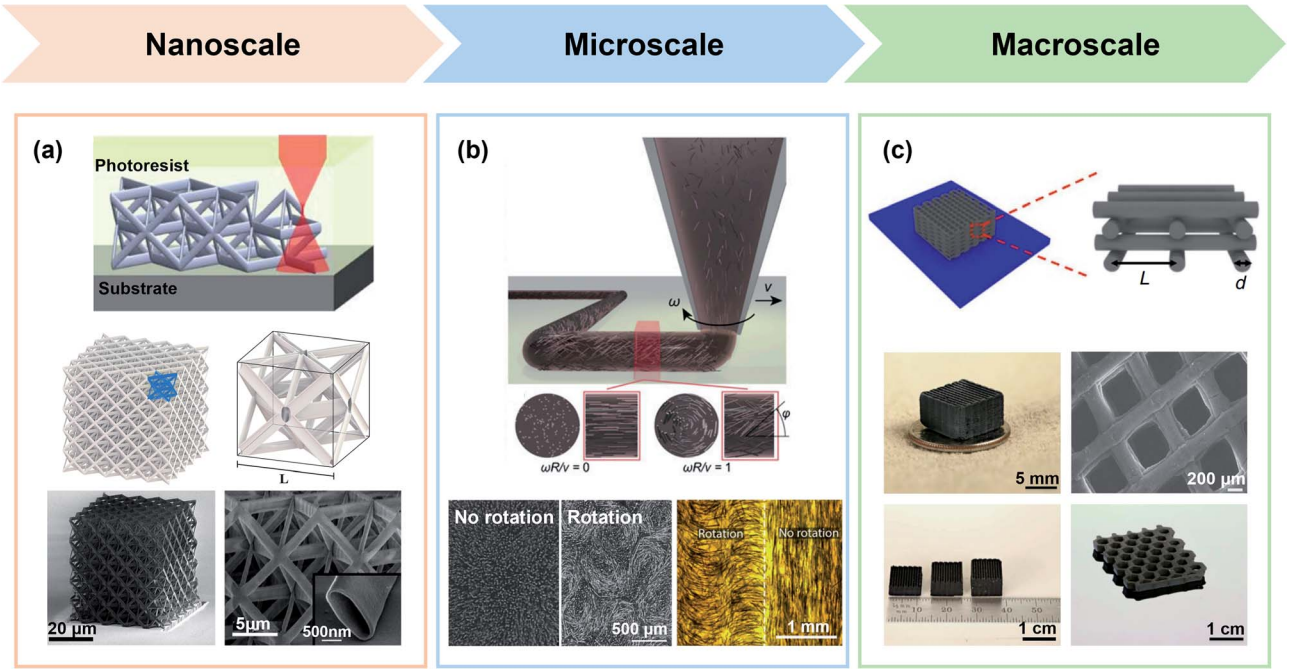

Fig. 19 Integration of materials into nanoscale, microscale and macroscale structures by 3D printing. (a) Fabrication of nano-sized hollow-tube alumina ceramic nanolattices using two-photon lithography. Reproduced from ref. 258 with permission from the American Association for the Advancement of Science. (b) Carbon fiber orientation during printing through rotational direct ink writing with fiber alignment controllable on a micro-scale. Reproduced from ref. 259 with permission from the National Academy of Science. The helical pattern is dictated by the rotational rate (ω), translational velocity (v), surface fiber orientation (φ) and dimensionless rotation rate ($\omega R/v$). (c) 3D printed graphene aerogel microlattices with various structures and dimensions up to the centimeter scale. Reproduced from ref. 260 with permission from Springer Nature.

the dimensions and defined geometries of the printed architectures can be easily customized, enabling the fabrication of scalable products. The 3D printing methods used for 2D nanomaterials are presented in the following section.

4.2 3D printing combined with alignment

First described in the 1980s by Charles Hull regarding the stereolithography (SLA) process, 3D printing technology has evolved into multiple printing forms such as inkjet printing, direct ink writing, powder bed fusion, selective laser sintering and so on.[261–268] Overall, 3D printing techniques can mainly be classified into three types based on the material feedstock: slurry-based, powder-based and bulk solid-based. Each printing method possesses its own technical features in terms of the equipment setup, feedstock material requirement, and printing advantages and limitations. The recent progress in 3D printing has been summarized in a few comprehensive reviews.[262–264,268–271] A few studies report the use of fused deposition modelling (FDM) using graphene but the fabrication of thermoplastic filaments with homogeneously distributed 2D nanosheets is challenging.[272,273] In FDM, a thermoplastic filament is heated and extruded through a nozzle on a substrate, where it cools down to solidify. Inkjet printing has also been applied to 2D nanomaterial liquid suspensions but yields horizontal alignment.[274] Obtaining vertically oriented nanosheets is difficult due to the capillary forces that develop during solvent evaporation in the deposited droplets. One recent paper reported on the drop-on-demand of purposely oriented 2D nanomaterials by adding a magnetic field. The success of the method depended on the concentration of particles in the ink deposited.[275] Moreover, SLA has also been used with 2D nanomaterials.[276,277] In SLA, a liquid suspension containing 2D nanosheets and a UV-curable liquid is locally cured using UV light. Using local, sequential curing, SLA has been successfully applied in conjunction with magnetic fields to locally orient 2D nanosheets.[278] Also, in SLA, graphene could be horizontally oriented simply by gravitational force during printing.[279]

Furthermore, the orientation of 2D nanomaterials has been achieved by combining 3D printing techniques with an external magnetic field, electric field and temperature gradient, to introduce particle alignment in a programmable fashion.[226,280] Martin *et al.* utilized the 3D magnetic printing method to fabricate complex oriented architectures using anisotropic 2D particles.[281] The particles were oriented and patterned during printing using magnetic fields, where a digital light processor was used to cure the resin (Fig. 20a1–a3). Furthermore, applying a temperature gradient by freeze casting is also a feasible way to create desirable alignment in 3D printing.[49] Zhang *et al.* developed the freeze casting assisted 3D printing of graphene aerogels from a drop-on-demand inkjet printer (Fig. 20b1–b4).[282] Freeze casting provides rapid freezing and can manipulate the dispersed graphene orientation along the freezing direction. Thanks to the anisotropic ice crystal growth, the low viscous Newtonian graphene suspension can be printed into highly ordered assemblies as the graphene nanosheets are squeezed between the ice crystals. The printed graphene aerogel obtained

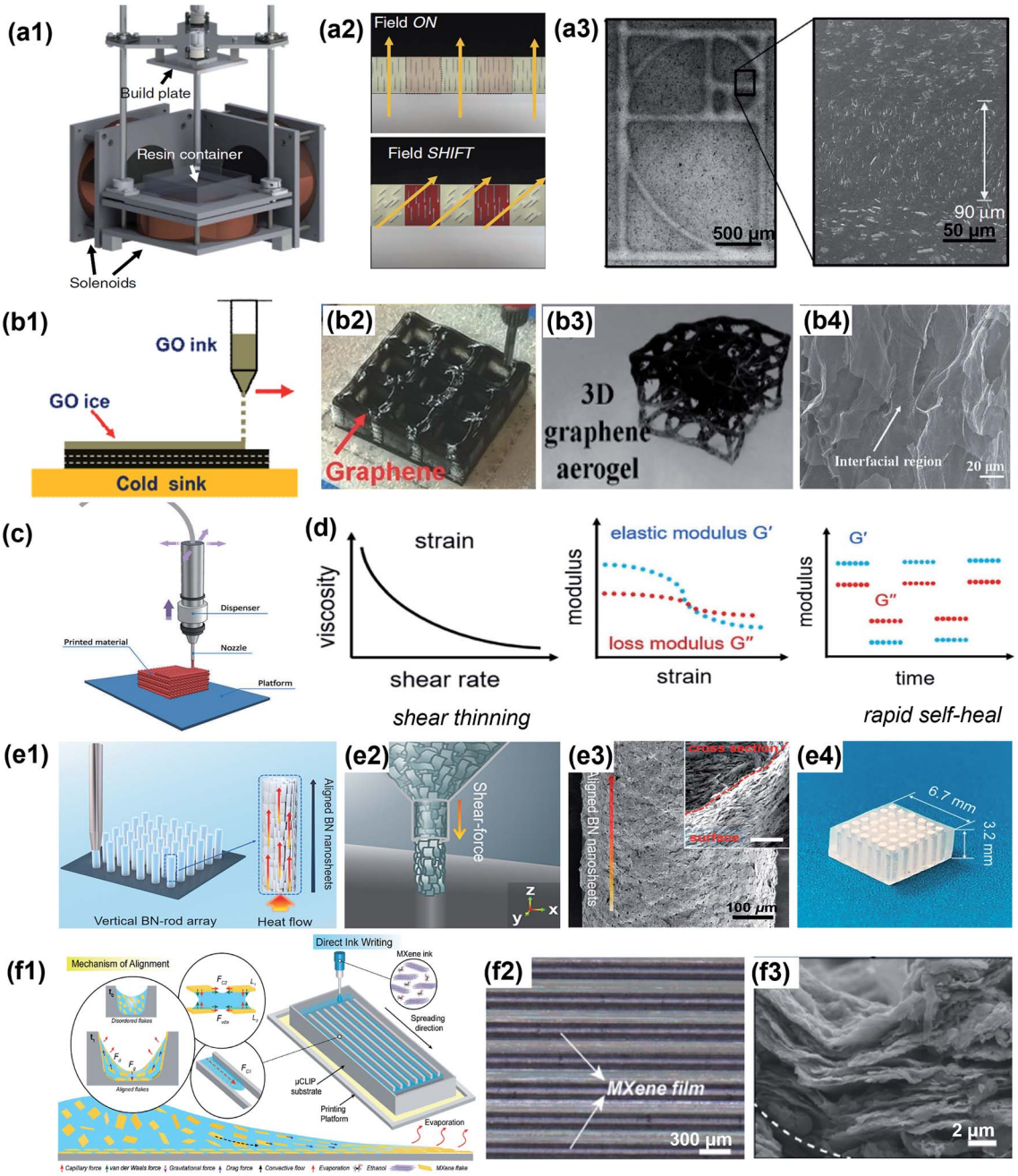

Fig. 20 Representative 3D printing techniques combined with 2D material alignment. (a1) Schematic representation of the 3D magnetic-printer setup. (a2) The 3D magnetic printing process with programmable magnetic field shift and selective polymerization. (a3) The printed micro-architectures showing complex particle orientation. Reproduced from ref. 281 with permission from Springer Nature. (b1) Schematic of freeze casting assisted 3D printing of graphene aerogel. (b2) 3D printing of graphene suspension. (b3) Thermally reduced 3D ultralight graphene aerogel. (b4) Cross-sectional SEM image showing the interfacial region along the deposition direction. Reproduced from ref. 282 with permission from John Wiley and Sons. (c) Schematic diagram of direct ink writing (DIW). Reproduced from ref. 298 with permission from the Royal Society of Chemistry. (d) Favored rheological properties of a typical DIW ink with shear thinning and rapid self-healing properties. Reproduced from ref. 287 with permission from John Wiley and Sons. (e1) Schematic illustration of the 3D vertical printing of a BN array through the DIW method. (e2) Schematic illustration of BNNS alignment by shear force from the fine nozzle during extrusion. (e3) Morphology of the printed BN rod showing vertically aligned BNNSs. (e4) Scalable BN array encapsulated into a PDMS matrix. Reprinted with permission from ref. 294. Copyright (2019) American Chemical Society. (f1) Schematic of the $Ti_3C_2T_x$ MXene alignment by capillarity-driven DIW *via* microcontinuous liquid interface production (μCLIP). (f2) Representative top view of deposited MXene films on patterned substrates. (f3) Printed MXene films showing the alignment. Reprinted with permission from ref. 295. Copyright (2021) American Chemical Society.

presented ultralight densities with high compressibility, demonstrating excellent mechanical robustness. At the same time, the graphene macroscopic material with an aligned microstructure offers high electrical conductivity and potential anisotropic thermal insulation properties for future applications.

The direct ink writing (DIW) 3D printing method is preferred for 2D nanomaterials given its ability to print from homogeneously dispersed liquid suspensions. In the following paragraphs, we discuss the DIW method applied to slurries containing 2D nanomaterials, showing multiple orientation control. DIW is an extrusion-based 3D printing technique. In this process, 2D nanosheets are first homogeneously dispersed in a liquid polymer or solvent to produce an ink. As shown in Fig. 20c, the as-prepared ink is extruded from a printing nozzle as a continuous filament, and deposited in a layer-by-layer manner following a predefined pattern, just as directly "writing".[268,283,284] Then, the printed filaments are consolidated by curing under heat or light, other chemical reactions, dried or frozen, depending on the matrix composition used in the ink. As the quality of final printed parts is entirely determined by the rheological properties of the ink, a wide range of 2D nanomaterials can be obtained. Pastes, solutions, and hydrogels have been shown to be printable using DIW.[267,285,286] Obtaining appropriate rheological properties for the ink is paramount for successful printing, which is closely related to the filler concentration. To secure this printability, the ink has to exhibit the following key properties (Fig. 20d): shear thinning and viscoelasticity. Indeed, extrusion requires reasonably low viscosity of the ink. Thus, a viscosity decreasing with the applied shear rate is necessary. A viscosity ranging from 0.1 to 10^3 Pa s^{-1} is recommended to get smooth printing.[269,283,287] In addition, the ink should have viscoelasticity to guarantee shape-retention and stability of the printed part. The elastic (or storage) modulus (G') should be lower than the loss modulus (G'') under shear, but should rapidly recover to the opposite ($G' > G''$) once the shear force is removed.[288] The behavior of such a viscous ink flow is usually described by the Herschel–Bulkley model:[289]

$$\tau = \tau_y + K\dot{\gamma}^n \quad (6)$$

where τ is the shear stress, τ_y is the yield stress, K is the viscosity parameter, $\dot{\gamma}$ is the shear rate, and n is the shear shinning exponent ($n < 1$). In this model, the yield stress is the minimum shear stress above which the ink flows. In the case of a shear stress lower than the yield stress, the fluid behaves like a solid material.[290–292]

Having described the DIW printing method, we report how DIW has been used for 2D nanomaterial alignment. The 2D nanosheets dispersed in the ink can be manipulated by external forces or driven by self-assembly when the ink is still liquid, in the barrel, during extrusion, or in the printed parts and before consolidation by post-processing. The ability to locally control the orientation can in turn tune the local properties within the whole 3D part. For example, for 2D nanomaterials with a considerable aspect ratio, the alignment can be induced by shear force along the printing direction.[293,294] Liang *et al.* proposed a general method to fabricate vertically aligned 2D materials on a multiscale by DIW.[294] As shown in Fig. 20e1 and e2, the orientation of 2D BNNSs could be induced by the high shear force generated during the extrusion of the ink. As a result, the 2D BNNSs were assembled along the vertical direction, which demonstrated outstanding thermal conductivity in the out-of-plane direction (Fig. 20e3). This shear force assisted printing strategy has been expanded to other 2D nanomaterials such as graphene and MoS_2 and can also be upscaled into macroscopic arrays (Fig. 20e4). In addition, Jambhulkar *et al.* demonstrated the orientation of 2D MXene nanoparticles by capillarity-driven DIW.[295] In this case, a patterned substrate with microchannels was fabricated before printing, into which a MXene/ethanol suspension was spread (Fig. 20f1). The high capillary forces generated at the entry of the microchannels overcome the gravity, leading to the flow of MXenes in the microchannels. The Reynolds number, R_e, is an index used to describe fluid flow and is key in this process.

$$R_e = \frac{\rho v L}{\mu} \quad (7)$$

where ρ is the fluid density, v is the fluid velocity, L is the characteristic linear length, and μ is the viscosity of the fluid. A low R_e ($R_e \ll 1$) indicates a laminar flow within the microchannels and is suggested to be the main driving force to MXene nanosheet alignment retained after the subsequent evaporation of the solvent (Fig. 20f2 and f3).[295–297]

In summary, DIW is a highly tunable method that further expands the already large freedom degree of 3D printing by providing alignment control. This permits concomitant design of the shape and of the properties. Indeed, by providing a 3D shape with intricate microstructural features and design capabilities, these methods will enable us to make one step forward towards functional devices using 2D nanomaterials. One limitation however is the concentration of 2D nanosheets in the final material that is limited by the rheological properties. Indeed, it is known that increasing the concentration of nanoparticles leads to jamming of suspensions. In the case of anisotropic nanosheets of a high aspect ratio, this concentration is further decreased. Other points of improvement in DIW are interfilament binding that might compromise the performances of the 3D part, and nanosheet deformation which might reduce their intrinsic properties. Nevertheless, performing 3D objects can now be obtained and tested for real applications.

4.3 Beyond alignment control

The capability of harnessing local structures using 3D printing has potential for developing advanced materials and multifunctional devices. Indeed, we have seen in Section 2 of this review how orienting 2D materials into specific directions could enhance the performance of various functional devices. But the potential of 3D printing goes beyond its capability to create 3D shapes and controlling the local particle orientation. In view of creating multifunctional devices, another benefit of 3D printing is that inks of various chemical compositions can be printed in the same part. This is referred to as multimaterial 3D printing. This could for example lead to the fabrication of devices where the sensor is integrated in a device along with a battery or a supercapacitor, so as to release energy upon a specific external stimulus. It could also be used simply to create compact devices while maintaining low weight, to reduce the volume and

payload for automobile or aerospace applications. In addition to this, 3D printed parts with a local orientation and composition can induce new properties in the object, which result from the microstructural control and not entirely from the intrinsic properties of the filler. The most obvious of these new properties is self-shaping. 3D printing with time-varying morphing or performance variations is referred to as 4D printing. With the local orientational and compositional control, it is therefore possible to talk about 6D printing.[299] These aspects are reviewed and discussed in the following sections for the specific case of 2D nanomaterials.

4.3.1 Multimaterial fabrication. Recent advances in 3D printing have revealed the possibility of multimaterial fabrication. Thanks to this unique capability, 3D printing is no longer limited to shaping and offers a broader imagination space for design and multifunctionality. Multimateriality in devices is thought as a means to increase sustainability thanks to the reduction of processing steps, waste material, and increase in functionalities within a small volume.[284] For example, Kokkinis *et al.* established multimaterial magnetically assisted DIW with alumina platelet orientation.[300] The DIW printer was equipped with individual syringes and a two-component dispenser to extrude different compositions during printing combined with local control over the building blocks (Fig. 21a). The inks, containing magnetized alumina platelets with fumed silica in resin (Fig. 21b and c), were designed to have printable rheological behaviors. The subsequent control of particle alignment was achieved by applying an external rotating magnetic field before consolidation (Fig. 21d). As a result, the printed macrostructure could be programmed with heterogeneous microstructures through locally tailored particle orientation and multimaterial compositions, as shown in Fig. 21e–g. Moreover, Skylar-Scott *et al.* achieved soft matter assembly by multimaterial multinozzle DIW.[301] The ideal DIW system for multimaterial 3D printing possesses multiple printheads that extrude filaments of various compositions at a sufficiently high switching frequency between the compositions. The multimaterial nozzle can print different compositions within a single continuous filament, a pattern of filaments, or different parts in a macrostructure, which further broadens the design and manufacturing of complex motifs. Hardin *et al.* also demonstrated multimaterial 3D printing by developing a multimaterial microfluidic printhead for DIW.[302] The microfluidic printhead design enabled printing multiple materials from the same

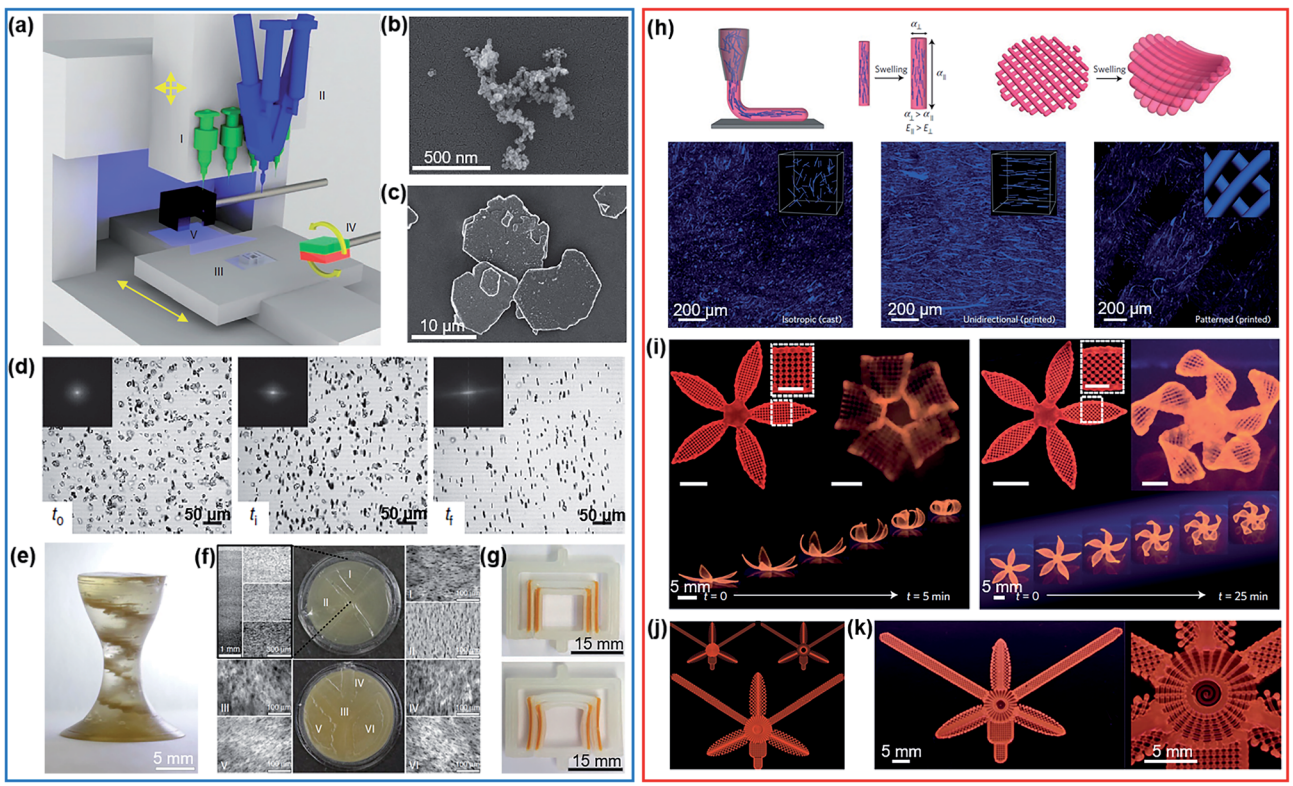

Fig. 21 Possibility beyond 3D printing with multimaterial fabrication and shape morphing. (a) Schematic of the direct ink writing setup for multimaterial magnetically assisted 3D printing. (b) SEM image of fumed silica particles as a rheology modifier. (c) SEM image of alumina platelets as a functional component. (d) Alignment dynamics of alumina platelets under a rotating magnetic field. (e) Printed macroscopic structure with an internal helicoidal staircase. (f) Morphology of the bottom layer showing effective printing of domains with different local platelet orientations. (g) Printed key-lock structure before and after swelling shape change. Reproduced from ref. 300 with permission from Springer Nature. (h) Schematic of 4D direct ink writing for shear-induced alignment of cellulose fibrils with isotropic, unidirectional, and patterned microstructures. (i) Printed flower morphology changes during the swelling process generated with 90°/0° and 45°/45° bilayer orientation. (j) Print path and (k) printed swollen structure. Reproduced from ref. 314 with permission from Springer Nature.

nozzle in a seamlessly switching manner. This programmable multimaterial fabrication method demonstrates the chances for building architectures with encoded local compositions for multifunctional applications. Some issues still remain, such as local mixing between the different compositions, which can lead to desired or undesired compositional gradients. Also, interfacial bonding between the different inks is important to be maintained throughout the processing stages to prevent the delamination of the macrostructure at a later stage. More recently, the concept of introducing complex gradient design is implemented in multimaterial 3D printing to reduce the interface mismatches in heterogeneous materials. With a gradient structure, the local mechanical properties of printed products can be altered to prevent the premature failure of devices, for example, to relieve the stress concentration.[321] The point of interfacial bonding is rather challenging when anisotropic, local orientations are added to it because of the anisotropic shrinkage that occurs due to temperature or curing, or other discrepancies between each material within the multimaterial composition. These challenges could be mitigated by using inks suspending 2D nanoparticles of various chemistries within the same matrix, and by consolidated the parts *via* methods that do not use temperature, curing, or drying. In addition, the gradient 3D printing provides the capability of better manipulating local material compositions from functionally graded materials (FGMs) where the material properties can vary spatially in 3D space, shedding light on wider design space and optimized functions in 3D printing.[322]

4.3.2 4D printing. The concept of 4D printing was initially established by Tibbits in 2013.[303] 4D printing allows the time-dependent evolution of the 3D printed shape or properties by intentionally encoding this time dependence into the part through the 3D printing process.[269,270,304–307] Generally, the time-dependent change is triggered by an internal or external stimulus, such as temperature, magnetic field, electric field, particle orientation and pressure.[228,308–313] For example, one typical strategy to encode shape change in a 3D printed object is by orienting nanofillers in perpendicular directions in a bilayer and using a matrix that changes its volume in response to an external stimulus. One illustration of such a shape change has been realized by 3D printing anisotropic cellulose fibrils in a soft acrylamide matrix.[314] During printing, the cellulose fibrils within the hydrogel composite align due to the shear force (Fig. 21h). Therefore, the printed object had anisotropic elastic and swelling properties tailored thanks to the local control of the filler orientation, which leads to its morphing under hydration (Fig. 21i–k).

In summary, the rapid development of 3D printing technologies has the potential to further unlock the advantages of 2D nanomaterials from the nanoscale to the microscale and up to the macroscale. 3D printing can be efficiently combined with deliberate local 2D nanosheet orientations, multimaterial compositions and time-dependent properties. The capability of controlling local compositions and microstructural alignment in 3D parts of defined shapes could therefore allow the development of new advanced, smart and multifunctional devices. The following section discusses what could be the anticipated exciting prospects and what challenges still need to be faced to this aim.

5. Anticipated prospects and remaining challenges

The aforementioned processing techniques demonstrate the potential of harnessing 2D nanomaterial alignment into desirable assembly patterns, where the local orientation can be horizontal, vertical, heterogeneous, or purposely set in any orientation. Furthermore, 3D printing technologies enable upscaling with the possibility of using multiple local compositions or microstructural orientations. We have seen in Section 2 of this review that oriented 2D nanomaterials significantly boost the performance of sensing, thermoelectric and electrochemical devices. Given all these advances in manufacturing and local orientation and composition, we have to pose the question of how can these advances be leveraged for realistic, smart, multifunctional applications? What remains to be investigated or what could be the difficulties to overcome? These open questions are discussed in the following.

5.1 Anticipated prospects

3D printing of 2D nanomaterials already can create 3D shapes with local design, composition and time-dependent properties. 3D printing can even be further augmented with tunable density by controlling the porosity within the printed filaments in DIW, by adding a sacrificial porogen or a foaming agent, for example. Intentionally introducing nano- or micro-porosity could increase the surface area, contribute to efficient molecule transportation and diffusion, to further augment the functional properties. Therefore, appropriate addition of porosity could lead to objects with a lighter weight but similar, if not increased, performance. This would result in the use of less material feedstock and in turn allow less waste material generation. Another advantage of controlled local porosity, orientation, and composition is the ability to design entirely hierarchical structures from the nanoscopic scale to the macroscopic scale, in a fashion that can be paralleled with the natural materials discussed in Fig. 1 in the Introduction of this review. Hierarchical designs are indeed known to enhance simultaneously the functional and structural properties of natural materials by inducing microstructure-related mechanisms. One common example of hierarchical design is the helicoidal arrangement of nanoparticles in the so-called Bouligand structure in the Mantis shrimp, that provides strength and toughness, while nanochannels spread throughout the material allowing ion flow.[315] One could imagine such a similar structure where the nanoparticles in the natural structure are replaced with vertically oriented 2D nanosheets. In this case it could be that the resulting materials could exhibit lower tortuosity, leading to the functionalities reported in Section 2 of this review, in combination to high mechanical performance. The dual presence of enhanced functional and structural properties is important in all devices. Indeed, in operation, devices also need to withstand loads, shocks, vibrations, stresses, *etc.*

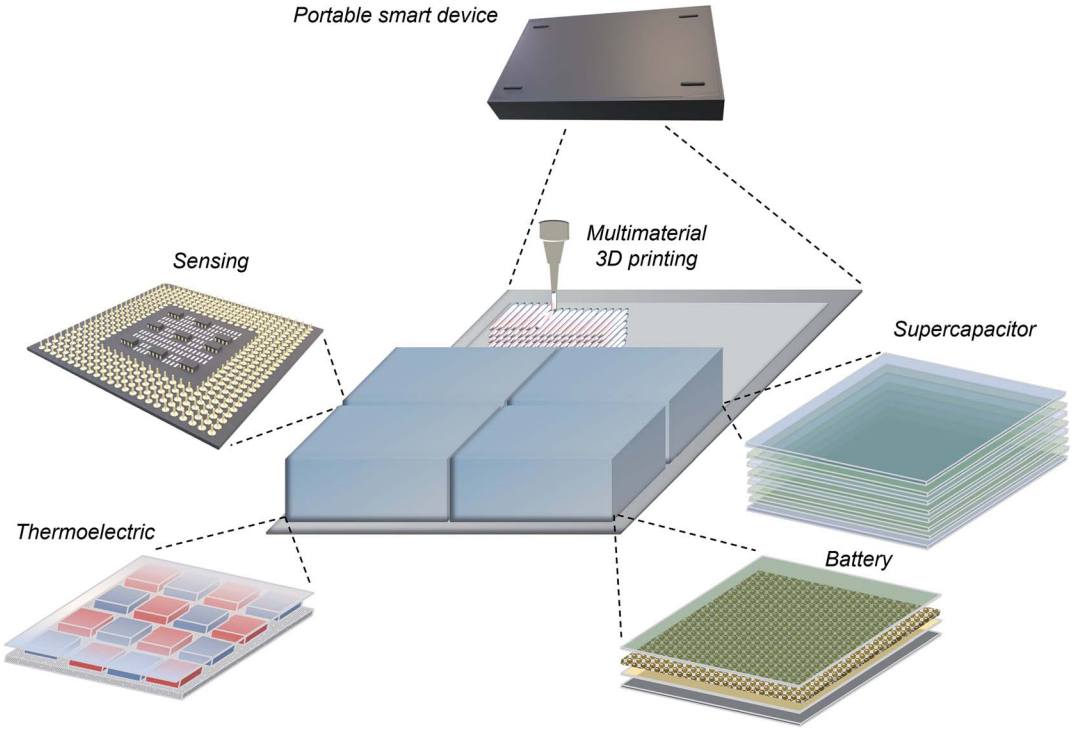

Fig. 22 Schematic illustration of smart functional device design with customizable multifunctionality.

Furthermore, local microstructural design capability also opens up new applications. One could imagine conformable batteries or supercapacitors with complex intricate shapes that integrate inside or around the apparatus to which they supply energy. To maintain the performance in curved designs, for example, the microstructure should be adapted accordingly. One could be interested in this capability when designing compact devices of a high surface to volume ratio and low weight. These kinds of demands are interesting in autonomous vehicles, portable biomedical devices and other robotic applications, for example. Finally, the multimaterial capability of 3D printing would permit the design of multiple devices integrated within one 3D object. Fig. 22 illustrates the design of a multifunctional smart device. Within one 3D device, multiple functionalities can be fused and cooperate automatically, for example, sensing an external heat stimulus, and then generating electrical energy from the waste heat through a thermoelectric module, and later harvesting the electrical energy by using a battery or a supercapacitor. To add more customizable functions, the individual devices could be simply printed next to each other using one unique process, thereby reducing time, manpower, and space for their fabrication. The devices could also be integrated more intimately at a smaller scale, nano or micro, so that their functions are related to each other. Other concrete examples of this concept might be a battery that changes shape depending on an external stimulus and that in turn changes its battery performance, or a supercapacitor with an integrated sensor able to inform on the status of the capacitor or to change its performance depending on external parameters. Materials with embodied and interacting functions are referred to as 'robotic materials' and could unlock numerous opportunities for passive actuation of functional device and material computation.[316]

The blooming studies on the synthesis and assembly processing of 2D nanomaterials in the past few decades have triggered explosive progress in this research community and brought about great opportunities in diverse application fields. Introducing alignment and designed microstructural patterns with 2D nanomaterials has shown unpredictable capabilities to further amplify the functionalities. Established, state-of-the-art advances demonstrate indeed the great potential of orientated 2D materials in future functional designs and applications. Although these developments lead to exciting, anticipated ideas, a number of challenges remain. Some of these challenges are now discussed.

5.2 Remaining challenges

The first challenge to realize the anticipated prospects is the obtention of a scalable material feedstock of high quality. In terms of 2D nanomaterial synthesis, the current nanomaterials produced through top-down exfoliation and bottom-to-up growth still have a yield far from what is needed for industrial application or commercialization. Furthermore, the quality of the produced 2D nanomaterials is greatly affected by the fabrication methods. For example, mechanical processes may lead to wrinkling of the nanosheets, reducing their properties in the plane. At the same time, chemical processes use harsh chemicals and solvents that are not sustainable or safe, for which waste management and cost are demanding. The synthesis of 2D nanomaterials also determines their

dimensions, anisotropy, surface functionalization capability, *etc.* The 2D nanomaterial quality, composition, size, *etc.*, greatly affect their nanoscopic intrinsic properties. Hence, managing high material quality and quantity are essential for good performances. To achieve high yield and quality, and limit the use of solvents and waste chemicals, biosynthesis and green synthesis should be further explored. Promising results have been obtained for the biosynthesis of graphene using biomolecules,[317] and green synthesis of graphene *via* electrochemical processes,[318] and should be transposed for other 2D nanomaterials.

Furthermore, to achieve ideal tunability and high performance of devices based on 2D nanomaterials oriented in multiple directions, it is necessary to unravel the related microstructure–property relationships. The complex relationships between the intrinsic material properties, defects, assembled structure, orientation degree, and connectivity are indeed intrinsically related to the final performances. For example, giving a specific application, suitable material selection, high material quality and a controlled defect level can bring about higher chances for desirable material performances. Moreover, the assembly strategy plays a critical role in further deciding how the final performances are yielded. With better understanding of the internal interactions, 2D nanomaterials could then be rationally modified and arranged into favorable structures using the advanced processing methods or printing technologies described in this review. Computation modelling and simulations, for example using density-functional theory (DFT) modelling, Monte-Carlo simulations and other computation methods should be further used to explore and understand the mechanisms at the nanoscopic and microscopic scales and enable hierarchical design.

Finally, the grand challenge as well as ultimate goal of designing oriented 2D nanomaterials locally and in 3D macrostructures is to leverage their exceptional properties for multifunctional devices. We have seen how 3D printing with local orientational control could open up the design capabilities by provide at least 6 degrees of freedom. How to make best use of such a large design space for target properties? How to open up all the possibilities to find among the best microstructure, composition, local orientation and so forth for realizing the highest performance? These are challenging questions to address which could be tackled with the establishment of open access databases, machine learning and artificial intelligence as well as smart reverse engineering optimization methods.

6. Conclusions

The emerging development of 2D nanomaterials such as graphene, BNNSs, MXenes, TMDCs, *etc.* sheds light on promising future applications. Controlled local orientation of 2D nanomaterials plays an increasingly important role in realizing high performances for multiple applications. In this paper, we first reported several examples that demonstrate the advantages of orienting 2D nanomaterials in specific directions for enhancing the performance of sensing, thermoelectric and electrochemical devices. We then systematically reviewed the state-of-the-art processing methods to induce controlled alignment of 2D nanomaterials in a desired manner, namely with horizontal, vertical, heterogeneous and arbitrary orientation. Recent advances in 3D printing techniques were then discussed and highlighted the possibility of upscaling 2D nanomaterial assembly from nano- to macro-scales, while further opening other advantages such as multimaterial fabrication and programmable time-dependent evolution. Although 2D nanomaterials with delicately designed local orientations have demonstrated their potential for inducing higher material performances in multiple functional applications, there are multiple challenges to overcome to really create the next generation of devices. We suggested enthusiastic future prospects in this research field as well as pinpointed a few challenges to solve to realize them. From the rapid development of 2D nanomaterials and orientation assembly technology, we can see the great potential in the currently established functional applications and a future breakthrough in harnessing the complexity and multifunctionality.

Author contributions

Hongying He: writing – original draft and conceptualization. Hortense Le Ferrand: conceptualization, supervision, writing – review and editing. Lizhi Guan: writing – review and editing.

Conflicts of interest

There are no conflicts to declare.

Acknowledgements

This research was supported by the National Research Foundation, Singapore under its National Research Foundation Fellowship scheme (award NRFF12-2020-0002).

References

1 K. S. Novoselov, A. K. Geim, S. V. Morozov, D.-e. Jiang, Y. Zhang, S. V. Dubonos, I. V. Grigorieva and A. A. Firsov, *Science*, 2004, **306**, 666–669.
2 K. S. Novoselov, A. K. Geim, S. V. Morozov, D. Jiang, M. I. Katsnelson, I. Grigorieva, S. Dubonos and A. A. Firsov, *Nature*, 2005, **438**, 197–200.
3 P. Blake, E. Hill, A. Castro Neto, K. Novoselov, D. Jiang, R. Yang, T. Booth and A. Geim, *Appl. Phys. Lett.*, 2007, **91**, 063124.
4 D. Akinwande, C. J. Brennan, J. S. Bunch, P. Egberts, J. R. Felts, H. Gao, R. Huang, J.-S. Kim, T. Li and Y. Li, *Extreme Mech. Lett.*, 2017, **13**, 42–77.
5 S. Z. Butler, S. M. Hollen, L. Cao, Y. Cui, J. A. Gupta, H. R. Gutiérrez, T. F. Heinz, S. S. Hong, J. Huang and A. F. Ismach, *ACS Nano*, 2013, **7**, 2898–2926.
6 Q. H. Wang, K. Kalantar-Zadeh, A. Kis, J. N. Coleman and M. S. Strano, *Nat. Nanotechnol.*, 2012, **7**, 699–712.
7 P. Sun, K. Wang and H. Zhu, *Adv. Mater.*, 2016, **28**, 2287–2310.

8 R. Mas-Balleste, C. Gomez-Navarro, J. Gomez-Herrero and F. Zamora, *Nanoscale*, 2011, **3**, 20–30.
9 J. Tang and Y. Yamauchi, *Nat. Chem.*, 2016, **8**, 638–639.
10 Y. Peng, Y. S. Li, Y. J. Ban, H. Jin, W. M. Jiao, X. L. Liu and W. S. Yang, *Science*, 2014, **346**, 1356–1359.
11 Y. Peng, Y. S. Li, Y. J. Ban and W. S. Yang, *Angew. Chem., Int. Ed.*, 2017, **56**, 9757–9761.
12 K. S. Novoselov, A. K. Geim, S. V. Morozov, D. Jiang, M. I. Katsnelson, I. Grigorieva, S. Dubonos and a. Firsov, *Nature*, 2005, **438**, 197–200.
13 A. K. Geim, *Science*, 2009, **324**, 1530–1534.
14 A. K. Geim and K. S. Novoselov, in *Nanoscience and technology: a collection of reviews from nature journals*, World Scientific, 2010, pp. 11–19.
15 C. Tan, X. Cao, X.-J. Wu, Q. He, J. Yang, X. Zhang, J. Chen, W. Zhao, S. Han and G.-H. Nam, *Chem. Rev.*, 2017, **117**, 6225–6331.
16 X. Zhang, Z. C. Lai, C. L. Tan and H. Zhang, *Angew. Chem., Int. Ed.*, 2016, **55**, 8816–8838.
17 H. T. Wang, H. T. Yuan, S. S. Hong, Y. B. Li and Y. Cui, *Chem. Soc. Rev.*, 2015, **44**, 2664–2680.
18 V. Guerra, C. Wan and T. McNally, *Prog. Mater. Sci.*, 2019, **100**, 170–186.
19 K. L. Zhang, Y. L. Feng, F. Wang, Z. C. Yang and J. Wang, *J. Mater. Chem. C*, 2017, **5**, 11992–12022.
20 Y. Lin and J. W. Connell, *Nanoscale*, 2012, **4**, 6908–6939.
21 B. Anasori, M. R. Lukatskaya and Y. Gogotsi, *Nat. Rev. Mater.*, 2017, **2**, 16098.
22 K. Hantanasirisakul and Y. Gogotsi, *Adv. Mater.*, 2018, **30**, 1804779.
23 C. Zhang, Y. L. Ma, X. T. Zhang, S. Abdolhosseinzadeh, H. W. Sheng, W. Lan, A. Pakdel, J. Heier and F. Nuesch, *Energy Environ. Sci.*, 2020, **3**, 29–55.
24 M. Naguib, M. Kurtoglu, V. Presser, J. Lu, J. Niu, M. Heon, L. Hultman, Y. Gogotsi and M. W. Barsoum, *Adv. Mater.*, 2011, **23**, 4248–4253.
25 M. Naguib, V. N. Mochalin, M. W. Barsoum and Y. Gogotsi, *Adv. Mater.*, 2014, **26**, 992–1005.
26 N. San Ha and G. Lu, *Composites, Part B*, 2020, **181**, 107496.
27 H.-B. Yao, H.-Y. Fang, X.-H. Wang and S.-H. Yu, *Chem. Soc. Rev.*, 2011, **40**, 3764–3785.
28 Y. Zhao, Z. Xie, H. Gu, C. Zhu and Z. Gu, *Chem. Soc. Rev.*, 2012, **41**, 3297–3317.
29 R. P. Behera and H. Le Ferrand, *Matter*, 2021, **4**, 2831–2849.
30 K. Liu and L. Jiang, *Nano Today*, 2011, **6**, 155–175.
31 R. L. Antoniou Kourounioti, L. R. Band, J. A. Fozard, A. Hampstead, A. Lovrics, E. Moyroud, S. Vignolini, J. R. King, O. E. Jensen and B. J. Glover, *J. R. Soc., Interface*, 2013, **10**, 20120847.
32 H. Wang, Z. Lu, S. Xu, D. Kong, J. J. Cha, G. Zheng, P.-C. Hsu, K. Yan, D. Bradshaw and F. B. Prinz, *Proc. Natl. Acad. Sci. U. S. A.*, 2013, **110**, 19701–19706.
33 E. Reyssat and L. Mahadevan, *J. R. Soc., Interface*, 2009, **6**, 951–957.
34 J. Deng, J. Li, P. Chen, X. Fang, X. Sun, Y. Jiang, W. Weng, B. Wang and H. Peng, *J. Am. Chem. Soc.*, 2016, **138**, 225–230.
35 D. Dogu, K. Tirak, Z. Candan and O. Unsal, *BioResources*, 2010, **5**, 2640–2663.
36 C. Wang, X. Chen, B. Wang, M. Huang, B. Wang, Y. Jiang and R. S. Ruoff, *ACS Nano*, 2018, **12**, 5816–5825.
37 J. Huang, X. Wang and Z. L. Wang, *Nano Lett.*, 2006, **6**, 2325–2331.
38 S. Gong, H. Ni, L. Jiang and Q. Cheng, *Mater. Today*, 2017, **20**, 210–219.
39 E. M. Spiesz, D. T. Schmieden, A. M. Grande, K. Liang, J. Schwiedrzik, F. Natalio, J. Michler, S. J. Garcia, M. E. Aubin-Tam and A. S. Meyer, *Small*, 2019, **15**, 1805312.
40 J. Wang, Q. Cheng, L. Lin and L. Jiang, *ACS Nano*, 2014, **8**, 2739–2745.
41 L. Grunenfelder, N. Suksangpanya, C. Salinas, G. Milliron, N. Yaraghi, S. Herrera, K. Evans-Lutterodt, S. Nutt, P. Zavattieri and D. Kisailus, *Acta Biomater.*, 2014, **10**, 3997–4008.
42 H. Le Ferrand, F. Bouville, T. P. Niebel and A. R. Studart, *Nat. Mater.*, 2015, **14**, 1172–1179.
43 B. Luo, G. Liu and L. Wang, *Nanoscale*, 2016, **8**, 6904–6920.
44 Z. Zhang, C. S. Lee and W. Zhang, *Adv. Energy Mater.*, 2017, **7**, 1700678.
45 N. A. Yaraghi and D. Kisailus, *Annu. Rev. Phys. Chem.*, 2018, **69**, 23–57.
46 M. S. Cao, X. X. Wang, M. Zhang, J. C. Shu, W. Q. Cao, H. J. Yang, X. Y. Fang and J. Yuan, *Adv. Funct. Mater.*, 2019, **29**, 1807398.
47 B. Xu, S. Qi, M. Jin, X. Cai, L. Lai, Z. Sun, X. Han, Z. Lin, H. Shao and P. Peng, *Chin. Chem. Lett.*, 2019, **30**, 2053–2064.
48 Q. Huang, S. Ni, M. Jiao, X. Zhong, G. Zhou and H. M. Cheng, *Small*, 2021, 2007676.
49 G. Shao, D. A. Hanaor, X. Shen and A. Gurlo, *Adv. Mater.*, 2020, **32**, 1907176.
50 C. Lei, Z. Xie, K. Wu and Q. Fu, *Adv. Mater.*, 2021, 2103495.
51 Z. Zhang, J. Du, J. Li, X. Huang, T. Kang, C. Zhang, S. Wang, O. O. Ajao, W.-J. Wang and P. Liu, *Prog. Polym. Sci.*, 2021, 101360.
52 D. Voiry, A. Mohite and M. Chhowalla, *Chem. Soc. Rev.*, 2015, **44**, 2702–2712.
53 R. M. Ronchi, J. T. Arantes and S. F. Santos, *Ceram. Int.*, 2019, **45**, 18167–18188.
54 B. G. Compton and J. A. Lewis, *Adv. Mater.*, 2014, **26**, 5930–5935.
55 S.-Y. Cho, S. J. Kim, Y. Lee, J.-S. Kim, W.-B. Jung, H.-W. Yoo, J. Kim and H.-T. Jung, *ACS Nano*, 2015, **9**, 9314–9321.
56 J. R. Szczech, J. M. Higgins and S. Jin, *J. Mater. Chem.*, 2011, **21**, 4037–4055.
57 J. Zhong, W. Sun, Q. Wei, X. Qian, H.-M. Cheng and W. Ren, *Nat. Commun.*, 2018, **9**, 1–11.
58 H. Li, J. Hou, T. D. Bennett, J. Liu and Y. Zhang, *J. Mater. Chem. A*, 2019, **7**, 5811–5818.
59 J. Y. Kim, J. Lim, H. M. Jin, B. H. Kim, S. J. Jeong, D. S. Choi, D. J. Li and S. O. Kim, *Adv. Mater.*, 2016, **28**, 1591–1596.
60 H. Le Ferrand, S. Bolisetty, A. F. Demirörs, R. Libanori, A. R. Studart and R. Mezzenga, *Nat. Commun.*, 2016, **7**, 1–9.

61 J. Zhu, E. Ha, G. Zhao, Y. Zhou, D. Huang, G. Yue, L. Hu, N. Sun, Y. Wang and L. Y. S. Lee, *Coord. Chem. Rev.*, 2017, **352**, 306–327.
62 H. He, X. Lu, E. Hanc, C. Chen, H. Zhang and L. Lu, *J. Mater. Chem. C*, 2020, **8**, 1494–1516.
63 H. He, X. Lu, M. Li, Y. Wang, Z. Li, Z. Lu and L. Lu, *J. Mater. Chem. C*, 2020, **8**, 2411–2418.
64 H. He, W. Lu, J. A. S. Oh, Z. Li, X. Lu, K. Zeng and L. Lu, *ACS Appl. Mater. Interfaces*, 2020, **12**, 30548–30556.
65 X. Liu, T. Ma, N. Pinna and J. Zhang, *Adv. Funct. Mater.*, 2017, **27**, 1702168.
66 G. H. Jeong, S. P. Sasikala, T. Yun, G. Y. Lee, W. J. Lee and S. O. Kim, *Adv. Mater.*, 2020, **32**, 1907006.
67 L. Zhang, K. Khan, J. Zou, H. Zhang and Y. Li, *Adv. Mater. Interfaces*, 2019, **6**, 1901329.
68 D. J. Buckley, N. C. Black, E. G. Castanon, C. Melios, M. Hardman and O. Kazakova, *2D Mater.*, 2020, **7**, 032002.
69 M. Long, P. Wang, H. Fang and W. Hu, *Adv. Funct. Mater.*, 2019, **29**, 1803807.
70 N. Huo and G. Konstantatos, *Adv. Mater.*, 2018, **30**, 1801164.
71 J. J. Pyeon, I.-H. Baek, Y. G. Song, G. S. Kim, A.-J. Cho, G.-Y. Lee, J. H. Han, T.-M. Chung, C. S. Hwang and C.-Y. Kang, *J. Mater. Chem. C*, 2020, **8**, 11874–11881.
72 M. A. Islam, H. Li, S. Moon, S. S. Han, H.-S. Chung, J. Ma, C. Yoo, T.-J. Ko, K. H. Oh and Y. Jung, *ACS Appl. Mater. Interfaces*, 2020, **12**, 53174–53183.
73 Z. Li, Y. Liu, D. Guo, J. Guo and Y. Su, *Sens. Actuators, B*, 2018, **271**, 306–310.
74 E. Lee, A. VahidMohammadi, Y. S. Yoon, M. Beidaghi and D.-J. Kim, *ACS Sens.*, 2019, **4**, 1603–1611.
75 S. J. Kim, H.-J. Koh, C. E. Ren, O. Kwon, K. Maleski, S.-Y. Cho, B. Anasori, C.-K. Kim, Y.-K. Choi and J. Kim, *ACS Nano*, 2018, **12**, 986–993.
76 D. J. Late, T. Doneux and M. Bougouma, *Appl. Phys. Lett.*, 2014, **105**, 233103.
77 H. Tang, Y. Li, R. Sokolovskij, L. Sacco, H. Zheng, H. Ye, H. Yu, X. Fan, H. Tian and T.-L. Ren, *ACS Appl. Mater. Interfaces*, 2019, **11**, 40850–40859.
78 A. Shokri and N. Salami, *Sens. Actuators, B*, 2016, **236**, 378–385.
79 H. J. Yoon, J. H. Yang, Z. Zhou, S. S. Yang and M. M.-C. Cheng, *Sens. Actuators, B*, 2011, **157**, 310–313.
80 W. Yuan and G. Shi, *J. Mater. Chem. A*, 2013, **1**, 10078–10091.
81 L. Kou, T. Frauenheim and C. Chen, *J. Phys. Chem. Lett.*, 2014, **5**, 2675–2681.
82 S. Cui, H. Pu, S. A. Wells, Z. Wen, S. Mao, J. Chang, M. C. Hersam and J. Chen, *Nat. Commun.*, 2015, **6**, 1–9.
83 T. Pham, G. Li, E. Bekyarova, M. E. Itkis and A. Mulchandani, *ACS Nano*, 2019, **13**, 3196–3205.
84 J.-H. Kim, A. Mirzaei, H. W. Kim and S. S. Kim, *Sens. Actuators, B*, 2020, **313**, 128040.
85 K. Rathi and K. Pal, *ACS Appl. Mater. Interfaces*, 2020, **12**, 38365–38375.
86 S. Kanaparthi and S. G. Singh, *Mater. Sci. Energy Technol.*, 2020, **3**, 91–96.
87 Z. Jiang, J. Li, H. Aslan, Q. Li, Y. Li, M. Chen, Y. Huang, J. P. Froning, M. Otyepka and R. Zbořil, *J. Mater. Chem. A*, 2014, **2**, 6714–6717.
88 M. S. Dresselhaus, G. Chen, M. Y. Tang, R. Yang, H. Lee, D. Wang, Z. Ren, J. P. Fleurial and P. Gogna, *Adv. Mater.*, 2007, **19**, 1043–1053.
89 G. J. Snyder and E. S. Toberer, *Materials for sustainable energy: a collection of peer-reviewed research and review articles from Nature Publishing Group*, 2011, pp. 101–110.
90 G. J. Snyder and T. S. Ursell, *Phys. Rev. Lett.*, 2003, **91**, 148301.
91 Y. Zhou and L. D. Zhao, *Adv. Mater.*, 2017, **29**, 1702676.
92 T. G. Novak, K. Kim and S. Jeon, *Nanoscale*, 2019, **11**, 19684–19699.
93 H. Goldsmid, *Thermoelectric refrigeration*, Springer, 2013.
94 Y. M. Zuev, W. Chang and P. Kim, *Phys. Rev. Lett.*, 2009, **102**, 096807.
95 Y. Xu, Z. Li and W. Duan, *Small*, 2014, **10**, 2182–2199.
96 D. Dragoman and M. Dragoman, *Appl. Phys. Lett.*, 2007, **91**, 203116.
97 D. Fan, H. Liu, L. Cheng, P. Jiang, J. Shi and X. Tang, *Appl. Phys. Lett.*, 2014, **105**, 133113.
98 Y. Guo, C. Dun, J. Xu, P. Li, W. Huang, J. Mu, C. Hou, C. A. Hewitt, Q. Zhang and Y. Li, *ACS Appl. Mater. Interfaces*, 2018, **10**, 33316–33321.
99 M. Khazaei, M. Arai, T. Sasaki, M. Estili and Y. Sakka, *Phys. Chem. Chem. Phys.*, 2014, **16**, 7841–7849.
100 S. Sarikurt, D. Çakır, M. Keçeli and C. Sevik, *Nanoscale*, 2018, **10**, 8859–8868.
101 H.-C. Chang and C.-H. Chen, *CrystEngComm*, 2011, **13**, 5956–5962.
102 J. Oh, Y. Kim, S. Chung, H. Kim and J. G. Son, *Adv. Mater. Interfaces*, 2019, **6**, 1901333.
103 K. Wu, Y. Zhang, F. Gong, D. Liu, C. Lei and Q. Fu, *Chem. Eng. J.*, 2021, **421**, 127764.
104 T. Zhu, Y. Liu, C. Fu, J. P. Heremans, J. G. Snyder and X. Zhao, *Adv. Mater.*, 2017, **29**, 1605884.
105 L. Fu, T. Wang, J. Yu, W. Dai, H. Sun, Z. Liu, R. Sun, N. Jiang, A. Yu and C.-T. Lin, *2D Mater.*, 2017, **4**, 025047.
106 X. Peng, L. Peng, C. Wu and Y. Xie, *Chem. Soc. Rev.*, 2014, **43**, 3303–3323.
107 R. Rojaee and R. Shahbazian-Yassar, *ACS Nano*, 2020, **14**, 2628–2658.
108 M. Ghidiu, M. R. Lukatskaya, M.-Q. Zhao, Y. Gogotsi and M. W. Barsoum, *Nature*, 2014, **516**, 78–81.
109 M. A. Hope, A. C. Forse, K. J. Griffith, M. R. Lukatskaya, M. Ghidiu, Y. Gogotsi and C. P. Grey, *Phys. Chem. Chem. Phys.*, 2016, **18**, 5099–5102.
110 V. Augustyn and Y. Gogotsi, *Joule*, 2017, **1**, 443–452.
111 M. R. Lukatskaya, S. Kota, Z. Lin, M.-Q. Zhao, N. Shpigel, M. D. Levi, J. Halim, P.-L. Taberna, M. W. Barsoum, P. Simon and Y. Gogotsi, *Nat. Energy*, 2017, **2**, 17105.
112 M. M. Forouzan, M. Wray, L. Robertson and D. R. Wheeler, *J. Electrochem. Soc.*, 2017, **164**, A3117–A3130.
113 X. Wang, T. Wang, J. Borovilas, X. He, S. Du and Y. Yang, *Nano Res.*, 2019, **12**, 2002–2017.
114 Y. Liu, Y. Zhu and Y. Cui, *Nat. Energy*, 2019, **4**, 540–550.

115 Z. Ju, X. Zhang, J. Wu and G. Yu, *Nano Res.*, 2021, **14**, 3562–3575.
116 Y. Xia, T. S. Mathis, M.-Q. Zhao, B. Anasori, A. Dang, Z. Zhou, H. Cho, Y. Gogotsi and S. Yang, *Nature*, 2018, **557**, 409–412.
117 J. R. Miller, R. Outlaw and B. Holloway, *Science*, 2010, **329**, 1637–1639.
118 Y. Yoon, K. Lee, S. Kwon, S. Seo, H. Yoo, S. Kim, Y. Shin, Y. Park, D. Kim and J.-Y. Choi, *ACS Nano*, 2014, **8**, 4580–4590.
119 J. Chen, Z. Bo and G. Lu, *Vertically-Oriented Graphene*, Springer International Publishing, Switzerland, 2015, vol. 10, pp. 978–973, DOI: 10.1007/978-3-319-15302-5.
120 J. Billaud, F. Bouville, T. Magrini, C. Villevieille and A. R. Studart, *Nat. Energy*, 2016, **1**, 16097.
121 H. Chen, A. Pei, J. Wan, D. Lin, R. Vilá, H. Wang, D. Mackanic, H.-G. Steinrück, W. Huang, Y. Li, A. Yang, J. Xie, Y. Wu, H. Wang and Y. Cui, *Joule*, 2020, **4**, 938–952.
122 X. Zhang, Z. Ju, L. M. Housel, L. Wang, Y. Zhu, G. Singh, N. Sadique, K. J. Takeuchi, E. S. Takeuchi, A. C. Marschilok and G. Yu, *Nano Lett.*, 2019, **19**, 8255–8261.
123 H. Chen, A. Pei, J. Wan, D. Lin, R. Vilá, H. Wang, D. Mackanic, H.-G. Steinrück, W. Huang and Y. Li, *Joule*, 2020, **4**, 938–952.
124 Z. Zhao, M. Sun, W. Chen, Y. Liu, L. Zhang, N. Dongfang, Y. Ruan, J. Zhang, P. Wang, L. Dong, Y. Xia and H. Lu, *Adv. Funct. Mater.*, 2019, **29**, 1809196.
125 R. Amin, B. Delattre, A. P. Tomsia and Y.-M. Chiang, *ACS Appl. Energy Mater.*, 2018, **1**, 4976–4981.
126 Z. Ju, Y. Zhu, X. Zhang, D. M. Lutz, Z. Fang, K. J. Takeuchi, E. S. Takeuchi, A. C. Marschilok and G. Yu, *Chem. Mater.*, 2020, **32**, 1684–1692.
127 L. Zhang, M. Zeng, Z. Liu, Q. Ma, Y. Lu, J. Ma and X. Yan, *ACS Appl. Energy Mater.*, 2021, **4**, 5590–5598.
128 W. Yang, J. J. Byun, J. Yang, F. P. Moissinac, Y. Peng, G. Tontini, R. A. W. Dryfe and S. Barg, *Energy Environ. Mater.*, 2020, **3**, 380–388.
129 K. W. Putz, O. C. Compton, M. J. Palmeri, S. T. Nguyen and L. C. Brinson, *Adv. Funct. Mater.*, 2010, **20**, 3322–3329.
130 K. W. Putz, O. C. Compton, C. Segar, Z. An, S. T. Nguyen and L. C. Brinson, *ACS Nano*, 2011, **5**, 6601–6609.
131 K. Wu, J. Fang, J. Ma, R. Huang, S. Chai, F. Chen and Q. Fu, *ACS Appl. Mater. Interfaces*, 2017, **9**, 30035–30045.
132 X. Lin, X. Shen, Q. Zheng, N. Yousefi, L. Ye, Y.-W. Mai and J.-K. Kim, *ACS Nano*, 2012, **6**, 10708–10719.
133 Z. Ling, C. E. Ren, M.-Q. Zhao, J. Yang, J. M. Giammarco, J. Qiu, M. W. Barsoum and Y. Gogotsi, *Proc. Natl. Acad. Sci. U. S. A.*, 2014, **111**, 16676–16681.
134 L. Ding, Y. Wei, L. Li, T. Zhang, H. Wang, J. Xue, L.-X. Ding, S. Wang, J. Caro and Y. Gogotsi, *Nat. Commun.*, 2018, **9**, 1–7.
135 A. Buekenhoudt, A. Kovalevsky, J. Luyten, F. Snijkers and L. Giorno, *Comprehensive Membrane Science and Engineering*, ed. G. L. Enrico, Elsevier, Oxford, 2010, pp. 217–252.
136 B. Dan, G. C. Irvin and M. Pasquali, *ACS Nano*, 2009, **3**, 835–843.
137 A. Akbari, P. Sheath, S. T. Martin, D. B. Shinde, M. Shaibani, P. C. Banerjee, R. Tkacz, D. Bhattacharyya and M. Majumder, *Nat. Commun.*, 2016, **7**, 1–12.
138 C. Simari, A. Enotiadis, C. L. Vecchio, V. Baglio, L. Coppola and I. Nicotera, *J. Membr. Sci.*, 2020, **599**, 117858.
139 Z. Liu, Z. Xu, X. Hu and C. Gao, *Macromolecules*, 2013, **46**, 6931–6941.
140 R. Jalili, S. Aminorroaya-Yamini, T. M. Benedetti, S. H. Aboutalebi, Y. Chao, G. G. Wallace and D. L. Officer, *Nanoscale*, 2016, **8**, 16862–16867.
141 Q. Yang, Z. Xu, B. Fang, T. Huang, S. Cai, H. Chen, Y. Liu, K. Gopalsamy, W. Gao and C. Gao, *J. Mater. Chem. A*, 2017, **5**, 22113–22119.
142 S. Seyedin, E. R. S. Yanza and J. M. Razal, *J. Mater. Chem. A*, 2017, **5**, 24076–24082.
143 J. Bohacek, A. Kharicha, A. Ludwig and M. Wu, *ISIJ Int.*, 2014, **54**, 266–274.
144 Q. Wei, S. Pei, X. Qian, H. Liu, Z. Liu, W. Zhang, T. Zhou, Z. Zhang, X. Zhang and H. M. Cheng, *Adv. Mater.*, 2020, **32**, 1907411.
145 H. Li, P. Tang, H. Shen, T. Hu, J. Chen, K. Chen, F. Qi, H. Yang, L. Wen and F. Li, *Carbon*, 2021, **183**, 840–849.
146 K. Wu, J. Wang, D. Liu, C. Lei, D. Liu, W. Lei and Q. Fu, *Adv. Mater.*, 2020, **32**, 1906939.
147 Z. Zhuang, Q. Peng and Y. Li, *Chem. Soc. Rev.*, 2011, **40**, 5492–5513.
148 S. Han, L. Hu, Z. Liang, S. Wageh, A. A. Al-Ghamdi, Y. Chen and X. Fang, *Adv. Funct. Mater.*, 2014, **24**, 5719–5727.
149 K.-J. Huang, J.-Z. Zhang, G.-W. Shi and Y.-M. Liu, *Electrochim. Acta*, 2014, **132**, 397–403.
150 Y. Deng, T. Shang, Z. Wu, Y. Tao, C. Luo, J. Liang, D. Han, R. Lyu, C. Qi and W. Lv, *Adv. Mater.*, 2019, **31**, 1902432.
151 Y. Xu, K. Sheng, C. Li and G. Shi, *ACS Nano*, 2010, **4**, 4324–4330.
152 W. Chen and L. Yan, *Nanoscale*, 2011, **3**, 3132–3137.
153 S.-H. Feng and G.-H. Li, in *Modern inorganic synthetic chemistry*, Elsevier, 2017, pp. 73–104.
154 W. Shi, S. Song and H. Zhang, *Chem. Soc. Rev.*, 2013, **42**, 5714–5743.
155 N. Xu, J. Liang, T. Qian, T. Yang and C. Yan, *RSC Adv.*, 2016, **6**, 98581–98587.
156 X. Yang, L. Qiu, C. Cheng, Y. Wu, Z. F. Ma and D. Li, *Angew. Chem., Int. Ed.*, 2011, **50**, 7325–7328.
157 D. Li, M. B. Müller, S. Gilje, R. B. Kaner and G. G. Wallace, *Nat. Nanotechnol.*, 2008, **3**, 101–105.
158 U. N. Maiti, J. Lim, K. E. Lee, W. J. Lee and S. O. Kim, *Adv. Mater.*, 2014, **26**, 615–619.
159 C. Chen, Y. Tan, X. Han, H. Luo, S. Zeng, S. Peng and H. Zhang, *J. Eur. Ceram. Soc.*, 2018, **38**, 5615–5619.
160 C. Yu, W. Gong, W. Tian, Q. Zhang, Y. Xu, Z. Lin, M. Hu, X. Fan and Y. Yao, *Compos. Sci. Technol.*, 2018, **160**, 199–207.
161 Y. Zhang, D. Li, X. Tan, B. Zhang, X. Ruan, H. Liu, C. Pan, L. Liao, T. Zhai and Y. Bando, *Carbon*, 2013, **54**, 143–148.
162 J. Kang, S. Hwang, J. H. Kim, M. H. Kim, J. Ryu, S. J. Seo, B. H. Hong, M. K. Kim and J.-B. Choi, *ACS Nano*, 2012, **6**, 5360–5365.

163 P. Liu, Z. Jin, G. Katsukis, L. W. Drahushuk, S. Shimizu, C.-J. Shih, E. D. Wetzel, J. K. Taggart-Scarff, B. Qing and K. J. Van Vliet, *Science*, 2016, **353**, 364–367.
164 X. Zhang, K. Wu, Y. Liu, B. Yu, Q. Zhang, F. Chen and Q. Fu, *Compos. Sci. Technol.*, 2019, **175**, 135–142.
165 A. Pockels, *Nature*, 1891, **43**, 437–439.
166 F. Rice and K. Herzfeld, *J. Am. Chem. Soc.*, 1934, **56**, 284–289.
167 M. Gleiche, L. F. Chi and H. Fuchs, *Nature*, 2000, **403**, 173–175.
168 F. Kim, L. J. Cote and J. Huang, *Adv. Mater.*, 2010, **22**, 1954–1958.
169 H.-L. Nie, X. Dou, Z. Tang, H. D. Jang and J. Huang, *J. Am. Chem. Soc.*, 2015, **137**, 10683–10688.
170 J. Huang, A. R. Tao, S. Connor, R. He and P. Yang, *Nano Lett.*, 2006, **6**, 524–529.
171 A. R. Tao, J. Huang and P. Yang, *Acc. Chem. Res.*, 2008, **41**, 1662–1673.
172 J. Shen, G. Liu, Y. Ji, Q. Liu, L. Cheng, K. Guan, M. Zhang, G. Liu, J. Xiong and J. Yang, *Adv. Funct. Mater.*, 2018, **28**, 1801511.
173 M. Zhang, K. Guan, Y. Ji, G. Liu, W. Jin and N. Xu, *Nat. Commun.*, 2019, **10**, 1–8.
174 M. Jabbari, R. Bulatova, A. Tok, C. Bahl, E. Mitsoulis and J. H. Hattel, *Mater. Sci. Eng., C*, 2016, **212**, 39–61.
175 H. Yuan, X. Liu, L. Ma, Z. Yang, H. Wang, J. Wang and S. Yang, *Composites, Part A*, 2017, **95**, 220–228.
176 W. G. Chong, J. Q. Huang, Z. L. Xu, X. Qin, X. Wang and J. K. Kim, *Adv. Funct. Mater.*, 2017, **27**, 1604815.
177 A. Azizi, M. R. Gadinski, Q. Li, M. A. AlSaud, J. Wang, Y. Wang, B. Wang, F. Liu, L. Q. Chen and N. Alem, *Adv. Mater.*, 2017, **29**, 1701864.
178 X. Lin, J. Jia, N. Yousefi, X. Shen and J.-K. Kim, *J. Mater. Chem. C*, 2013, **1**, 6869–6877.
179 Q. Zheng, W. H. Ip, X. Lin, N. Yousefi, K. K. Yeung, Z. Li and J.-K. Kim, *ACS Nano*, 2011, **5**, 6039–6051.
180 C. R. Safinya, E. B. Sirota, R. F. Bruinsma, C. Jeppesen, R. J. Plano and L. J. Wenzel, *Science*, 1993, **261**, 588–591.
181 R. Narayan, J. E. Kim, J. Y. Kim, K. E. Lee and S. O. Kim, *Adv. Mater.*, 2016, **28**, 3045–3068.
182 J. Mang, S. Kumar and B. Hammouda, *Europhys. Lett.*, 1994, **28**, 489.
183 S. Pandit, K. Gaska, V. R. Mokkapati, E. Celauro, A. Derouiche, S. Forsberg, M. Svensson, R. Kádár and I. Mijakovic, *Small*, 2020, **16**, 1904756.
184 C. Yang, Q. Li, M. Nie and Q. Wang, *Compos. Sci. Technol.*, 2021, **215**, 109034.
185 X. Shen, Q. Zheng and J.-K. Kim, *Prog. Mater. Sci.*, 2021, **115**, 100708.
186 S. Park, S. Ji, Y. Yoon, S. K. Kim, W. Song, S. Myung, J. Lim, H.-K. Jung, S. S. Lee and K.-S. An, *Carbon*, 2021, **182**, 691–699.
187 R. Ye, D. K. James and J. M. Tour, *Acc. Chem. Res.*, 2018, **51**, 1609–1620.
188 H. Palneedi, J. H. Park, D. Maurya, M. Peddigari, G. T. Hwang, V. Annapureddy, J. W. Kim, J. J. Choi, B. D. Hahn and S. Priya, *Adv. Mater.*, 2018, **30**, 1705148.
189 H. Zeng, X. W. Du, S. C. Singh, S. A. Kulinich, S. Yang, J. He and W. Cai, *Adv. Funct. Mater.*, 2012, **22**, 1333–1353.
190 L. Li, J. Zhang, Y. Wang, F. U. Zaman, Y. Zhang, L. Hou and C. Yuan, *InfoMat*, 2021, **3**(12), 1393–1421.
191 F. Ye, D. Chang, A. Ayub, K. Ibrahim, A. Shahin, R. Karimi, S. Wettig, J. Sanderson and K. P. Musselman, *Chem. Mater.*, 2021, **33**(12), 4510–4521.
192 S. Z. Noby, K. K. Wong, A. Ramadoss, S. Siroky, M. Hagner, K. Boldt and L. Schmidt-Mende, *RSC Adv.*, 2020, **10**, 24119–24126.
193 Z.-Y. Ma, Z.-L. Yu, Z.-L. Xu, L.-F. Bu, H.-R. Liu, Y.-B. Zhu, B. Qin, T. Ma, H.-J. Zhan and L. Xu, *Matter*, 2020, **2**, 1270–1282.
194 K. Byrappa and T. Adschiri, *Prog. Cryst. Growth Charact. Mater.*, 2007, **53**, 117–166.
195 M. K. Devaraju and I. Honma, *Adv. Energy Mater.*, 2012, **2**, 284–297.
196 J. Min, J. Liu, M. Lei, W. Wang, Y. Lu, L. Yang, Q. Yang, G. Liu and N. Su, *ACS Appl. Mater. Interfaces*, 2016, **8**, 780–791.
197 M. P. Thomas, A. Ullah, R. H. Pham, H. Djieutedjeu, J. P. Selegue and B. S. Guiton, *Cryst. Growth Des.*, 2020, **20**, 5728–5735.
198 I. S. Neira, Y. V. Kolen'ko, O. I. Lebedev, G. Van Tendeloo, H. S. Gupta, F. Guitián and M. Yoshimura, *Cryst. Growth Des.*, 2009, **9**, 466–474.
199 G. Canu and V. Buscaglia, *CrystEngComm*, 2017, **19**, 3867–3891.
200 G. Ren, M. N. F. Hoque, X. Pan, J. Warzywoda and Z. Fan, *J. Mater. Chem. A*, 2015, **3**, 10787–10794.
201 J. Zhu, K. Sakaushi, G. Clavel, M. Shalom, M. Antonietti and T.-P. Fellinger, *J. Am. Chem. Soc.*, 2015, **137**, 5480–5485.
202 Y. Jiao, A. Mukhopadhyay, Y. Ma, L. Yang, A. M. Hafez and H. Zhu, *Adv. Energy Mater.*, 2018, **8**, 1702779.
203 C. Lee, X. Wei, J. W. Kysar and J. Hone, *Science*, 2008, **321**, 385–388.
204 P. Y. Chen, M. Liu, Z. Wang, R. H. Hurt and I. Y. Wong, *Adv. Mater.*, 2017, **29**, 1605096.
205 J. Luo, H. D. Jang, T. Sun, L. Xiao, Z. He, A. P. Katsoulidis, M. G. Kanatzidis, J. M. Gibson and J. Huang, *ACS Nano*, 2011, **5**, 8943–8949.
206 V. M. Pereira, A. C. Neto, H. Liang and L. Mahadevan, *Phys. Rev. Lett.*, 2010, **105**, 156603.
207 J. Zang, S. Ryu, N. Pugno, Q. Wang, Q. Tu, M. J. Buehler and X. Zhao, *Nat. Mater.*, 2013, **12**, 321–325.
208 Z. Wang, D. Tonderys, S. E. Leggett, E. K. Williams, M. T. Kiani, R. S. Steinberg, Y. Qiu, I. Y. Wong and R. H. Hurt, *Carbon*, 2016, **97**, 14–24.
209 X. Lei, D. Ye, J. Chen, S. Tang, P. Sun, L. Chen, A. Lu, Y. Du and L. Zhang, *Chem. Mater.*, 2019, **31**, 10032–10039.
210 H. Jiang, D.-Y. Khang, J. Song, Y. Sun, Y. Huang and J. A. Rogers, *Proc. Natl. Acad. Sci. U. S. A.*, 2007, **104**, 15607–15612.
211 Y. Wang, R. Yang, Z. Shi, L. Zhang, D. Shi, E. Wang and G. Zhang, *ACS Nano*, 2011, **5**, 3645–3650.
212 J. Chen, X. Huang, B. Sun, Y. Wang, Y. Zhu and P. Jiang, *ACS Appl. Mater. Interfaces*, 2017, **9**, 30909–30917.

213 E. Pomerantseva and Y. Gogotsi, *Nat. Energy*, 2017, **2**, 1–6.
214 S. Srivastava and N. A. Kotov, *Acc. Chem. Res.*, 2008, **41**, 1831–1841.
215 P. T. Hammond, *AIChE J.*, 2011, **57**, 2928–2940.
216 D. W. Lee, T.-K. Hong, D. Kang, J. Lee, M. Heo, J. Y. Kim, B.-S. Kim and H. S. Shin, *J. Mater. Chem.*, 2011, **21**, 3438–3442.
217 L. Schmidt-Mende, A. Fechtenkötter, K. Müllen, E. Moons, R. H. Friend and J. D. MacKenzie, *Science*, 2001, **293**, 1119–1122.
218 B. Yao, J. Chen, L. Huang, Q. Zhou and G. Shi, *Adv. Mater.*, 2016, **28**, 1623–1629.
219 P. Xiong, B. Sun, N. Sakai, R. Ma, T. Sasaki, S. Wang, J. Zhang and G. Wang, *Adv. Mater.*, 2020, **32**, 1902654.
220 J. E. Kim, T. H. Han, S. H. Lee, J. Y. Kim, C. W. Ahn, J. M. Yun and S. O. Kim, *Angew. Chem.*, 2011, **123**, 3099–3103.
221 F. Lin, G. Yang, C. Niu, Y. Wang, Z. Zhu, H. Luo, C. Dai, D. Mayerich, Y. Hu and J. Hu, *Adv. Funct. Mater.*, 2018, **28**, 1805255.
222 F. Lin, Z. Zhu, X. Zhou, W. Qiu, C. Niu, J. Hu, K. Dahal, Y. Wang, Z. Zhao and Z. Ren, *Adv. Mater.*, 2017, **29**, 1604453.
223 H. Le Ferrand, *J. Eur. Ceram. Soc.*, 2021, **41**, 24–37.
224 V. Shukla, *Mater. Adv.*, 2020, **1**, 3104–3121.
225 R. M. Erb, R. Libanori, N. Rothfuchs and A. R. Studart, *Science*, 2012, **335**, 199–204.
226 H. Le Ferrand, F. Bouville and A. R. Studart, *Soft Matter*, 2019, **15**, 3886–3896.
227 H. L. Ferrand, 2021, arXiv preprint arXiv:2103.01440.
228 F. L. Bargardi, H. Le Ferrand, R. Libanori and A. R. Studart, *Nat. Commun.*, 2016, **7**, 1–8.
229 G. Kim and Y. M. Shkel, *J. Mater. Res.*, 2004, **19**, 1164–1174.
230 G. Kim, *Compos. Sci. Technol.*, 2005, **65**, 1728–1735.
231 T. Inadomi, S. Ikeda, Y. Okumura, H. Kikuchi and N. Miyamoto, *Macromol. Rapid Commun.*, 2014, **35**, 1741–1746.
232 Q. L. Zhu, C. Du, Y. Dai, M. Daab, M. Matejdes, J. Breu, W. Hong, Q. Zheng and Z. L. Wu, *Nat. Commun.*, 2020, **11**, 1–11.
233 S. Wu, R. B. Ladani, J. Zhang, E. Bafekrpour, K. Ghorbani, A. P. Mouritz, A. J. Kinloch and C. H. Wang, *Carbon*, 2015, **94**, 607–618.
234 S. Kim, J.-S. Oh, M.-G. Kim, W. Jang, M. Wang, Y. Kim, H. W. Seo, Y. C. Kim, J.-H. Lee and Y. Lee, *ACS Appl. Mater. Interfaces*, 2014, **6**, 17647–17653.
235 P. Collini, S. Kota, A. D. Dillon, M. W. Barsoum and A. T. Fafarman, *J. Electrochem. Soc.*, 2017, **164**, D573.
236 M. Talib, R. Tabassum, Abid, S. S. Islam and P. Mishra, *ACS Omega*, 2019, **4**, 6180–6191.
237 I. Nelson and S. E. Naleway, *J. Mater. Res. Technol.*, 2019, **8**, 2372–2385.
238 S. Deville, *Scr. Mater.*, 2018, **147**, 119–124.
239 W. Tang, S. Tang, X. Guan, X. Zhang, Q. Xiang and J. Luo, *Adv. Funct. Mater.*, 2019, **29**, 1900648.
240 S. Deville, *Adv. Eng. Mater.*, 2008, **10**, 155–169.
241 H. Zhang, I. Hussain, M. Brust, M. F. Butler, S. P. Rannard and A. I. Cooper, *Nat. Mater.*, 2005, **4**, 787–793.
242 H. Bai, Y. Chen, B. Delattre, A. P. Tomsia and R. O. Ritchie, *Sci. Adv.*, 2015, **1**, e1500849.
243 Y. Shao, M. F. El-Kady, C. W. Lin, G. Zhu, K. L. Marsh, J. Y. Hwang, Q. Zhang, Y. Li, H. Wang and R. B. Kaner, *Adv. Mater.*, 2016, **28**, 6719–6726.
244 R. Bian, G. He, W. Zhi, S. Xiang, T. Wang and D. Cai, *J. Mater. Chem. C*, 2019, **7**, 474–478.
245 M. M. Porter, P. Niksiar and J. McKittrick, *J. Am. Ceram. Soc.*, 2016, **99**, 1917–1926.
246 Y. Zhang, L. Hu and J. Han, *J. Am. Ceram. Soc.*, 2009, **92**, 1874–1876.
247 Z. Cai, B. Liu, X. Zou and H.-M. Cheng, *Chem. Rev.*, 2018, **118**, 6091–6133.
248 Y. Jung, J. Shen, Y. Liu, J. M. Woods, Y. Sun and J. J. Cha, *Nano Lett.*, 2014, **14**, 6842–6849.
249 P. Kumar and B. Viswanath, *CrystEngComm*, 2017, **19**, 5068–5078.
250 Y. Fang, I. S. Merenkov, X. Li, J. Xu, S. Lin, M. L. Kosinova and X. Wang, *J. Mater. Chem. A*, 2020, **8**, 13059–13064.
251 S. S. Han, J. H. Kim, C. Noh, J. H. Kim, E. Ji, J. Kwon, S. M. Yu, T.-J. Ko, E. Okogbue and K. H. Oh, *ACS Appl. Mater. Interfaces*, 2019, **11**, 13598–13607.
252 B. Zheng, Y. Chen, F. Qi, X. Wang, W. Zhang, Y. Li and X. Li, *2D Mater.*, 2017, **4**, 025092.
253 N. Choudhary, H. S. Chung, J. H. Kim, C. Noh, M. A. Islam, K. H. Oh, K. Coffey, Y. Jung and Y. Jung, *Adv. Mater. Interfaces*, 2018, **5**, 1800382.
254 D. Dumcenco, D. Ovchinnikov, O. L. Sanchez, P. Gillet, D. T. Alexander, S. Lazar, A. Radenovic and A. Kis, *2D Mater.*, 2015, **2**, 044005.
255 Y. Wang, J. Li, X. Li, H. Jin, W. Ali, Z. Song and S. Ding, *J. Mater. Chem. A*, 2022, **10**, 699–706.
256 M. Das, R. S. Ambekar, S. K. Panda, S. Chakraborty and C. S. Tiwary, *J. Mater. Res.*, 2021, **36**, 4024–4050.
257 I. J. Gómez, N. Alegret, A. Dominguez-Alfaro and M. Vázquez Sulleiro, *Chemistry*, 2021, **3**, 1314–1343.
258 L. R. Meza, S. Das and J. R. Greer, *Science*, 2014, **345**, 1322–1326.
259 J. R. Raney, B. G. Compton, J. Mueller, T. J. Ober, K. Shea and J. A. Lewis, *Proc. Natl. Acad. Sci. U. S. A.*, 2018, **115**, 1198–1203.
260 C. Zhu, T. Y.-J. Han, E. B. Duoss, A. M. Golobic, J. D. Kuntz, C. M. Spadaccini and M. A. Worsley, *Nat. Commun.*, 2015, **6**, 1–8.
261 C. W. Hull, *US Pat.*, Appl., No. 638905, Filed, 1984.
262 T. D. Ngo, A. Kashani, G. Imbalzano, K. T. Nguyen and D. Hui, *Composites, Part B*, 2018, **143**, 172–196.
263 Z. Chen, Z. Li, J. Li, C. Liu, C. Lao, Y. Fu, C. Liu, Y. Li, P. Wang and Y. He, *J. Eur. Ceram. Soc.*, 2019, **39**, 661–687.
264 X. Wang, M. Jiang, Z. Zhou, J. Gou and D. Hui, *Composites, Part B*, 2017, **110**, 442–458.
265 T. Campbell, C. Williams, O. Ivanova and B. Garrett, *Technologies, Potential, and Implications of Additive Manufacturing*, Atlantic Council, Washington, DC, 2011, vol. 3.

266 H. Lipson and M. Kurman, *Fabricated: The new world of 3D printing*, John Wiley & Sons, 2013.
267 H. Le Ferrand, *MRS Bull.*, 2020, **45**, 986.
268 H. Le Ferrand, *Acc. Mater. Res.*, 2020, **1**, 123–125.
269 G. Liu, X. Zhang, X. Chen, Y. He, L. Cheng, M. Huo, J. Yin, F. Hao, S. Chen and P. Wang, *Mater. Sci. Eng., R*, 2021, 100596.
270 Y. Zhang, F. Zhang, Z. Yan, Q. Ma, X. Li, Y. Huang and J. A. Rogers, *Nat. Rev. Mater.*, 2017, **2**, 1–17.
271 H. Le Ferrand, S. Chabi and S. Agarwala, *Adv. Intell. Syst.*, 2020, **2**, 1900151.
272 S. Dul, L. Fambri and A. Pegoretti, *Composites, Part A*, 2016, **85**, 181–191.
273 J. C. Camargo, Á. R. Machado, E. C. Almeida and E. F. M. S. Silva, *Int. J. Adv. Manuf. Technol.*, 2019, **103**, 2423–2443.
274 T. Carey, S. Cacovich, G. Divitini, J. Ren, A. Mansouri, J. M. Kim, C. Wang, C. Ducati, R. Sordan and F. Torrisi, *Nat. Commun.*, 2017, **8**, 1–11.
275 V. H. Y. Chou, W. C. Liu, M. Wittwer, H. Le Ferrand and M. Seita, *Acta Mater.*, 2022, 117798.
276 B. Huang, Z. Zhou, L. Wei, Q. Song, W. Yu, Y. Zhou, R. Hu, W. Zhang and C. Lu, *Composites, Part B*, 2021, **225**, 109261.
277 J. O. Palaganas, N. B. Palaganas, L. J. I. Ramos and C. P. C. David, *ACS Appl. Mater. Interfaces*, 2019, **11**, 46034–46043.
278 A. Gurijala, R. B. Zando, J. L. Faust, J. R. Barber, L. Zhang and R. M. Erb, *Matter*, 2020, **2**, 1015–1024.
279 K. Markandan, I. P. Seetoh and C. Q. Lai, *J. Mater. Res.*, 2021, **36**, 4262–4274.
280 H. Le Ferrand and A. F. Arrieta, *Soft Matter*, 2022, **18**, 1054–1063.
281 J. J. Martin, B. E. Fiore and R. M. Erb, *Nat. Commun.*, 2015, **6**, 1–7.
282 Q. Zhang, F. Zhang, S. P. Medarametla, H. Li, C. Zhou and D. Lin, *Small*, 2016, **12**, 1702–1708.
283 J. A. Lewis, *Adv. Funct. Mater.*, 2006, **16**, 2193–2204.
284 V. G. Rocha, E. Saiz, I. S. Tirichenko and E. García-Tuñón, *J. Mater. Chem. A*, 2020, **8**, 15646–15657.
285 T. Billiet, M. Vandenhaute, J. Schelfhout, S. Van Vlierberghe and P. Dubruel, *Biomaterials*, 2012, **33**, 6020–6041.
286 S.-z. Guo, X. Yang, M.-C. Heuzey and D. Therriault, *Nanoscale*, 2015, **7**, 6451–6456.
287 L. Li, Q. Lin, M. Tang, A. J. Duncan and C. Ke, *Chem.–Eur. J.*, 2019, **25**, 10768–10781.
288 A. M'barki, L. Bocquet and A. Stevenson, *Sci. Rep.*, 2017, **7**, 1–10.
289 W. H. Herschel and R. Bulkley, *Kolloid-Z.*, 1926, **39**, 291–300.
290 A. Saasen and J. D. Ytrehus, *Energies*, 2020, **13**, 5271.
291 R. Yang, J. Zhou, C. Yang, L. Qiu and H. Cheng, *Adv. Mater. Technol.*, 2020, **5**, 1901066.
292 X. Wang and F. Gordaninejad, *J. Intell. Mater. Syst. Struct.*, 1999, **10**, 601–608.
293 T. Gao, Z. Yang, C. Chen, Y. Li, K. Fu, J. Dai, E. M. Hitz, H. Xie, B. Liu and J. Song, *ACS Nano*, 2017, **11**, 11513–11520.
294 Z. Liang, Y. Pei, C. Chen, B. Jiang, Y. Yao, H. Xie, M. Jiao, G. Chen, T. Li and B. Yang, *ACS Nano*, 2019, **13**, 12653–12661.
295 S. Jambhulkar, S. Liu, P. Vala, W. Xu, D. Ravichandran, Y. Zhu, K. Bi, Q. Nian, X. Chen and K. Song, *ACS Nano*, 2021, **15**, 12057–12068.
296 G. Xin, W. Zhu, Y. Deng, J. Cheng, L. T. Zhang, A. J. Chung, S. De and J. Lian, *Nat. Nanotechnol.*, 2019, **14**, 168–175.
297 M. Trebbin, D. Steinhauser, J. Perlich, A. Buffet, S. V. Roth, W. Zimmermann, J. Thiele and S. Förster, *Proc. Natl. Acad. Sci. U. S. A.*, 2013, **110**, 6706–6711.
298 A. Ambrosi and M. Pumera, *Chem. Soc. Rev.*, 2016, **45**, 2740–2755.
299 S. K. Georgantzinos, G. I. Giannopoulos and P. A. Bakalis, *J. Compos. Sci.*, 2021, **5**, 119.
300 D. Kokkinis, M. Schaffner and A. R. Studart, *Nat. Commun.*, 2015, **6**, 1–10.
301 M. A. Skylar-Scott, J. Mueller, C. W. Visser and J. A. Lewis, *Nature*, 2019, **575**, 330–335.
302 J. O. Hardin, T. J. Ober, A. D. Valentine and J. A. Lewis, *Adv. Mater.*, 2015, **27**, 3279–3284.
303 S. Tibbits, The emergence of "4D printing", in *TED conference*, February 2013.
304 M. Zeng and Y. Zhang, *J. Mater. Chem. A*, 2019, **7**, 23301–23336.
305 F. Momeni, X. Liu and J. Ni, *Mater. Des.*, 2017, **122**, 42–79.
306 X. Kuang, D. J. Roach, J. Wu, C. M. Hamel, Z. Ding, T. Wang, M. L. Dunn and H. J. Qi, *Adv. Funct. Mater.*, 2019, **29**, 1805290.
307 S. Tibbits, *Archt. Des.*, 2014, **84**, 116–121.
308 Y. Guo, Y. Liu, J. Liu, J. Zhao, H. Zhang and Z. Zhang, *Composites, Part A*, 2020, **135**, 105903.
309 C. Yuan, D. J. Roach, C. K. Dunn, Q. Mu, X. Kuang, C. M. Yakacki, T. Wang, K. Yu and H. J. Qi, *Soft Matter*, 2017, **13**, 5558–5568.
310 P. Zhu, W. Yang, R. Wang, S. Gao, B. Li and Q. Li, *ACS Appl. Mater. Interfaces*, 2018, **10**, 36435–36442.
311 Y. Kim, H. Yuk, R. Zhao, S. A. Chester and X. Zhao, *Nature*, 2018, **558**, 274–279.
312 A. Chortos, E. Hajiesmaili, J. Morales, D. R. Clarke and J. A. Lewis, *Adv. Funct. Mater.*, 2020, **30**, 1907375.
313 F. B. Coulter, B. S. Coulter, E. Papastavrou and A. Ianakiev, *3D Print. Addit. Manuf.*, 2018, **5**, 17–28.
314 A. S. Gladman, E. A. Matsumoto, R. G. Nuzzo, L. Mahadevan and J. A. Lewis, *Nat. Mater.*, 2016, **15**, 413–418.
315 S. Amini, M. Tadayon, J. J. Loke, A. Kumar, D. Kanagavel, H. Le Ferrand, M. Duchamp, M. Raida, R. M. Sobota and L. Chen, *Proc. Natl. Acad. Sci. U. S. A.*, 2019, **116**, 8685–8692.
316 M. A. McEvoy and N. Correll, *Science*, 2015, **347**, 1261689.
317 J. Wen, B. K. Salunke and B. S. Kim, *J. Chem. Technol. Biotechnol.*, 2017, **92**, 1428–1435.
318 H.-L. Guo, X.-F. Wang, Q.-Y. Qian, F.-B. Wang and X.-H. Xia, *ACS Nano*, 2009, **3**, 2653–2659.
319 A. F. Demirörs, P. P. Pillai, B. Kowalczyk and B. A. Grzybowski, *Nature*, 2013, **503**, 99–103.

320 F. Li, Z. Zheng, X. Wang, H. Li and Y. Yan, *Chem. Eng. J.*, 2022, 135920.
321 D. Kokkinis, F. Bouville and A. R. Studart, *Adv. Mater.*, 2018, **30**, 1705808.
322 L. Ren, Z. Song, H. Liu, Q. Han, C. Zhao, B. Derby, Q. Liu and L. Ren, *Mater. Des.*, 2018, **156**, 470–479.
323 R. M. Hensleigh, H. Cui, J. S. Oakdale, C. Y. Jianchao, P. G. Campbell, E. B. Duoss, C. M. Spadaccini, X. Zheng and M. A. Worsley, *Mater. Horiz.*, 2018, **5**, 1035–1041.